

## 35. Particle Detectors at Accelerators

Revised 2017. See the various sections for authors.

### 35.1. Introduction

This review summarizes the detector technologies employed at accelerator particle physics experiments. Several of these detectors are also used in a non-accelerator context and examples of such applications will be provided. The detector techniques which are specific to non-accelerator particle physics experiments are the subject of Chap. 36. More detailed discussions of detectors and their underlying physics can be found in books by Ferbel [1], Kleinknecht [2], Knoll [3], Green [4], Leroy & Rancoita [5], and Grupen [6].

In Table 35.1 are given typical resolutions and deadtimes of common charged particle detectors. The quoted numbers are usually based on typical devices, and should be regarded only as rough approximations for new designs. The spatial resolution refers to the intrinsic detector resolution, i.e. without multiple scattering. We note that analog detector readout can provide better spatial resolution than digital readout by measuring the deposited charge in neighboring channels. Quoted ranges attempt to be representative of both possibilities. The time resolution is defined by how accurately the time at which a particle crossed the detector can be determined. The deadtime is the minimum separation in time between two resolved hits on the same channel. Typical performance of calorimetry and particle identification are provided in the relevant sections below.

**Table 35.1:** Typical resolutions and deadtimes of common charged particle detectors. Revised November 2011.

Detector Type	Intrinsic Spatial Resolution (rms)	Time Resolution	Dead Time
Resistive plate chamber	$\lesssim 10$ mm	1 ns (50 ps <sup>a</sup> )	—
Streamer chamber	300 $\mu\text{m}^b$	2 $\mu\text{s}$	100 ms
Liquid argon drift [7]	$\sim 175\text{--}450$ $\mu\text{m}$	$\sim 200$ ns	$\sim 2$ $\mu\text{s}$
Scintillation tracker	$\sim 100$ $\mu\text{m}$	100 ps/ $n^c$	10 ns
Bubble chamber	10–150 $\mu\text{m}$	1 ms	50 ms <sup>d</sup>
Proportional chamber	50–100 $\mu\text{m}^e$	2 ns	20–200 ns
Drift chamber	50–100 $\mu\text{m}$	2 ns <sup>f</sup>	20–100 ns
Micro-pattern gas detectors	30–40 $\mu\text{m}$	< 10 ns	10–100 ns
Silicon strip	pitch/(3 to 7) <sup>g</sup>	few ns <sup>h</sup>	$\lesssim 50$ ns <sup>h</sup>
Silicon pixel	$\lesssim 10$ $\mu\text{m}$	few ns <sup>h</sup>	$\lesssim 50$ ns <sup>h</sup>
Emulsion	1 $\mu\text{m}$	—	—

## 2 35. Particle detectors at accelerators

<sup>a</sup> For multiple-gap RPCs.

<sup>b</sup> 300  $\mu\text{m}$  is for 1 mm pitch (wirespacing/ $\sqrt{12}$ ).

<sup>c</sup>  $n$  = index of refraction.

<sup>d</sup> Multiple pulsing time.

<sup>e</sup> Delay line cathode readout can give  $\pm 150 \mu\text{m}$  parallel to anode wire.

<sup>f</sup> For two chambers.

<sup>g</sup> The highest resolution (“7”) is obtained for small-pitch detectors ( $\lesssim 25 \mu\text{m}$ ) with pulse-height-weighted center finding.

<sup>h</sup> Limited by the readout electronics [8].

### 35.2. Photon detectors

Updated August 2011 by D. Chakraborty (Northern Illinois U) and T. Sumiyoshi (Tokyo Metro U).

Most detectors in high-energy, nuclear, and astrophysics rely on the detection of photons in or near the visible range,  $100 \text{ nm} \lesssim \lambda \lesssim 1000 \text{ nm}$ , or  $E \approx$  a few eV. This range covers scintillation and Cherenkov radiation as well as the light detected in many astronomical observations.

Generally, photodetection involves generating a detectable electrical signal proportional to the (usually very small) number of incident photons. The process involves three distinct steps:

1. generation of a primary photoelectron or electron-hole ( $e-h$ ) pair by an incident photon by the photoelectric or photoconductive effect,
2. amplification of the p.e. signal to detectable levels by one or more multiplicative bombardment steps and/or an avalanche process (usually), and,
3. collection of the secondary electrons to form the electrical signal.

The important characteristics of a photodetector include the following in statistical averages:

1. quantum efficiency (QE or  $\epsilon_Q$ ): the number of primary photoelectrons generated per incident photon ( $0 \leq \epsilon_Q \leq 1$ ; in silicon more than one  $e-h$  pair per incident photon can be generated for  $\lambda \lesssim 165 \text{ nm}$ ),
2. collection efficiency (CE or  $\epsilon_C$ ): the overall acceptance factor other than the generation of photoelectrons ( $0 \leq \epsilon_C \leq 1$ ),
3. gain ( $G$ ): the number of electrons collected for each photoelectron generated,
4. dark current or dark noise: the electrical signal when there is no photon,
5. energy resolution: electronic noise (ENC or  $N_e$ ) and statistical fluctuations in the amplification process compound the Poisson distribution of  $n_\gamma$  photons from a given source:

$$\frac{\sigma(E)}{\langle E \rangle} = \sqrt{\frac{f_N}{n_\gamma \epsilon_Q \epsilon_C} + \left( \frac{N_e}{G n_\gamma \epsilon_Q \epsilon_C} \right)^2}, \quad (35.1)$$

where  $f_N$ , or the excess noise factor (ENF), is the contribution to the energy distribution variance due to amplification statistics [9],

6. dynamic range: the maximum signal available from the detector (this is usually expressed in units of the response to noise-equivalent power, or NEP, which is the

- optical input power that produces a signal-to-noise ratio of 1),
7. time dependence of the response: this includes the transit time, which is the time between the arrival of the photon and the electrical pulse, and the transit time spread, which contributes to the pulse rise time and width, and
  8. rate capability: inversely proportional to the time needed, after the arrival of one photon, to get ready to receive the next.

**Table 35.2:** Representative characteristics of some photodetectors commonly used in particle physics. The time resolution of the devices listed here vary in the 10–2000 ps range.

Type	$\lambda$ (nm)	$\epsilon_Q \epsilon_C$	Gain	Risetime (ns)	Area (mm <sup>2</sup> )	1-p.e noise (Hz)	HV (V)	Price (USD)
PMT*	115–1700	0.15–0.25	$10^3$ – $10^7$	0.7–10	$10^2$ – $10^5$	$10$ – $10^4$	500–3000	100–5000
MCP*	100–650	0.01–0.10	$10^3$ – $10^7$	0.15–0.3	$10^2$ – $10^4$	0.1–200	500–3500	10–6000
HPD*	115–850	0.1–0.3	$10^3$ – $10^4$	7	$10^2$ – $10^5$	$10$ – $10^3$	$\sim 2 \times 10^4$	$\sim 600$
GPM*	115–500	0.15–0.3	$10^3$ – $10^6$	$O(0.1)$	$O(10)$	$10$ – $10^3$	300–2000	$O(10)$
APD	300–1700	$\sim 0.7$	$10$ – $10^8$	$O(1)$	$10$ – $10^3$	$1$ – $10^3$	400–1400	$O(100)$
PPD	320–900	0.15–0.3	$10^5$ – $10^6$	$\sim 1$	1–10	$O(10^6)$	30–60	$O(100)$
VLPC	500–600	$\sim 0.9$	$\sim 5 \times 10^4$	$\sim 10$	1	$O(10^4)$	$\sim 7$	$\sim 1$

\*These devices often come in multi-anode configurations. In such cases, area, noise, and price are to be considered on a “per readout-channel” basis.

The QE is a strong function of the photon wavelength ( $\lambda$ ), and is usually quoted at maximum, together with a range of  $\lambda$  where the QE is comparable to its maximum. Spatial uniformity and linearity with respect to the number of photons are highly desirable in a photodetector’s response.

Optimization of these factors involves many trade-offs and vary widely between applications. For example, while a large gain is desirable, attempts to increase the gain for a given device also increases the ENF and after-pulsing (“echos” of the main pulse). In solid-state devices, a higher QE often requires a compromise in the timing properties. In other types, coverage of large areas by focusing increases the transit time spread.

Other important considerations also are highly application-specific. These include the photon flux and wavelength range, the total area to be covered and the efficiency required, the volume available to accommodate the detectors, characteristics of the environment such as chemical composition, temperature, magnetic field, ambient background, as well as ambient radiation of different types and, mode of operation (continuous or triggered), bias (high-voltage) requirements, power consumption, calibration needs, aging, cost, and so on. Several technologies employing different phenomena for the three steps described above, and many variants within each, offer a wide range of solutions to choose from. The

## 4 35. Particle detectors at accelerators

salient features of the main technologies and the common variants are described below. Some key characteristics are summarized in Table 35.2.

**35.2.1. Vacuum photodetectors :** Vacuum photodetectors can be broadly subdivided into three types: photomultiplier tubes, microchannel plates, and hybrid photodetectors.

**35.2.1.1. Photomultiplier tubes:** A versatile class of photon detectors, vacuum photomultiplier tubes (PMT) has been employed by a vast majority of all particle physics experiments to date [9]. Both “transmission-” and “reflection-type” PMT’s are widely used. In the former, the photocathode material is deposited on the inside of a transparent window through which the photons enter, while in the latter, the photocathode material rests on a separate surface that the incident photons strike. The cathode material has a low work function, chosen for the wavelength band of interest. When a photon hits the cathode and liberates an electron (the photoelectric effect), the latter is accelerated and guided by electric fields to impinge on a secondary-emission electrode, or dynode, which then emits a few ( $\sim 5$ ) secondary electrons. The multiplication process is repeated typically 10 times in series to generate a sufficient number of electrons, which are collected at the anode for delivery to the external circuit. The total gain of a PMT depends on the applied high voltage  $V$  as  $G = AV^{kn}$ , where  $k \approx 0.7\text{--}0.8$  (depending on the dynode material),  $n$  is the number of dynodes in the chain, and  $A$  a constant (which also depends on  $n$ ). Typically,  $G$  is in the range of  $10^5\text{--}10^6$ . Pulse risetimes are usually in the few nanosecond range. With *e.g.* two-level discrimination the effective time resolution can be much better.

A large variety of PMT’s, including many just recently developed, covers a wide span of wavelength ranges from infrared (IR) to extreme ultraviolet (XUV) [10]. They are categorized by the window materials, photocathode materials, dynode structures, anode configurations, *etc.* Common window materials are borosilicate glass for IR to near-UV, fused quartz and sapphire ( $\text{Al}_2\text{O}_3$ ) for UV, and  $\text{MgF}_2$  or  $\text{LiF}$  for XUV. The choice of photocathode materials include a variety of mostly Cs- and/or Sb-based compounds such as CsI, CsTe, bi-alkali (SbRbCs, SbKCs), multi-alkali (SbNa<sub>2</sub>KCs), GaAs(Cs), GaAsP, *etc.* Sensitive wavelengths and peak quantum efficiencies for these materials are summarized in Table 35.3. Typical dynode structures used in PMT’s are circular cage, line focusing, box and grid, venetian blind, and fine mesh. In some cases, limited spatial resolution can be obtained by using a mosaic of multiple anodes. Fast PMT’s with very large windows—measuring up to 508 mm across—have been developed in recent years for detection of Cherenkov radiation in neutrino experiments such as Super-Kamiokande and KamLAND among many others. Specially prepared low-radioactivity glass is used to make these PMT’s, and they are also able to withstand the high pressure of the surrounding liquid.

PMT’s are vulnerable to magnetic fields—sometimes even the geomagnetic field causes large orientation-dependent gain changes. A high-permeability metal shield is often necessary. However, proximity-focused PMT’s, *e.g.* the fine-mesh types, can be used even in a high magnetic field ( $\geq 1$  T) if the electron drift direction is parallel to the field. CMS uses custom-made vacuum phototriodes (VPT) mounted on the back face of projective lead tungstate crystals to detect scintillation light in the endcap sections of its electromagnetic calorimeters, which are inside a 3.8 T superconducting solenoid. A VPT

employs a single dynode (thus,  $G \approx 10$ ) placed close to the photocathode, and a mesh anode plane between the two, to help it cope with the strong magnetic field, which is not too unfavorably oriented with respect to the photodetector axis in the endcaps (within  $25^\circ$ ), but where the radiation level is too high for Avalanche Photodiodes (APD's) like those used in the barrel section.

**35.2.1.2. Microchannel plates:** A typical Microchannel plate (MCP) photodetector consists of one or more  $\sim 2$  mm thick glass plates with densely packed  $O(10 \mu\text{m})$ -diameter cylindrical holes, or “channels”, sitting between the transmission-type photocathode and anode planes, separated by  $O(1 \text{ mm})$  gaps. Instead of discrete dynodes, the inner surface of each cylindrical tube serves as a continuous dynode for the entire cascade of multiplicative bombardments initiated by a photoelectron. Gain fluctuations can be minimized by operating in a saturation mode, whence each channel is only capable of a binary output, but the sum of all channel outputs remains proportional to the number of photons received so long as the photon flux is low enough to ensure that the probability of a single channel receiving more than one photon during a single time gate is negligible. MCP's are thin, offer good spatial resolution, have excellent time resolution ( $\sim 20$  ps), and can tolerate random magnetic fields up to 0.1 T and axial fields up to  $\sim 1$  T. However, they suffer from relatively long recovery time per channel and short lifetime. MCP's are widely employed as image-intensifiers, although not so much in HEP or astrophysics.

**35.2.1.3. Hybrid photon detectors:** Hybrid photon detectors (HPD) combine the sensitivity of a vacuum PMT with the excellent spatial and energy resolutions of a Si sensor [11]. A single photoelectron ejected from the photocathode is accelerated through a potential difference of  $\sim 20$  kV before it impinges on the silicon sensor/anode. The gain nearly equals the maximum number of  $e$ - $h$  pairs that could be created from the entire kinetic energy of the accelerated electron:  $G \approx eV/w$ , where  $e$  is the electronic charge,  $V$  is the applied potential difference, and  $w \approx 3.7$  eV is the mean energy required to create an  $e$ - $h$  pair in Si at room temperature. Since the gain is achieved in a single step, one might expect to have the excellent resolution of a simple Poisson statistic with large mean, but in fact it is even better, thanks to the Fano effect discussed in Sec. 35.7.

Low-noise electronics must be used to read out HPD's if one intends to take advantage of the low fluctuations in gain, *e.g.* when counting small numbers of photons. HPD's can have the same  $\epsilon_Q \epsilon_C$  and window geometries as PMT's and can be segmented down to  $\sim 50 \mu\text{m}$ . However, they require rather high biases and will not function in a magnetic field. The exception is proximity-focused devices ( $\Rightarrow$  no (de)magnification) in an axial field. With time resolutions of  $\sim 10$  ps and superior rate capability, proximity-focused HPD's can be an alternative to MCP's. Current applications of HPD's include the CMS hadronic calorimeter and the RICH detector in LHCb. Large-size HPD's with sophisticated focusing may be suitable for future water Cherenkov experiments.

Hybrid APD's (HAPD's) add an avalanche multiplication step following the electron bombardment to boost the gain by a factor of  $\sim 50$ . This affords a higher gain and/or lower electrical bias, but also degrades the signal definition.

**Table 35.3:** Properties of photocathode and window materials commonly used in vacuum photodetectors [10].

Photocathode material	$\lambda$ (nm)	Window material	Peak $\epsilon_Q$ ( $\lambda/\text{nm}$ )
CsI	115–200	MgF <sub>2</sub>	0.11 (140)
CsTe	115–320	MgF <sub>2</sub>	0.14 (240)
Bi-alkali	300–650	Borosilicate	0.27 (390)
	160-650	Synthetic Silica	0.27 (390)
“Ultra Bi-alkali”	300–650	Borosilicate	0.43 (350)
	160-650	Synthetic Silica	0.43 (350)
Multi-alkali	300–850	Borosilicate	0.20 (360)
	160-850	Synthetic Silica	0.20 (360)
GaAs(Cs)*	160–930	Synthetic Silica	0.23 (280)
GaAsP(Cs)	300-750	Borosilicate	0.50 (500)
InP/InGaAsP <sup>†</sup>	350-1700	Borosilicate	0.01 (1100)

\*Reflection type photocathode is used. <sup>†</sup>Requires cooling to  $\sim -80^\circ\text{C}$ .

**35.2.2. Gaseous photon detectors :** In gaseous photomultipliers (GPM) a photoelectron in a suitable gas mixture initiates an avalanche in a high-field region, producing a large number of secondary impact-ionization electrons. In principle the charge multiplication and collection processes are identical to those employed in gaseous tracking detectors such as multiwire proportional chambers, micromesh gaseous detectors (Micromegas), or gas electron multipliers (GEM). These are discussed in Sec. 35.6.4.

The devices can be divided into two types depending on the photocathode material. One type uses solid photocathode materials much in the same way as PMT’s. Since it is resistant to gas mixtures typically used in tracking chambers, CsI is a common choice. In the other type, photoionization occurs on suitable molecules vaporized and mixed in the drift volume. Most gases have photoionization work functions in excess of 10 eV, which would limit their sensitivity to wavelengths far too short. However, vapors of TMAE (tetrakis dimethyl-amine ethylene) or TEA (tri-ethyl-amine), which have smaller work functions (5.3 eV for TMAE and 7.5 eV for TEA), are suited for XUV photon detection [12]. Since devices like GEM’s offer sub-mm spatial resolution, GPM’s are often used as position-sensitive photon detectors. They can be made into flat panels to cover large areas ( $O(1 \text{ m}^2)$ ), can operate in high magnetic fields, and are relatively inexpensive. Many of the ring imaging Cherenkov (RICH) detectors to date have used GPM’s for the detection of Cherenkov light [13]. Special care must be taken to suppress the photon-feedback process in GPM’s. It is also important to maintain high purity of the gas as minute traces of O<sub>2</sub> can significantly degrade the detection efficiency.

**35.2.3. Solid-state photon detectors** : In a phase of rapid development, solid-state photodetectors are competing with vacuum- or gas-based devices for many existing applications and making way for a multitude of new ones. Compared to traditional vacuum- and gaseous photodetectors, solid-state devices are more compact, lightweight, rugged, tolerant to magnetic fields, and often cheaper. They also allow fine pixelization, are easy to integrate into large systems, and can operate at low electric potentials, while matching or exceeding most performance criteria. They are particularly well suited for detection of  $\gamma$ - and X-rays. Except for applications where coverage of very large areas or dynamic range is required, solid-state detectors are proving to be the better choice. Some hybrid devices attempt to combine the best features of different technologies while applications of nanotechnology are opening up exciting new possibilities.

Silicon photodiodes (PD) are widely used in high-energy physics as particle detectors and in a great number of applications (including solar cells!) as light detectors. The structure is discussed in some detail in Sec. 35.7. In its simplest form, the PD is a reverse-biased  $p$ - $n$  junction. Photons with energies above the indirect bandgap energy (wavelengths shorter than about 1050 nm, depending on the temperature) can create  $e$ - $h$  pairs (the photoconductive effect), which are collected on the  $p$  and  $n$  sides, respectively. Often, as in the PD's used for crystal scintillator readout in CLEO, L3, Belle, BaBar, and GLAST, intrinsic silicon is doped to create a  $p$ - $i$ - $n$  structure. The reverse bias increases the thickness of the depleted region; in the case of these particular detectors, to full depletion at a depth of about 100  $\mu\text{m}$ . Increasing the depletion depth decreases the capacitance (and hence electronic noise) and extends the red response. Quantum efficiency can exceed 90%, but falls toward the red because of the increasing absorption length of light in silicon. The absorption length reaches 100  $\mu\text{m}$  at 985 nm. However, since  $G = 1$ , amplification is necessary. Optimal low-noise amplifiers are slow, but, even so, noise limits the minimum detectable signal in room-temperature devices to several hundred photons.

Very large arrays containing  $O(10^7)$  of  $O(10 \mu\text{m}^2)$ -sized photodiodes pixelizing a plane are widely used to photograph all sorts of things from everyday subjects at visible wavelengths to crystal structures with X-rays and astronomical objects from infrared to UV. To limit the number of readout channels, these are made into charge-coupled devices (CCD), where pixel-to-pixel signal transfer takes place over thousands of synchronous cycles with sequential output through shift registers [14]. Thus, high spatial resolution is achieved at the expense of speed and timing precision. Custom-made CCD's have virtually replaced photographic plates and other imagers for astronomy and in spacecraft. Typical QE's exceed 90% over much of the visible spectrum, and "thick" CCD's have useful QE up to  $\lambda = 1 \mu\text{m}$ . Active Pixel Sensor (APS) arrays with a preamplifier on each pixel and CMOS processing afford higher speeds, but are challenged at longer wavelengths. Much R&D is underway to overcome the limitations of both CCD and CMOS imagers.

In APD's, an exponential cascade of impact ionizations initiated by the original photogenerated  $e$ - $h$  pair under a large reverse-bias voltage leads to an avalanche breakdown [15]. As a result, detectable electrical response can be obtained from low-intensity optical signals down to single photons. Excellent junction uniformity is critical,

and a guard ring is generally used as a protection against edge breakdown. Well-designed APD's, such as those used in CMS' crystal-based electromagnetic calorimeter, have achieved  $\epsilon_Q \epsilon_C \approx 0.7$  with sub-ns response time. The sensitive wavelength window and gain depend on the semiconductor used. The gain is typically 10–200 in linear and up to  $10^8$  in Geiger mode of operation. Stability and close monitoring of the operating temperature are important for linear-mode operation, and substantial cooling is often necessary. Position-sensitive APD's use time information at multiple anodes to calculate the hit position.

One of the most promising recent developments in the field is that of devices consisting of large arrays ( $O(10^3)$ ) of tiny APD's packed over a small area ( $O(1 \text{ mm}^2)$ ) and operated in a limited Geiger mode [16]. Among different names used for this class of photodetectors, “PPD” (for “Pixelized Photon Detector”) is most widely accepted (formerly “SiPM”). Although each cell only offers a binary output, linearity with respect to the number of photons is achieved by summing the cell outputs in the same way as with a MCP in saturation mode (see above). PPD's are being adopted as the preferred solution for various purposes including medical imaging, *e.g.* positron emission tomography (PET). These compact, rugged, and economical devices allow auto-calibration through decent separation of photoelectron peaks and offer gains of  $O(10^6)$  at a moderate bias voltage ( $\sim 50 \text{ V}$ ). However, the single-photoelectron noise of a PPD, being the logical “or” of  $O(10^3)$  Geiger APD's, is rather large:  $O(1 \text{ MHz/mm}^2)$  at room temperature. PPD's are particularly well-suited for applications where triggered pulses of several photons are expected over a small area, *e.g.* fiber-guided scintillation light. Intense R&D is expected to lower the noise level and improve radiation hardness, resulting in coverage of larger areas and wider applications. Attempts are being made to combine the fabrication of the sensors and the front-end electronics (ASIC) in the same process with the goal of making PPD's and other finely pixelized solid-state photodetectors extremely easy to use.

Of late, much R&D has been directed to *p-i-n* diode arrays based on thin polycrystalline diamond films formed by chemical vapor deposition (CVD) on a hot substrate ( $\sim 1000 \text{ K}$ ) from a hydrocarbon-containing gas mixture under low pressure ( $\sim 100 \text{ mbar}$ ). These devices have maximum sensitivity in the extreme- to moderate-UV region [17]. Many desirable characteristics, including high tolerance to radiation and temperature fluctuations, low dark noise, blindness to most of the solar radiation spectrum, and relatively low cost make them ideal for space-based UV/XUV astronomy, measurement of synchrotron radiation, and luminosity monitoring at (future) lepton collider(s).

Visible-light photon counters (VLPC) utilize the formation of an impurity band only 50 meV below the conduction band in As-doped Si to generate strong ( $G \approx 5 \times 10^4$ ) yet sharp response to single photons with  $\epsilon_Q \approx 0.9$  [18]. The smallness of the band gap considerably reduces the gain dispersion. Only a very small bias ( $\sim 7 \text{ V}$ ) is needed, but high sensitivity to infrared photons requires cooling below 10 K. The dark noise increases sharply and exponentially with both temperature and bias. The Run 2 DØ detector used 86000 VLPC's to read the optical signal from its scintillating-fiber tracker and scintillator-strip preshower detectors.



### 35.3. Organic scintillators

Revised August 2017 by Kurtis F. Johnson (FSU).

Organic scintillators are broadly classed into three types, crystalline, liquid, and plastic, all of which utilize the ionization produced by charged particles (see Sec. 34.2 of this *Review*) to generate optical photons, usually in the blue to green wavelength regions [19]. Plastic scintillators are by far the most widely used, liquid organic scintillator is finding increased use, and crystal organic scintillators are practically unused in high-energy physics. Plastic scintillator densities range from 1.03 to 1.20 g cm<sup>-3</sup>. Typical photon yields are about 1 photon per 100 eV of energy deposit [20]. A one-cm-thick scintillator traversed by a minimum-ionizing particle will therefore yield  $\approx 2 \times 10^4$  photons. The resulting photoelectron signal will depend on the collection and transport efficiency of the optical package and the quantum efficiency of the photodetector.

Organic scintillator does not respond linearly to the ionization density. Very dense ionization columns emit less light than expected on the basis of  $dE/dx$  for minimum-ionizing particles. A widely used semi-empirical model by Birks posits that recombination and quenching effects between the excited molecules reduce the light yield [21]. These effects are more pronounced the greater the density of the excited molecules. Birks' formula is

$$\frac{d\mathcal{L}}{dx} = \mathcal{L}_0 \frac{dE/dx}{1 + k_B dE/dx}, \quad (35.2)$$

where  $\mathcal{L}$  is the luminescence,  $\mathcal{L}_0$  is the luminescence at low specific ionization density, and  $k_B$  is Birks' constant, which must be determined for each scintillator by measurement. Decay times are in the ns range; rise times are much faster. The high light yield and fast response time allow the possibility of sub-ns timing resolution [22]. The fraction of light emitted during the decay "tail" can depend on the exciting particle. This allows pulse shape discrimination as a technique to carry out particle identification. Because of the hydrogen content (carbon to hydrogen ratio  $\approx 1$ ) plastic scintillator is sensitive to proton recoils from neutrons. Ease of fabrication into desired shapes and low cost has made plastic scintillator a common detector element. In the form of scintillating fiber it has found widespread use in tracking and calorimetry [23].

Demand for large volume detectors has lead to increased use of liquid organic scintillator, which has the same scintillation mechanism as plastic scintillator, due to its cost advantage. The containment vessel defines the detector shape; photodetectors or waveshifters may be immersed in the liquid.

#### 35.3.1. Scintillation mechanism :

A charged particle traversing matter leaves behind it a wake of excited molecules. Certain types of molecules, however, will release a small fraction ( $\approx 3\%$ ) of this energy as optical photons. This process, scintillation, is especially marked in those organic substances which contain aromatic rings, such as polystyrene (PS) and polyvinyltoluene (PVT). Liquids which scintillate include toluene, xylene and pseudocumene.

In fluorescence, the initial excitation takes place via the absorption of a photon, and de-excitation by emission of a longer wavelength photon. Fluors are used as "waveshifters" to shift scintillation light to a more convenient wavelength. Occurring

in complex molecules, the absorption and emission are spread out over a wide band of photon energies, and have some overlap, that is, there is some fraction of the emitted light which can be re-absorbed [24]. This “self-absorption” is undesirable for detector applications because it causes a shortened attenuation length. The wavelength difference between the major absorption and emission peaks is called the Stokes’ shift. It is usually the case that the greater the Stokes’ shift, the smaller the self absorption thus, a large Stokes’ shift is a desirable property for a fluor.

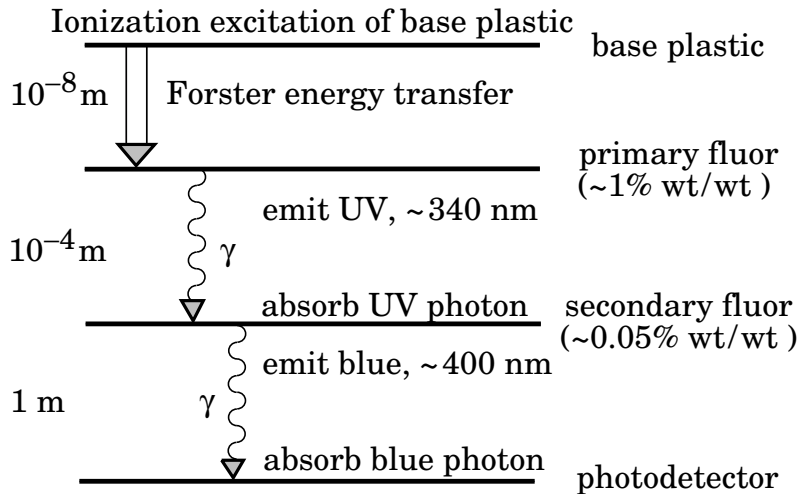


**Figure 35.1:** Cartoon of scintillation “ladder” depicting the operating mechanism of organic scintillator. Approximate fluor concentrations and energy transfer distances for the separate sub-processes are shown.

The plastic scintillators used in high-energy physics are binary or ternary solutions of selected fluors in a plastic base containing aromatic rings. (See appendix in Ref. 25 for a comprehensive list of components.) Virtually all plastic scintillators contain as a base either PVT or PS. PVT-based scintillator can be up to 50% brighter.

Ionization in the plastic base produces UV photons with short attenuation length (several mm). Longer attenuation lengths are obtained by dissolving a “primary” fluor in high concentration (1% by weight) into the base, which is selected to efficiently re-radiate absorbed energy at wavelengths where the base is more transparent (see Fig. 35.1).

The primary fluor has a second important function. The decay time of the scintillator base material can be quite long – in pure polystyrene it is 16 ns, for example. The addition of the primary fluor in high concentration can shorten the decay time by an order of magnitude and increase the total light yield. At the concentrations used (1% and greater), the average distance between a fluor molecule and an excited base unit is around 100 Å, much less than a wavelength of light. At these distances the predominant mode of energy transfer from base to fluor is not the radiation of a photon, but a resonant dipole-dipole interaction, first described by Foerster, which strongly couples the base and fluor [26]. The strong coupling sharply increases the speed and the light yield of the plastic scintillators.

Normally a fluor which fulfills other requirements is not adequate with respect

to emission wavelength or attenuation length, so it is necessary to add yet another waveshifter (the “secondary” fluor), at fractional percent levels, and occasionally a third (not shown in Fig. 35.1).

External wavelength shifters are widely used to aid light collection in complex geometries. Scintillation light is captured by a lightpipe comprising a wave-shifting fluor dissolved in a nonscintillating base. The wavelength shifter must be insensitive to ionizing radiation and Cherenkov light. A typical wavelength shifter uses an acrylic base because of its good optical qualities, a single fluor to shift the light emerging from the plastic scintillator to the blue-green, and contains ultra-violet absorbing additives to deaden response to Cherenkov light.

By drastically increasing fluor concentrations beyond those discussed above, scintillators of increased radiation resistance or with special properties such as neutron/gamma discrimination may be made [35].

### 35.3.2. *Caveats and cautions :*

Plastic scintillators are reliable, robust, and convenient. However, exposure to solvent vapors, high temperatures, mechanical flexing, irradiation, or rough handling will cause degradation. A The surface is particularly fragile region and can “craze” – develop microcracks which degrade transmission of light by total internal reflection. crazing is particularly likely where oils, solvents, or *fingerprints* have contacted the surface.

They have a long-lived luminescence which does not follow a simple exponential decay. Intensities at the  $10^{-4}$  level of the initial fluorescence can persist for hundreds of ns [19,27].

They can decrease their light yield with increasing partial pressure of oxygen. This can be a 10% effect in an artificial atmosphere [28].

Their light yield may be changed by a magnetic field. Increases of  $\approx 3\%$  at 0.45 T have been reported [29].

Irradiation of plastic scintillator creates color centers which absorb light more strongly in the UV and blue than at longer wavelengths. This poorly understood effect appears as a reduction both of light yield and attenuation length. Radiation damage depends not only on the integrated dose, but on the dose rate, atmosphere, and temperature, before, during and after irradiation, as well as the materials properties of the base such as glass transition temperature, polymer chain length, *etc.* Annealing also occurs, accelerated by the diffusion of atmospheric oxygen and elevated temperatures. The phenomena are complex, unpredictable, and not well understood [30]. Since color centers are most disruptive at shorter wavelengths, the most reliable method of mitigating radiation damage is to shift emissions at every step to the longest practical wavelengths, *e.g.*, utilize fluors with large Stokes’ shifts (aka the “Better red than dead” strategy).

**35.3.3. Scintillating and wavelength-shifting fibers :**

The clad optical fiber comprising scintillator and wavelength shifter (WLS) is particularly useful [31]. Since the initial demonstration of the scintillating fiber (SCIFI) calorimeter [32], SCIFI techniques have become mainstream [33]. SCIFI calorimeters are fast, dense, radiation hard, and can have leadglass-like resolution. SCIFI trackers can handle high rates and are radiation tolerant, but the low photon yield at the end of a long fiber (see below) requires use of sensitive photodetectors. WLS-only fiber readout of a calorimeter allows a very high level of hermeticity since the solid angle blocked by the fiber on its way to the photodetector is very small. The sensitive region of scintillating fibers can be controlled by splicing them onto clear (non-scintillating/non-WLS) fibers.

A typical configuration would be fibers with a core of polystyrene-based scintillator or WLS (index of refraction  $n = 1.59$ ), surrounded by a cladding of PMMA ( $n = 1.49$ ) a few microns thick, or, for added light capture, with another cladding of fluorinated PMMA with  $n = 1.42$ , for an overall diameter of 0.5 to 1 mm. The fraction of generated light which is transported down the optical fiber is denoted the capture fraction and is about 6% for the single-clad fiber and 10% for the double-clad fiber. A minimum-ionizing particle traversing a high-quality 1 mm diameter fiber perpendicular to its axis will produce fewer than 2000 photons, of which about 200 are captured. Attenuation may eliminate 95% of these photons in a large collider tracker.

A scintillating or WLS fiber is often characterized by its attenuation length, over which the signal is attenuated to  $1/e$  of its original value. Factors determining attenuation length include re-absorption of emitted photons by the polymer base or dissolved fluors, the level of crystallinity of the base polymer, variation of photodetector sensitivity to emitted wavelengths, and the quality of the internal surface [34]. Attenuation lengths of several meters are obtained by high quality fibers.

**35.4. Inorganic scintillators:**

Revised November 2017 by R.-Y. Zhu (California Institute of Technology) and C.L. Woody (BNL).

Inorganic crystals form a class of scintillating materials with much higher densities than organic plastic scintillators (typically  $\sim 4\text{--}8\text{ g/cm}^3$ ) with a variety of different properties for use as scintillation detectors. Due to their high density and high effective atomic number, they can be used in applications where high stopping power or a high conversion efficiency for electrons or photons is required. These include total absorption electromagnetic calorimeters (see Sec. 35.9.1), which consist of a totally active absorber (as opposed to a sampling calorimeter), as well as serving as gamma ray detectors over a wide range of energies. Many of these crystals also have very high light output, and can therefore provide excellent energy resolution down to very low energies ( $\sim$  few hundred keV).

Some crystals are intrinsic scintillators in which the luminescence is produced by a part of the crystal lattice itself. However, other crystals require the addition of a dopant, typically fluorescent ions such as thallium (Tl) or cerium (Ce) which is responsible for producing the scintillation light. However, in both cases, the scintillation mechanism is the same. Energy is deposited in the crystal by ionization, either directly by charged

particles, or by the conversion of photons into electrons or positrons which subsequently produce ionization. This energy is transferred to the luminescent centers which then radiate scintillation photons. The light yield  $L$  in terms of the number of scintillation photons produced per MeV of energy deposit in the crystal can be expressed as [36]

$$L = 10^6 S \cdot Q / (\beta \cdot E_g), \quad (35.3)$$

where  $\beta \cdot E_g$  is the energy required to create an e-h pair expressed as a multiple of the band gap energy  $E_g$  (eV),  $S$  is the efficiency of energy transfer to the luminescent center and  $Q$  is the quantum efficiency of the luminescent center. The values of  $\beta$ ,  $S$  and  $Q$  are crystal dependent and are the main factors in determining the intrinsic light yield of the scintillator. The decay time of the scintillator is mainly dominated by the decay time of the luminescent center.

Table 35.4 lists the basic properties of some commonly used inorganic crystals. NaI(Tl) is one of the most common and widely used scintillators, with an emission that is well matched to a bi-alkali photomultiplier tube, but it is highly hygroscopic and difficult to work with, and has a rather low density. CsI(Tl) and CsI(Na) have high light yield, low cost, and are mechanically robust (high plasticity and resistance to cracking). However, they need careful surface treatment and are slightly and highly hygroscopic respectively. Pure CsI has identical mechanical properties as CsI(Tl), but faster emission at shorter wavelength and a much lower light output. BaF<sub>2</sub> has a fast component with a sub-nanosecond decay time, and is the fastest known scintillator. However, it also has a slow component with a much longer decay time ( $\sim 630$  ns). Bismuth germanate (Bi<sub>4</sub>Ge<sub>3</sub>O<sub>12</sub> or BGO) has a high density, and consequently a short radiation length  $X_0$  and Molière radius  $R_M$ . Similar to CsI(Tl), BGO's emission is well-matched to the spectral sensitivity of photodiodes, and it is easy to handle and not hygroscopic. Lead tungstate (PbWO<sub>4</sub> or PWO) has a very high density, with a very short  $X_0$  and  $R_M$ , but its intrinsic light yield is rather low.

Cerium doped lutetium oxyorthosilicate (Lu<sub>2</sub>SiO<sub>5</sub>:Ce, or LSO:Ce) [37] and cerium doped lutetium-yttrium oxyorthosilicate (Lu<sub>2(1-x)</sub>Y<sub>2x</sub>SiO<sub>5</sub>, LYSO:Ce) [38] are dense crystal scintillators which have a high light yield and a fast decay time. Only the properties of LSO:Ce are listed in Table 35.4 since the properties of LYSO:Ce are similar to that of LSO:Ce except a slightly lower density than LSO:Ce depending on the yttrium fraction in LYSO:Ce. This material is also featured with excellent radiation hardness [39], so is expected to be used where extraordinary radiation hardness is required.

Also listed in Table 35.4 are other fluoride crystals such as PbF<sub>2</sub> as a Cherenkov material and CeF<sub>3</sub>, which have been shown to provide excellent energy resolution in calorimeter applications. Table 35.4 also includes cerium doped lanthanum tri-halides, such as LaBr<sub>3</sub> [40] and CeBr<sub>3</sub> [41], which are brighter and faster than LSO:Ce, but they are highly hygroscopic and have a lower density. The FWHM energy resolution measured for these materials coupled to a PMT with bi-alkali photocathode for 0.662 MeV  $\gamma$ -rays from a <sup>137</sup>Cs source is about 3%, and has recently been improved to 2% by co-doping with cerium and strontium [42], which is the best among all inorganic crystal scintillators. For this reason, LaBr<sub>3</sub> and CeBr<sub>3</sub> are expected to be used in applications where a good energy resolution for low energy photons are required, such as homeland security.

Beside the crystals listed in Table 35.4, a number of new crystals are being developed that may have potential applications in high energy or nuclear physics. Of particular interest is the family of yttrium and lutetium perovskites and garnet, which include YAP ( $\text{YAlO}_3:\text{Ce}$ ), LuAP ( $\text{LuAlO}_3:\text{Ce}$ ), YAG ( $\text{Y}_3\text{Al}_5\text{O}_{12}:\text{Ce}$ ) and LuAG ( $\text{Lu}_3\text{Al}_5\text{O}_{12}:\text{Ce}$ ) and their mixed compositions. These have been shown to be linear over a large energy range [43], and have the potential for providing good intrinsic energy resolution.

Aiming at the best jet-mass resolution inorganic scintillators are being investigated for HEP calorimeters with dual readout for both Cherenkov and scintillation light to be used at future linear colliders. These materials may be used for an electromagnetic calorimeter [44] or a homogeneous hadronic calorimetry (HHCAL) detector concept, including both electromagnetic and hadronic parts [45]. Because of the unprecedented volume (70 to 100  $\text{m}^3$ ) foreseen for the HHCAL detector concept the materials must be (1) dense (to minimize the leakage) and (2) cost-effective. It should also be UV transparent (for effective collection of the Cherenkov light) and allow for a clear discrimination between the Cherenkov and scintillation light. The preferred scintillation light is thus at a longer wavelength, and not necessarily bright or fast. Dense crystals, scintillating glasses and ceramics offer a very attractive implementation for this detector concept [46].

The fast scintillation light provides timing information about electromagnetic interactions and showers, which may be used to mitigate pile-up effects and/or for particle identification since the time development of electromagnetic and hadronic showers, as well as minimum ionizing particles, are different. The timing information is primarily determined by the scintillator rise time and decay time, and the number of photons produced. For fast timing, it is important to have a large number of photons emitted in the initial part of the scintillation pulse, e.g. in the first ns, since one is often measuring the arrival time of the particle in the crystal using the leading edge of the light pulse. A good example of this is  $\text{BaF}_2$ , which has  $\sim 10\%$  of its light in its fast component with a decay time of  $< 1$  ns. The light propagation can spread out the arrival time of the scintillation photons at the photodetector due to time dispersion [47]. The time response of the photodetector also plays a major role in achieving good time resolution with fast scintillating crystals.

Table 35.4 gives the light output of other crystals relative to  $\text{NaI}(\text{Tl})$  and their dependence to the temperature variations measured for 1.5  $X_0$  cube crystal samples with a Tyvek paper wrapping and a full end face coupled to a photodetector [48]. The quantum efficiencies of the photodetector is taken out to facilitate a direct comparison of crystal's light output. However, the useful signal produced by a scintillator is usually quoted in terms of the number of photoelectrons per MeV produced by a given photodetector. The relationship between the number of photons/MeV produced ( $L$ ) and photoelectrons/MeV detected ( $N_{\text{p.e.}}/\text{MeV}$ ) involves the factors for the light collection efficiency ( $LC$ ) and the quantum efficiency ( $QE$ ) of the photodetector:

$$N_{\text{p.e.}}/\text{MeV} = L \cdot LC \cdot QE. \quad (35.4)$$

$LC$  depends on the size and shape of the crystal, and includes effects such as the transmission of scintillation light within the crystal (i.e., the bulk attenuation length of the material), scattering from within the crystal, reflections and scattering from the

crystal surfaces, and re-bouncing back into the crystal by wrapping materials. These factors can vary considerably depending on the sample, but can be in the range of  $\sim 10\text{--}60\%$ . The internal light transmission depends on the intrinsic properties of the material, e.g. the density and type of the scattering centers and defects that can produce internal absorption within the crystal, and can be highly affected by factors such as radiation damage, as discussed below.

The quantum efficiency depends on the type of photodetector used to detect the scintillation light, which is typically  $\sim 15\text{--}30\%$  for photomultiplier tubes and  $\sim 70\%$  for silicon photodiodes for visible wavelengths. The quantum efficiency of the detector is usually highly wavelength dependent and should be matched to the particular crystal of interest to give the highest quantum yield at the wavelength corresponding to the peak of the scintillation emission. Fig. 35.2 shows the quantum efficiencies of two photodetectors, a Hamamatsu R2059 PMT with bi-alkali cathode and quartz window and a Hamamatsu S8664 avalanche photodiode (APD) as a function of wavelength. Also shown in the figure are emission spectra of three crystal scintillators, BGO, LSO:Ce/LYSO:Ce and CsI(Tl), and the numerical values of the emission weighted quantum efficiency. The area under each emission spectrum is proportional to crystal's light yield, as shown in Table 35.4, where the quantum efficiencies of the photodetector has been taken out. Results with different photodetectors can be significantly different. For example, the response of CsI(Tl) relative to NaI(Tl) with a standard photomultiplier tube with a bi-alkali photo-cathode, e.g. Hamamatsu R2059, would be 45 rather than 165 because of the photomultiplier's low quantum efficiency at longer wavelengths. For scintillators which emit in the UV, a detector with a quartz window should be used.

For very low energy applications (typically below 1 MeV), non-proportionality of the scintillation light yield may be important. It has been known for a long time that the conversion factor between the energy deposited in a crystal scintillator and the number of photons produced is not constant. It is also known that the energy resolution measured by all crystal scintillators for low energy  $\gamma$ -rays is significantly worse than the contribution from photo-electron statistics alone, indicating an intrinsic contribution from the scintillator itself. Precision measurement using low energy electron beam shows that this non-proportionality is crystal dependent [49]. Recent study on this issue also shows that this effect is also sample dependent even for the same crystal [50]. Further work is therefore needed to fully understand this subject.

One important issue related to the application of a crystal scintillator is its radiation hardness. Stability of its light output, or the ability to track and monitor the variation of its light output in a radiation environment, is required for high resolution and precision calibration [51]. All known crystal scintillators suffer from ionization dose induced radiation damage [52], where a common damage phenomenon is the appearance of radiation induced absorption caused by the formation of color centers originated from the impurities or point defects in the crystal. This radiation induced absorption reduces the light attenuation length in the crystal, and hence its light output. For crystals with high defect density, a severe reduction of light attenuation length may cause a distortion of the light response uniformity, leading to a degradation of the energy resolution. Additional radiation damage effects may include a reduced intrinsic scintillation light yield (damage

to the luminescent centers) and an increased phosphorescence (afterglow). For crystals to be used in a high precision calorimeter in a radiation environment, its scintillation mechanism must not be damaged and its light attenuation length in the expected radiation environment must be long enough so that its light response uniformity, and thus its energy resolution, does not change.

While radiation damage induced by ionization dose is well understood [53], investigation is on-going to understand radiation damage caused by hadrons, including both charged hadrons and neutrons [54]. Two additional fundamental processes may cause defects by hadrons: displacement damage and nuclear breakup. While charged hadrons can produce all three types of damage (and it's often difficult to separate them), neutrons can produce only the last two, and electrons and photons only produce ionization damage. Studies on hadron induced radiation damage to lead tungstate [56] show a proton-specific damage component caused by fragments from fission induced in lead and tungsten by particles in the hadronic shower. The fragments cause a severe, local damage to the crystalline lattice due to their extremely high energy loss over a short distance [56]. Investigation on neutron-specific damage in lead tungstate [57] up to  $4 \times 10^{19}$  n/cm<sup>2</sup> show no neutron-specific damage in PWO [58].

Most of the crystals listed in Table 35.4 have been used in high energy or nuclear physics experiments when the ultimate energy resolution for electrons and photons is desired. Examples are the Crystal Ball NaI(Tl) calorimeter at SPEAR, the L3 BGO calorimeter at LEP, the CLEO CsI(Tl) calorimeter at CESR, the KTeV CsI calorimeter at the Tevatron, the BaBar, BELLE and BES II CsI(Tl) calorimeters at PEP-II, KEK and BEPC III. Because of their high density and relative low cost, PWO calorimeters are used by CMS and ALICE at LHC, by CLAS and PrimEx at CEBAF and by PANDA at GSI, and PbF<sub>2</sub> calorimeters are used by the A4 experiment at MAINZ and by the g-2 experiment at Fermilab. A LYSO:Ce calorimeter is being built for the COMET experiment at J-PARC and a CsI calorimeter is being built for the Mu2e experiment at Fermilab.



**Table 35.4:** Properties of several inorganic crystals. Most of the notation is defined in Sec. 6 of this *Review*.

Parameter:	$\rho$	MP	$X_0^*$	$R_M^*$	$dE^*/dx$	$\lambda_I^*$	$\tau_{\text{decay}}$	$\lambda_{\text{max}}$	$n^{\natural}$	Relative output <sup>†</sup>	Hygro-scopic?	$d(\text{LY})/dT$
Units:	$\text{g}/\text{cm}^3$	$^{\circ}\text{C}$	cm	cm	$\text{MeV}/\text{cm}$	cm	ns	nm				$\%/^{\circ}\text{C}^{\ddagger}$
NaI(Tl)	3.67	651	2.59	4.13	4.8	42.9	245	410	1.85	100	yes	-0.2
BGO	7.13	1050	1.12	2.23	9.0	22.8	300	480	2.15	21	no	-0.9
BaF <sub>2</sub>	4.89	1280	2.03	3.10	6.5	30.7	650 <sup>s</sup> 0.9 <sup>f</sup>	300 <sup>s</sup> 220 <sup>f</sup>	1.50	36 <sup>s</sup> 4.1 <sup>f</sup>	no	-1.9 <sup>s</sup> 0.1 <sup>f</sup>
CsI(Tl)	4.51	621	1.86	3.57	5.6	39.3	1220	550	1.79	165	slight	0.4
CsI(Na)	4.51	621	1.86	3.57	5.6	39.3	690	420	1.84	88	yes	0.4
CsI(pure)	4.51	621	1.86	3.57	5.6	39.3	30 <sup>s</sup> 6 <sup>f</sup>	310	1.95	3.6 <sup>s</sup> 1.1 <sup>f</sup>	slight	-1.4
PbWO <sub>4</sub>	8.30	1123	0.89	2.00	10.1	20.7	30 <sup>s</sup> 10 <sup>f</sup>	425 <sup>s</sup> 420 <sup>f</sup>	2.20	0.3 <sup>s</sup> 0.077 <sup>f</sup>	no	-2.5
LSO(Ce)	7.40	2050	1.14	2.07	9.6	20.9	40	402	1.82	85	no	-0.2
PbF <sub>2</sub>	7.77	824	0.93	2.21	9.4	21.0	-	-	-	Cherenkov	no	-
CeF <sub>3</sub>	6.16	1460	1.70	2.41	8.42	23.2	30	340	1.62	7.3	no	0
LaBr <sub>3</sub> (Ce)	5.29	783	1.88	2.85	6.90	30.4	20	356	1.9	180	yes	0.2
CeBr <sub>3</sub>	5.23	722	1.96	2.97	6.65	31.5	17	371	1.9	165	yes	-0.1

\* Numerical values calculated using formulae in this review.

<sup>‡</sup> Refractive index at the wavelength of the emission maximum.

<sup>†</sup> Relative light output measured for samples of 1.5  $X_0$  cube with a Tyvek paper wrapping and a full end face coupled to a photodetector. The quantum efficiencies of the photodetector are taken out.

<sup>‡</sup> Variation of light yield with temperature evaluated at the room temperature.

$f$  = fast component,  $s$  = slow component

### 35.5. Cherenkov detectors

Revised August 2015 by B.N. Ratcliff (SLAC).

Although devices using Cherenkov radiation are often thought of as only particle identification (PID) detectors, in practice they are used over a much broader range of applications including; (1) fast particle counters; (2) hadronic PID; and (3) tracking detectors performing complete event reconstruction. Examples of applications from each category include; (1) the Quartic fast timing counter designed to measure small angle scatters at the LHC [59]; (2) the hadronic PID detectors at the B factory detectors—DIRC in BaBar [60] and the aerogel threshold Cherenkov in Belle [61]; and

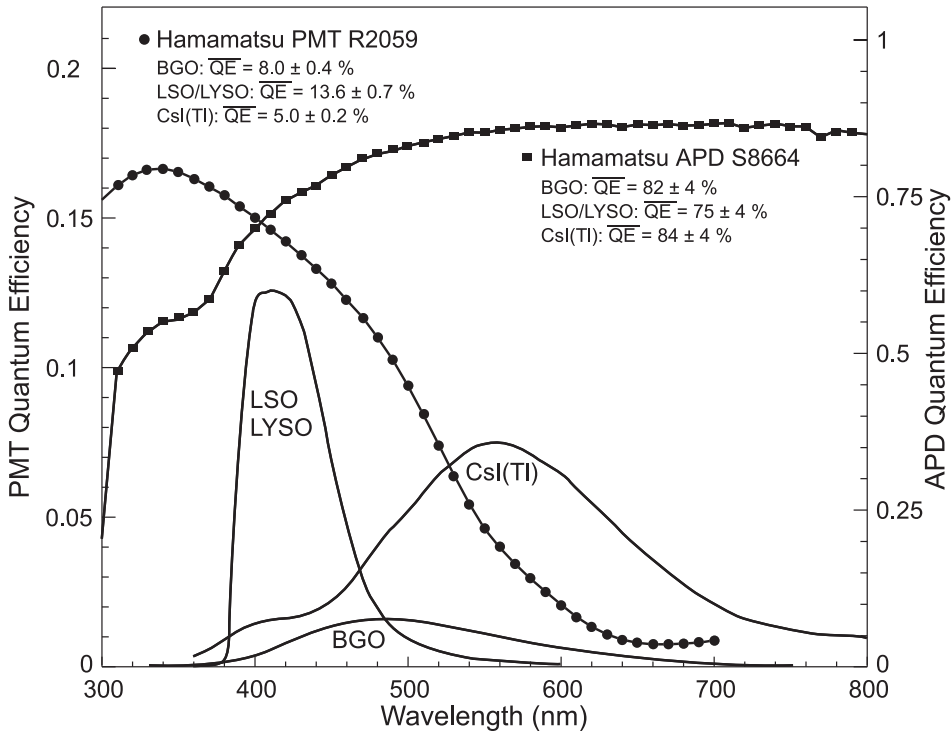


**Figure 35.2:** The quantum efficiencies of two photodetectors, a Hamamatsu R2059 PMT with bi-alkali cathode and a Hamamatsu S8664 avalanche photodiode (APD), are shown as a function of wavelength. Also shown in the figure are emission spectra of three crystal scintillators, BGO, LSO and Csl(Tl), and the numerical values of the emission weighted quantum efficiencies. The area under each emission spectrum is proportional to crystal's light yield.

(3) large water Cherenkov counters such as Super-Kamiokande [62]. Cherenkov counters contain two main elements; (1) a radiator through which the charged particle passes, and (2) a photodetector. As Cherenkov radiation is a weak source of photons, light collection and detection must be as efficient as possible. The refractive index  $n$  and the particle's path length through the radiator  $L$  appear in the Cherenkov relations allowing the tuning of these quantities for particular applications.

Cherenkov detectors utilize one or more of the properties of Cherenkov radiation discussed in the Passages of Particles through Matter section (Sec. 34 of this *Review*): the prompt emission of a light pulse; the existence of a velocity threshold for radiation; and the dependence of the Cherenkov cone half-angle  $\theta_c$  and the number of emitted photons on the velocity of the particle and the refractive index of the medium.

The number of photoelectrons ( $N_{p.e.}$ ) detected in a given device is

$$N_{p.e.} = L \frac{\alpha^2 z^2}{r_e m_e c^2} \int \epsilon(E) \sin^2 \theta_c(E) dE, \quad (35.5)$$

where  $\epsilon(E)$  is the efficiency for collecting the Cherenkov light and transducing it into photoelectrons, and  $\alpha^2/(r_e m_e c^2) = 370 \text{ cm}^{-1} \text{ eV}^{-1}$ .

The quantities  $\epsilon$  and  $\theta_c$  are functions of the photon energy  $E$ . As the typical energy dependent variation of the index of refraction is modest, a quantity called the *Cherenkov detector quality factor*  $N_0$  can be defined as

$$N_0 = \frac{\alpha^2 z^2}{r_e m_e c^2} \int \epsilon dE , \quad (35.6)$$

so that, taking  $z = 1$  (the usual case in high-energy physics),

$$N_{\text{p.e.}} \approx LN_0 \langle \sin^2 \theta_c \rangle . \quad (35.7)$$

This definition of the quality factor  $N_0$  is not universal, nor, indeed, very useful for those common situations where  $\epsilon$  factorizes as  $\epsilon = \epsilon_{\text{coll}} \epsilon_{\text{det}}$  with the geometrical photon collection efficiency ( $\epsilon_{\text{coll}}$ ) varying substantially for different tracks while the photon detector efficiency ( $\epsilon_{\text{det}}$ ) remains nearly track independent. In this case, it can be useful to explicitly remove ( $\epsilon_{\text{coll}}$ ) from the definition of  $N_0$ . A typical value of  $N_0$  for a photomultiplier (PMT) detection system working in the visible and near UV, and collecting most of the Cherenkov light, is about  $100 \text{ cm}^{-1}$ . Practical counters, utilizing a variety of different photodetectors, have values ranging between about 30 and  $180 \text{ cm}^{-1}$ . Radiators can be chosen from a variety of transparent materials (Sec. 34 of this *Review* and Table 6.1). In addition to refractive index, the choice requires consideration of factors such as material density, radiation length and radiation hardness, transmission bandwidth, absorption length, chromatic dispersion, optical workability (for solids), availability, and cost. When the momenta of particles to be identified is high, the refractive index must be set close to one, so that the photon yield per unit length is low and a long particle path in the radiator is required. Recently, the gap in refractive index that has traditionally existed between gases and liquid or solid materials has been partially closed with transparent *silica aerogels* with indices that range between about 1.007 and 1.13.

Cherenkov counters may be classified as either *imaging* or *threshold* types, depending on whether they do or do not make use of Cherenkov angle ( $\theta_c$ ) information. Imaging counters may be used to track particles as well as identify them. The recent development of very fast photodetectors such as micro-channel plate PMTs (MCP PMT) (see Sec. 35.2 of this *Review*) also potentially allows very fast Cherenkov based time of flight (TOF) detectors of either class [63]. The track timing resolution of imaging detectors can be extremely good as it scales approximately as  $\frac{1}{\sqrt{N_{\text{p.e.}}}}$ .

*Threshold* Cherenkov detectors [64], in their simplest form, make a yes/no decision based on whether the particle is above or below the Cherenkov threshold velocity  $\beta_t = 1/n$ . A straightforward enhancement of such detectors uses the number of observed photoelectrons (or a calibrated pulse height) to discriminate between species or to set probabilities for each particle species [65]. This strategy can increase the momentum range of particle separation by a modest amount (to a momentum some 20% above the threshold momentum of the heavier particle in a typical case).

Careful designs give  $\langle \epsilon_{\text{coll}} \rangle \gtrsim 90\%$ . For a photomultiplier with a typical bialkali cathode,  $\int \epsilon_{\text{det}} dE \approx 0.27 \text{ eV}$ , so that

$$N_{\text{p.e.}}/L \approx 90 \text{ cm}^{-1} \langle \sin^2 \theta_c \rangle \quad (i.e., N_0 = 90 \text{ cm}^{-1}) . \quad (35.8)$$

Suppose, for example, that  $n$  is chosen so that the threshold for species  $a$  is  $p_t$ ; that is, at this momentum species  $a$  has velocity  $\beta_a = 1/n$ . A second, lighter, species  $b$  with the same momentum has velocity  $\beta_b$ , so  $\cos \theta_c = \beta_a/\beta_b$ , and

$$N_{\text{p.e.}}/L \approx 90 \text{ cm}^{-1} \frac{m_a^2 - m_b^2}{p_t^2 + m_a^2}. \quad (35.9)$$

For  $K/\pi$  separation at  $p = p_t = 1(5) \text{ GeV}/c$ ,  $N_{\text{p.e.}}/L \approx 16(0.8) \text{ cm}^{-1}$  for  $\pi$ 's and (by design) 0 for  $K$ 's.

For limited path lengths  $N_{\text{p.e.}}$  will usually be small. The overall efficiency of the device is controlled by Poisson fluctuations, which can be especially critical for separation of species where one particle type is dominant. Moreover, the effective number of photoelectrons is often less than the average number calculated above due to additional equivalent noise from the photodetector (see the discussion of the excess noise factor in Sec. 35.2 of this *Review*). It is common to design for at least 10 photoelectrons for the high velocity particle in order to obtain a robust counter. As rejection of the particle that is below threshold depends on *not* seeing a signal, electronic and other background noise, especially overlapping tracks, can be important. Physics sources of light production for the below threshold particle, such as decay to an above threshold particle, scintillation light, or the production of delta rays in the radiator, often limit the separation attainable, and need to be carefully considered. Well designed, modern multi-channel counters, such as the ACC at Belle [61], can attain adequate particle separation performance over a substantial momentum range.

*Imaging* counters make the most powerful use of the information available by measuring the ring-correlated angles of emission of the individual Cherenkov photons. They typically provide positive ID information both for the “wanted” and the “unwanted” particles, thus reducing mis-identification substantially. Since low-energy photon detectors can measure only the position (and, perhaps, a precise detection time) of the individual Cherenkov photons (not the angles directly), the photons must be “imaged” onto a detector so that their angles can be derived [66]. Typically the optics map the Cherenkov cone onto (a portion of) a distorted “circle” at the photodetector. Though the imaging process is directly analogous to familiar imaging techniques used in telescopes and other optical instruments, there is a somewhat bewildering variety of methods used in a wide variety of counter types with different names. Some of the imaging methods used include (1) focusing by a lens or mirror; (2) proximity focusing (i.e., focusing by limiting the emission region of the radiation); and (3) focusing through an aperture (a pinhole). In addition, the prompt Cherenkov emission coupled with the speed of some modern photon detectors allows the use of (4) time imaging, a method which is little used in conventional imaging technology, and may allow some separation with particle TOF. Finally, (5) correlated tracking (and event reconstruction) can be performed in large water counters by combining the individual space position and time of each photon together with the constraint that Cherenkov photons are emitted from each track at the same polar angle (Sec. 36.3.1 of this *Review*).

In a simple model of an imaging PID counter, the fractional error on the particle velocity ( $\delta_\beta$ ) is given by

$$\delta_\beta = \frac{\sigma_\beta}{\beta} = \tan \theta_c \sigma(\theta_c) \quad , \quad (35.10)$$

where

$$\sigma(\theta_c) = \frac{\langle \sigma(\theta_i) \rangle}{\sqrt{N_{\text{p.e.}}}} \oplus C \quad , \quad (35.11)$$

and  $\langle \sigma(\theta_i) \rangle$  is the average single photoelectron resolution, as defined by the optics, detector resolution and the intrinsic chromaticity spread of the radiator index of refraction averaged over the photon detection bandwidth.  $C$  combines a number of other contributions to resolution including, (1) correlated terms such as tracking, alignment, and multiple scattering, (2) hit ambiguities, (3) background hits from random sources, and (4) hits coming from other tracks. The actual separation performance is also limited by physics effects such as decays in flight and particle interactions in the material of the detector. In many practical cases, the performance is limited by these effects.

For a  $\beta \approx 1$  particle of momentum ( $p$ ) well above threshold entering a radiator with index of refraction ( $n$ ), the number of  $\sigma$  separation ( $N_\sigma$ ) between particles of mass  $m_1$  and  $m_2$  is approximately

$$N_\sigma \approx \frac{|m_1^2 - m_2^2|}{2p^2 \sigma(\theta_c) \sqrt{n^2 - 1}} \quad . \quad (35.12)$$

In practical counters, the angular resolution term  $\sigma(\theta_c)$  varies between about 0.1 and 5 mrad depending on the size, radiator, and photodetector type of the particular counter. The range of momenta over which a particular counter can separate particle species extends from the point at which the number of photons emitted becomes sufficient for the counter to operate efficiently as a threshold device ( $\sim 20\%$  above the threshold for the lighter species) to the value in the imaging region given by the equation above. For example, for  $\sigma(\theta_c) = 2\text{mrad}$ , a fused silica radiator ( $n = 1.474$ ), or a fluorocarbon gas radiator ( $\text{C}_5\text{F}_{12}$ ,  $n = 1.0017$ ), would separate  $\pi/K$ 's from the threshold region starting around 0.15(3) GeV/ $c$  through the imaging region up to about 4.2(18) GeV/ $c$  at better than  $3\sigma$ .

Many different imaging counters have been built during the last several decades [63]. Among the earliest examples of this class of counters are the very limited acceptance Differential Cherenkov detectors, designed for particle selection in high momentum beam lines. These devices use optical focusing and/or geometrical masking to select particles having velocities in a specified region. With careful design, a velocity resolution of  $\sigma_\beta/\beta \approx 10^{-4}$ – $10^{-5}$  can be obtained [64].

Practical multi-track Ring-Imaging Cherenkov detectors (generically called RICH counters) are a more recent development. RICH counters are sometimes further classified by ‘generations’ that differ based on historical timing, performance, design, and photodetection techniques.

Prototypical examples of first generation RICH counters are those used in the DELPHI and SLD detectors at the LEP and SLC Z factory  $e^+e^-$  colliders [63]. They have both liquid ( $\text{C}_6\text{F}_{14}$ ,  $n = 1.276$ ) and gas ( $\text{C}_5\text{F}_{12}$ ,  $n = 1.0017$ ) radiators, the former

being proximity imaged with the latter using mirrors. The phototransducers are a TPC/wire-chamber combination. They are made sensitive to photons by doping the TPC gas (usually, ethane/methane) with  $\sim 0.05\%$  TMAE (tetrakis(dimethylamino)ethylene). Great attention to detail is required, (1) to avoid absorbing the UV photons to which TMAE is sensitive, (2) to avoid absorbing the single photoelectrons as they drift in the long TPC, and (3) to keep the chemically active TMAE vapor from interacting with materials in the system. In spite of their unforgiving operational characteristics, these counters attained good  $e/\pi/K/p$  separation over wide momentum ranges (from about 0.25 to 20 GeV/ $c$ ) during several years of operation at LEP and SLC. Related but smaller acceptance devices include the OMEGA RICH at the CERN SPS, and the RICH in the balloon-borne CAPRICE detector [63].

Later generation counters [63] generally operate at much higher rates, with more detection channels, than the first generation detectors just described. They also utilize faster, more forgiving photon detectors, covering different photon detection bandwidths. Radiator choices have broadened to include materials such as lithium fluoride, fused silica, and aerogel. Vacuum based photodetection systems (*e.g.*, single or multi anode PMTs, MCP PMTs, or hybrid photodiodes (HPD)) have become increasingly common (see Sec. 35.2 of this *Review*). They handle high rates, and can be used with a wide choice of radiators. Examples include (1) the SELEX RICH at Fermilab, which mirror focuses the Cherenkov photons from a neon radiator onto a camera array made of  $\sim 2000$  PMTs to separate hadrons over a wide momentum range (to well above 200 GeV/ $c$  for heavy hadrons); (2) the HERMES RICH at HERA, which mirror focuses photons from  $C_4F_{10}$  ( $n = 1.00137$ ) and aerogel ( $n = 1.0304$ ) radiators within the same volume onto a PMT camera array to separate hadrons in the momentum range from 2 to 15 GeV/ $c$ ; and (3) the LHCb detector now running at the LHC. It uses two separate counters readout by hybrid PMTs. One volume, like HERMES, contains two radiators (aerogel and  $C_4F_{10}$ ) while the second volume contains  $CF_4$ . Photons are mirror focused onto detector arrays of HPDs to cover a  $\pi/K$  separation momentum range between 1 and 150 GeV/ $c$ . This device will be upgraded to deal with the higher luminosities provided by LHC after 2018 by modifying the optics and removing the aerogel radiator of the upstream RICH and replacing the Hybrid PMTs with multi-anode PMTs (MaPMTs).

Other fast detection systems that use solid cesium iodide (CsI) photocathodes or triethylamine (TEA) doping in proportional chambers are useful with certain radiator types and geometries. Examples include (1) the CLEO-III RICH at CESR that uses a LiF radiator with TEA doped proportional chambers; (2) the ALICE detector at the LHC that uses proximity focused liquid ( $C_6F_{14}$  radiators and solid CSI photocathodes (similar photodetectors have been used for several years by the HADES and COMPASS detectors), and the hadron blind detector (HBD) in the PHENIX detector at RHIC that couples a low index  $CF_4$  radiator to a photodetector based on electron multiplier (GEM) chambers with reflective CSI photocathodes [63].

A DIRC (Detection [of] Internally Reflected Cherenkov [light]) is a distinctive, compact RICH subtype first used in the BaBar detector [60,63]. A DIRC “inverts” the usual RICH principle for use of light from the radiator by collecting and imaging the total internally reflected light rather than the transmitted light. It utilizes the optical material

of the radiator in two ways, simultaneously; first as a Cherenkov radiator, and second, as a light pipe. The magnitudes of the photon angles are preserved during transport by the flat, rectangular cross section radiators, allowing the photons to be efficiently transported to a detector outside the path of the particle where they may be imaged in up to three independent dimensions (the usual two in space and, due to the long photon paths lengths, one in time). Because the index of refraction in the radiator is large ( $\sim 1.48$  for fused silica), light collection efficiency is good, but the momentum range with good  $\pi/K$  separation is rather low. The BaBar DIRC range extends up to  $\sim 4$  GeV/ $c$ . It is plausible, but challenging, to extend it up to about 10 GeV/ $c$  with an improved design. New DIRC detectors are being developed that take advantage of the new, very fast, pixelated photodetectors becoming available, such as flat panel MaPMTs and MCP PMTs. They typically utilize either time imaging or mirror focused optics, or both, leading not only to a precision measurement of the Cherenkov angle, but in some cases, to a precise measurement of the particle TOF, and/or to correction of the chromatic dispersion in the radiator. Examples [63] include (1) the time of propagation (TOP) counter being fabricated for the BELLE-II upgrade at KEKB emphasizing precision timing for both Cherenkov imaging and TOF, which is scheduled for installation in 2016; (2) the full scale 3-dimensional imaging FDIRC prototype using the BaBar DIRC radiators which was designed for the SuperB detector at the Italian SuperB collider and uses precision timing not only for improving the angle reconstruction and TOF precision, but also to correct the chromatic dispersion; (3) the DIRCs being developed for the PANDA detector at FAIR that use elegant focusing optics and fast timing; and (4) the TORCH proposal being developed for an LHCb upgrade after 2019 which uses DIRC imaging with fast photon detectors to provide particle separation via particle TOF over a path length of 9.5m.

## 35.6. Gaseous detectors

**35.6.1. *Energy loss and charge transport in gases*** : Revised March 2010 by F. Sauli (CERN) and M. Titov (CEA Saclay).

Gas-filled detectors localize the ionization produced by charged particles, generally after charge multiplication. The statistics of ionization processes having asymmetries in the ionization trails, affect the coordinate determination deduced from the measurement of drift time, or of the center of gravity of the collected charge. For thin gas layers, the width of the energy loss distribution can be larger than its average, requiring multiple sample or truncated mean analysis to achieve good particle identification. In the truncated mean method for calculating  $\langle dE/dx \rangle$ , the ionization measurements along the track length are broken into many samples and then a fixed fraction of high-side (and sometimes also low-side) values are rejected [67].

The energy loss of charged particles and photons in matter is discussed in Sec. 34. Table 35.5 provides values of relevant parameters in some commonly used gases at NTP (normal temperature, 20° C, and pressure, 1 atm) for unit-charge minimum-ionizing particles (MIPs) [68–74]. Values often differ, depending on the source, so those in the table should be taken only as approximate. For different conditions and for mixtures, and neglecting internal energy transfer processes (*e.g.*, Penning effect), one can scale the

density,  $N_P$ , and  $N_T$  with temperature and pressure assuming a perfect gas law.

**Table 35.5:** Properties of noble and molecular gases at normal temperature and pressure (NTP: 20° C, one atm).  $E_X$ ,  $E_I$ : first excitation, ionization energy;  $W_I$ : average energy per ion pair;  $dE/dx|_{\min}$ ,  $N_P$ ,  $N_T$ : differential energy loss, primary and total number of electron-ion pairs per cm, for unit charge minimum ionizing particles.

Gas	Density, mg cm <sup>-3</sup>	$E_x$ eV	$E_I$ eV	$W_I$ eV	$dE/dx _{\min}$ keV cm <sup>-1</sup>	$N_P$ cm <sup>-1</sup>	$N_T$ cm <sup>-1</sup>
He	0.179	19.8	24.6	41.3	0.32	3.5	8
Ne	0.839	16.7	21.6	37	1.45	13	40
Ar	1.66	11.6	15.7	26	2.53	25	97
Xe	5.495	8.4	12.1	22	6.87	41	312
CH <sub>4</sub>	0.667	8.8	12.6	30	1.61	28	54
C <sub>2</sub> H <sub>6</sub>	1.26	8.2	11.5	26	2.91	48	112
iC <sub>4</sub> H <sub>10</sub>	2.49	6.5	10.6	26	5.67	90	220
CO <sub>2</sub>	1.84	7.0	13.8	34	3.35	35	100
CF <sub>4</sub>	3.78	10.0	16.0	54	6.38	63	120

When an ionizing particle passes through the gas it creates electron-ion pairs, but often the ejected electrons have sufficient energy to further ionize the medium. As shown in Table 35.5, the total number of electron-ion pairs ( $N_T$ ) is usually a few times larger than the number of primaries ( $N_P$ ).

The probability for a released electron to have an energy  $E$  or larger follows an approximate  $1/E^2$  dependence (Rutherford law), shown in Fig. 35.3 for Ar/CH<sub>4</sub> at NTP (dotted line, left scale). More detailed estimates taking into account the electronic structure of the medium are shown in the figure, for three values of the particle velocity factor  $\beta\gamma$  [69]. The dot-dashed line provides, on the right scale, the practical range of electrons (including scattering) of energy  $E$ . As an example, about 0.6% of released electrons have 1 keV or more energy, substantially increasing the ionization loss rate. The practical range of 1 keV electrons in argon (dot-dashed line, right scale) is 70  $\mu\text{m}$  and this can contribute to the error in the coordinate determination.

The number of electron-ion pairs per primary ionization, or cluster size, has an exponentially decreasing probability; for argon, there is about 1% probability for primary clusters to contain ten or more electron-ion pairs [70].

Once released in the gas, and under the influence of an applied electric field, electrons and ions drift in opposite directions and diffuse towards the electrodes. The scattering cross section is determined by the details of atomic and molecular structure. Therefore, the drift velocity and diffusion of electrons depend very strongly on the nature of the



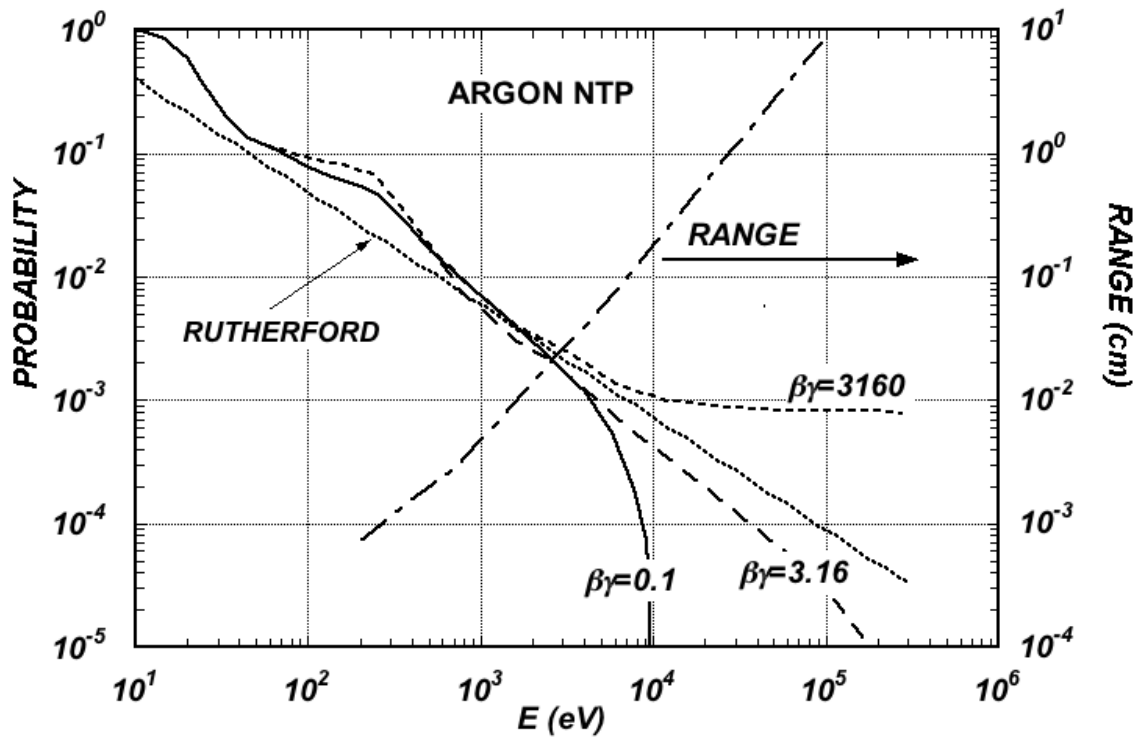


**Figure 35.3:** Probability of single collisions in which released electrons have an energy  $E$  or larger (left scale) and practical range of electrons in Ar/CH<sub>4</sub> (P10) at NTP (dot-dashed curve, right scale) [69].

gas, specifically on the inelastic cross-section involving the rotational and vibrational levels of molecules. In noble gases, the inelastic cross section is zero below excitation and ionization thresholds. Large drift velocities are achieved by adding polyatomic gases (usually CH<sub>4</sub>, CO<sub>2</sub>, or CF<sub>4</sub>) having large inelastic cross sections at moderate energies, which results in “cooling” electrons into the energy range of the Ramsauer-Townsend minimum (at  $\sim 0.5$  eV) of the elastic cross-section of argon. The reduction in both the total electron scattering cross-section and the electron energy results in a large increase of electron drift velocity (for a compilation of electron-molecule cross sections see Ref. 71). Another principal role of the polyatomic gas is to absorb the ultraviolet photons emitted by the excited noble gas atoms. Extensive collections of experimental data [72] and theoretical calculations based on transport theory [73] permit estimates of drift and diffusion properties in pure gases and their mixtures. In a simple approximation, gas kinetic theory provides the drift velocity  $v$  as a function of the mean collision time  $\tau$  and the electric field  $E$ :  $v = eE\tau/m_e$  (Townsend’s expression). Values of drift velocity and diffusion for some commonly used gases at NTP are given in Fig. 35.4 and Fig. 35.5. These have been computed with the MAGBOLTZ program [74]. For different conditions, the horizontal axis must be scaled inversely with the gas density. Standard deviations for longitudinal ( $\sigma_L$ ) and transverse diffusion ( $\sigma_T$ ) are given for one cm of drift, and scale with the the square root of the drift distance. Since the collection time is inversely

proportional to the drift velocity, diffusion is less in gases such as  $\text{CF}_4$  that have high drift velocities. In the presence of an external magnetic field, the Lorentz force acting on electrons between collisions deflects the drifting electrons and modifies the drift properties. The electron trajectories, velocities and diffusion parameters can be computed with MAGBOLTZ. A simple theory, the friction force model, provides an expression for the vector drift velocity  $\mathbf{v}$  as a function of electric and magnetic field vectors  $\mathbf{E}$  and  $\mathbf{B}$ , of the Larmor frequency  $\omega = eB/m_e$ , and of the mean collision time  $\tau$ :

$$\mathbf{v} = \frac{e}{m_e} \frac{\tau}{1 + \omega^2 \tau^2} \left( \mathbf{E} + \frac{\omega \tau}{B} (\mathbf{E} \times \mathbf{B}) + \frac{\omega^2 \tau^2}{B^2} (\mathbf{E} \cdot \mathbf{B}) \mathbf{B} \right) \quad (35.13)$$

To a good approximation, and for moderate fields, one can assume that the energy of the electrons is not affected by  $B$ , and use for  $\tau$  the values deduced from the drift velocity at  $B = 0$  (the Townsend expression). For  $\mathbf{E}$  perpendicular to  $\mathbf{B}$ , the drift angle to the relative to the electric field vector is  $\tan \theta_B = \omega \tau$  and  $v = (E/B)(\omega \tau / \sqrt{1 + \omega^2 \tau^2})$ . For parallel electric and magnetic fields, drift velocity and longitudinal diffusion are not affected, while the transverse diffusion can be strongly reduced:  $\sigma_T(B) = \sigma_T(B = 0) / \sqrt{1 + \omega^2 \tau^2}$ . The dotted line in Fig. 35.5 represents  $\sigma_T$  for the classic Ar/ $\text{CH}_4$  (90:10) mixture at 4 T. Large values of  $\omega \tau \sim 20$  at 5 T are consistent with the measurement of diffusion coefficient in Ar/ $\text{CF}_4$ / $\text{iC}_4\text{H}_{10}$  (95:3:2). This reduction is exploited in time projection chambers (Sec. 35.6.5) to improve spatial resolution.

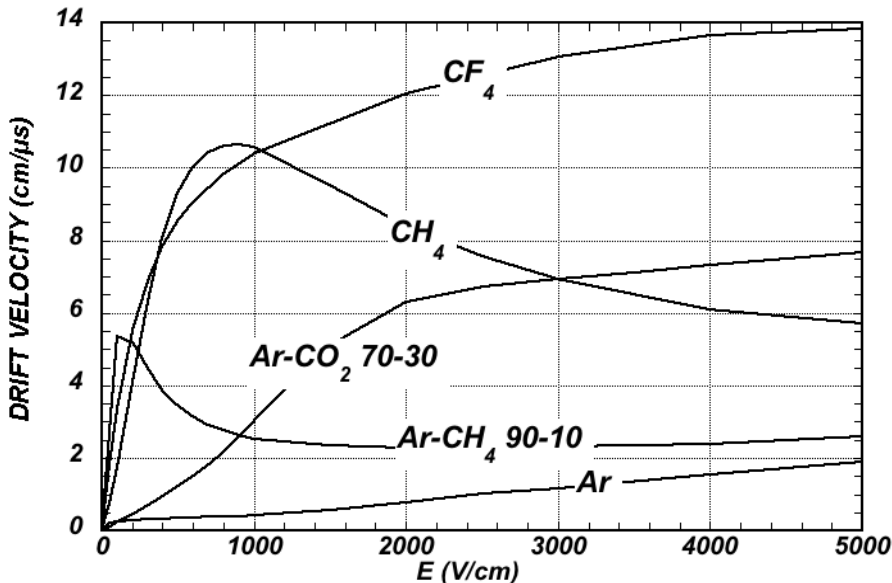


**Figure 35.4:** Computed electron drift velocity as a function of electric field in several gases at NTP and  $B = 0$  [74].

In mixtures containing electronegative molecules, such as  $\text{O}_2$  or  $\text{H}_2\text{O}$ , electrons can be captured to form negative ions. Capture cross-sections are strongly energy-dependent, and therefore the capture probability is a function of applied field. For example, the electron is attached to the oxygen molecule at energies below 1 eV. The three-body

electron attachment coefficients may differ greatly for the same additive in different mixtures. As an example, at moderate fields (up to 1 kV/cm) the addition of 0.1% of oxygen to an Ar/CO<sub>2</sub> mixture results in an electron capture probability about twenty times larger than the same addition to Ar/CH<sub>4</sub>.

Carbon tetrafluoride is not electronegative at low and moderate fields, making its use attractive as drift gas due to its very low diffusion. However, CF<sub>4</sub> has a large electron capture cross section at fields above  $\sim 8$  kV/cm, before reaching avalanche field strengths. Depending on detector geometry, some signal reduction and resolution loss can be expected using this gas.

If the electric field is increased sufficiently, electrons gain enough energy between collisions to ionize molecules. Above a gas-dependent threshold, the mean free path for ionization,  $\lambda_i$ , decreases exponentially with the field; its inverse,  $\alpha = 1/\lambda_i$ , is the first Townsend coefficient. In wire chambers, most of the increase of avalanche particle density occurs very close to the anode wires, and a simple electrostatic consideration shows that the largest fraction of the detected signal is due to the motion of positive ions receding from the wires. The electron component, although very fast, contributes very little to the signal. This determines the characteristic shape of the detected signals in the proportional mode: a fast rise followed by a gradual increase. The slow component, the so-called “ion tail” that limits the time resolution of the detector, is usually removed by differentiation of the signal. In uniform fields,  $N_0$  initial electrons multiply over a length  $x$  forming an electron avalanche of size  $N = N_0 e^{\alpha x}$ ;  $N/N_0$  is the gain of the detector. Fig. 35.6 shows examples of Townsend coefficients for several gas mixtures, computed with MAGBOLTZ [74].

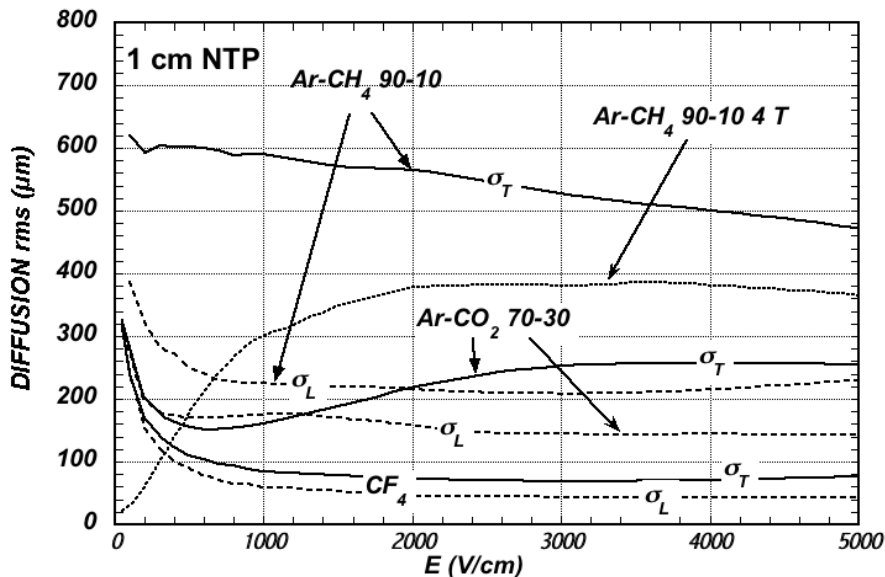


**Figure 35.5:** Electron longitudinal diffusion ( $\sigma_L$ ) (dashed lines) and transverse diffusion ( $\sigma_T$ ) (full lines) for 1 cm of drift at NTP and  $B = 0$ . The dotted line shows  $\sigma_T$  for the P10 mixture at 4 T [74].

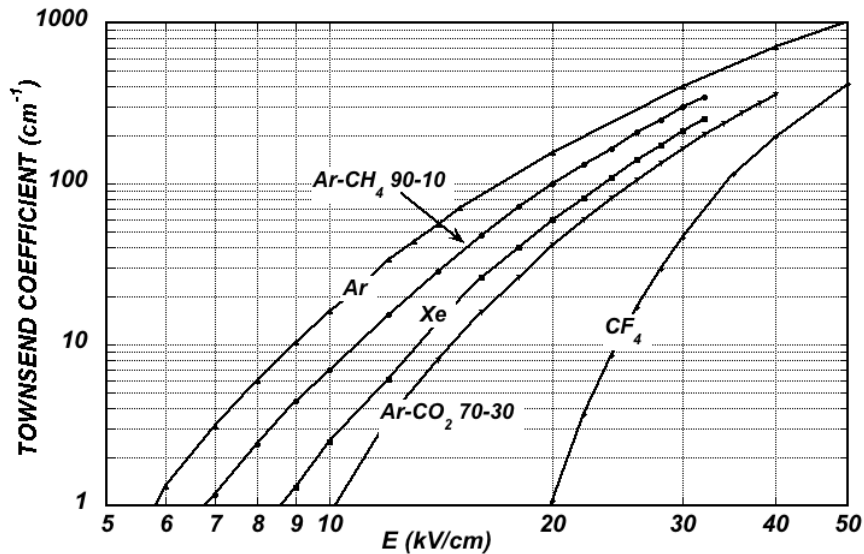


**Figure 35.6:** Computed first Townsend coefficient  $\alpha$  as a function of electric field in several gases at NTP [74].

Positive ions released by the primary ionization or produced in the avalanches drift and diffuse under the influence of the electric field. Negative ions may also be produced by electron attachment to gas molecules. The drift velocity of ions in the fields encountered in gaseous detectors (up to few kV/cm) is typically about three orders of magnitude less than for electrons. The ion mobility  $\mu$ , the ratio of drift velocity to electric field, is constant for a given ion type up to very high fields. Values of mobility at NTP for ions in their own and other gases are given in Table 35.6 [75]. For different temperatures and pressures, the mobility can be scaled inversely with the density assuming an ideal gas law. For mixtures, due to a very effective charge transfer mechanism, only ions with the lowest ionization potential survive after a short path in the gas. Both the lateral and transverse diffusion of ions are proportional to the square root of the drift time, with a coefficient that depends on temperature but not on the ion mass. Accumulation of ions in the gas drift volume may induce field distortions (see Sec. 35.6.5).

**35.6.2. Multi-Wire Proportional and Drift Chambers :** Revised March 2010 by Fabio Sauli (CERN) and Maxim Titov (CEA Saclay).

Single-wire counters that detect the ionization produced in a gas by a charged particle, followed by charge multiplication and collection around a thin wire have been used for decades. Good energy resolution is obtained in the proportional amplification mode, while very large saturated pulses can be detected in the streamer and Geiger modes [3].

Multiwire proportional chambers (MWPCs) [76,77], introduced in the late '60's, detect, localize and measure energy deposit by charged particles over large areas. A mesh of parallel anode wires at a suitable potential, inserted between two cathodes, acts almost as a set of independent proportional counters (see Fig. 35.7a). Electrons released in the gas volume drift towards the anodes and produce avalanches in the increasing field. Analytic expressions for the electric field can be found in many textbooks. The fields close to the wires  $E(r)$ , in the drift region  $E_D$ , and the capacitance  $C$  per unit length of

**Table 35.6:** Mobility of ions in gases at NTP [75].

Gas	Ion	Mobility $\mu$ ( $\text{cm}^2 \text{V}^{-1} \text{s}^{-1}$ )
He	He <sup>+</sup>	10.4
Ne	Ne <sup>+</sup>	4.7
Ar	Ar <sup>+</sup>	1.54
Ar/CH <sub>4</sub>	CH <sub>4</sub> <sup>+</sup>	1.87
Ar/CO <sub>2</sub>	CO <sub>2</sub> <sup>+</sup>	1.72
CH <sub>4</sub>	CH <sub>4</sub> <sup>+</sup>	2.26
CO <sub>2</sub>	CO <sub>2</sub> <sup>+</sup>	1.09

**Table 35.7:** Maximum tension  $T_M$  and stable unsupported length  $L_M$  for tungsten wires with spacing  $s$ , operated at  $V_0 = 5$  kV. No safety factor is included.

Wire diameter ( $\mu\text{m}$ )	$T_M$ (newton)	$s$ (mm)	$L_M$ (cm)
10	0.16	1	25
20	0.65	2	85

anode wire are approximately given by

$$E(r) = \frac{CV_0}{2\pi\epsilon_0} \frac{1}{r} \quad E_D = \frac{CV_0}{2\epsilon_0 s} \quad C = \frac{2\pi\epsilon_0}{\pi(\ell/s) - \ln(2\pi a/s)}, \quad (35.14)$$

where  $r$  is the distance from the center of the anode,  $s$  the wire spacing,  $\ell$  and  $V_0$  the distance and potential difference between anode and cathode, and  $a$  the anode wire radius.

Because of electrostatic forces, anode wires are in equilibrium only for a perfect geometry. Small deviations result in forces displacing the wires alternatively below and above the symmetry plane, sometimes with catastrophic results. These displacement forces are countered by the mechanical tension of the wire, up to a maximum unsupported stable length,  $L_M$  [67], above which the wire deforms:

$$L_M = \frac{s}{CV_0} \sqrt{4\pi\epsilon_0 T_M} \quad (35.15)$$

The maximum tension  $T_M$  depends on the wire diameter and modulus of elasticity. Table 35.7 gives approximate values for tungsten and the corresponding maximum stable wire length under reasonable assumptions for the operating voltage ( $V_0 = 5$  kV) [78]. Internal supports and spacers can be used in the construction of longer detectors to overcome limits on the wire length imposed by Eq. (35.15).

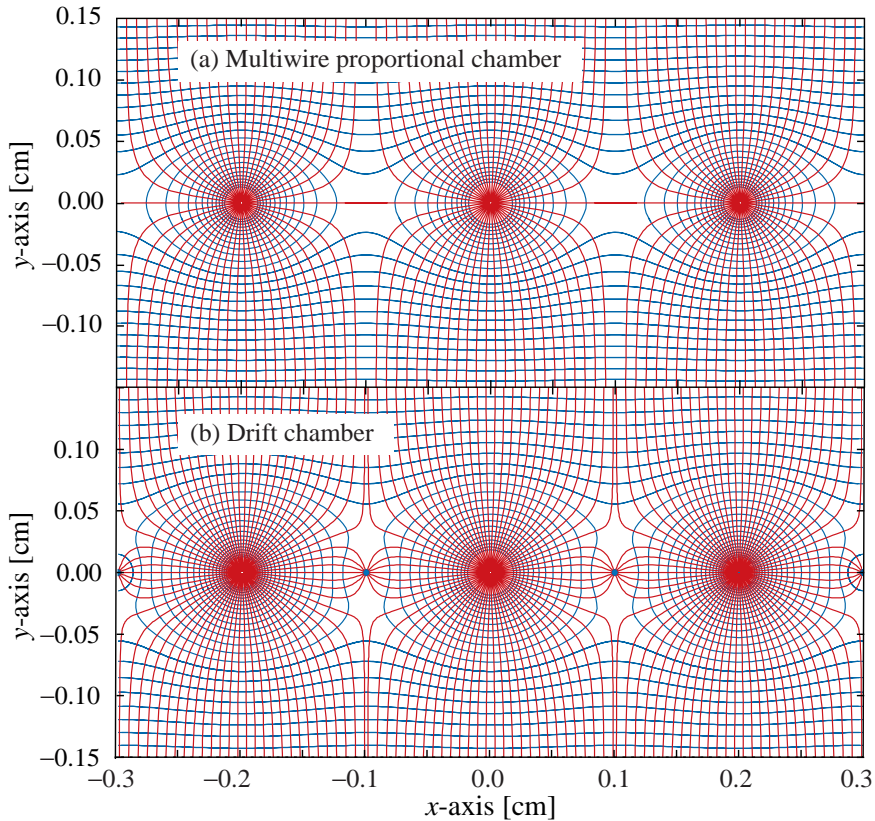


**Figure 35.7:** Electric field lines and equipotentials in (a) a multiwire proportional chamber and (b) a drift chamber.

Detection of charge on the wires over a predefined threshold provides the transverse coordinate to the wire with an accuracy comparable to that of the wire spacing. The coordinate along each wire can be obtained by measuring the ratio of collected charge at the two ends of resistive wires. Making use of the charge profile induced on segmented cathodes, the so-called center-of gravity (COG) method, permits localization of tracks to sub-mm accuracy. Due to the statistics of energy loss and asymmetric ionization clusters, the position accuracy is  $\sim 50 \mu\text{m}$  rms for tracks perpendicular to the wire plane, but degrades to  $\sim 250 \mu\text{m}$  at  $30^\circ$  to the normal [79]. The intrinsic bi-dimensional characteristic of the COG readout has found numerous applications in medical imaging.

Drift chambers, developed in the early '70's, can be used to estimate the longitudinal position of a track by exploiting the arrival time of electrons at the anodes if the time of interaction is known [80]. The distance between anode wires is usually several cm, allowing coverage of large areas at reduced cost. In the original design, a thicker wire (the field wire) at the proper voltage, placed between the anode wires, reduces the field at the mid-point between anodes and improves charge collection (Fig. 35.7b). In some drift chamber designs, and with the help of suitable voltages applied to field-shaping electrodes, the electric field structure is adjusted to improve the linearity of space-to-drift-time relation, resulting in better spatial resolution [81].

Drift chambers can reach a longitudinal spatial resolution from timing measurement of

order 100  $\mu\text{m}$  (rms) or better for minimum ionizing particles, depending on the geometry and operating conditions. However, a degradation of resolution is observed [82] due to primary ionization statistics for tracks close to the anode wires, caused by the spread in arrival time of the nearest ionization clusters. The effect can be reduced by operating the detector at higher pressures. Sampling the drift time on rows of anodes led to the concept of multiple arrays such as the multi-drift module [83] and the JET chamber [84]. A measurement of drift time, together with the recording of charge sharing from the two ends of the anode wires provides the coordinates of segments of tracks. The total charge gives information on the differential energy loss and is exploited for particle identification. The time projection chamber (TPC) [85] combines a measurement of drift time and charge induction on cathodes, to obtain excellent tracking for high multiplicity topologies occurring at moderate rates (see Sec. 35.6.5). In all cases, a good knowledge of electron drift velocity and diffusion properties is required. This has to be combined with the knowledge of the electric fields in the structures, computed with commercial or custom-developed software [74,86]. For an overview of detectors exploiting the drift time for coordinate measurement see Refs. 6 and 67.

Multiwire and drift chambers have been operated with a variety of gas fillings and operating modes, depending on experimental requirements. The so-called “Magic Gas,” a mixture of argon, isobutane and Freon [77], permits very high and saturated gains ( $\sim 10^6$ ). This gas mixture was used in early wire chambers, but was found to be susceptible to severe aging processes. With present-day electronics, proportional gains around  $10^4$  are sufficient for detection of minimum ionizing particles, and noble gases with moderate amounts of polyatomic gases, such as methane or carbon dioxide, are used.

Although very powerful in terms of performance, multi-wire structures have reliability problems when used in harsh or hard-to-access environments, since a single broken wire can disable the entire detector. Introduced in the '80's, straw and drift tube systems make use of large arrays of wire counters encased in individual enclosures, each acting as an independent wire counter [87]. Techniques for low-cost mass production of these detectors have been developed for large experiments, such as the Transition Radiation Tracker and the Drift Tubes arrays for CERN's LHC experiments [88].

**35.6.3. High Rate Effects** : Revised March 2010 by Fabio Sauli (CERN) and Maxim Titov (CEA Saclay).

The production of positive ions in the avalanches and their slow drift before neutralization result in a rate-dependent accumulation of positive charge in the detector. This may result in significant field distortion, gain reduction and degradation of spatial resolution. As shown in Fig. 35.8 [89], the proportional gain drops above a charge production rate around  $10^9$  electrons per second and mm of wire, independently of the avalanche size. For a proportional gain of  $10^4$  and 100 electrons per track, this corresponds to a particle flux of  $10^3 \text{ s}^{-1} \text{ mm}^{-1}$  (1 kHz/mm<sup>2</sup> for 1 mm wire spacing).

At high radiation fluxes, a fast degradation of detectors due to the formation of polymers deposits (aging) is often observed. The process has been extensively investigated, often with conflicting results. Several causes have been identified, including organic pollutants and silicone oils. Addition of small amounts of water in many (but not all) cases has been shown to extend the lifetime of the detectors. Addition of fluorinated

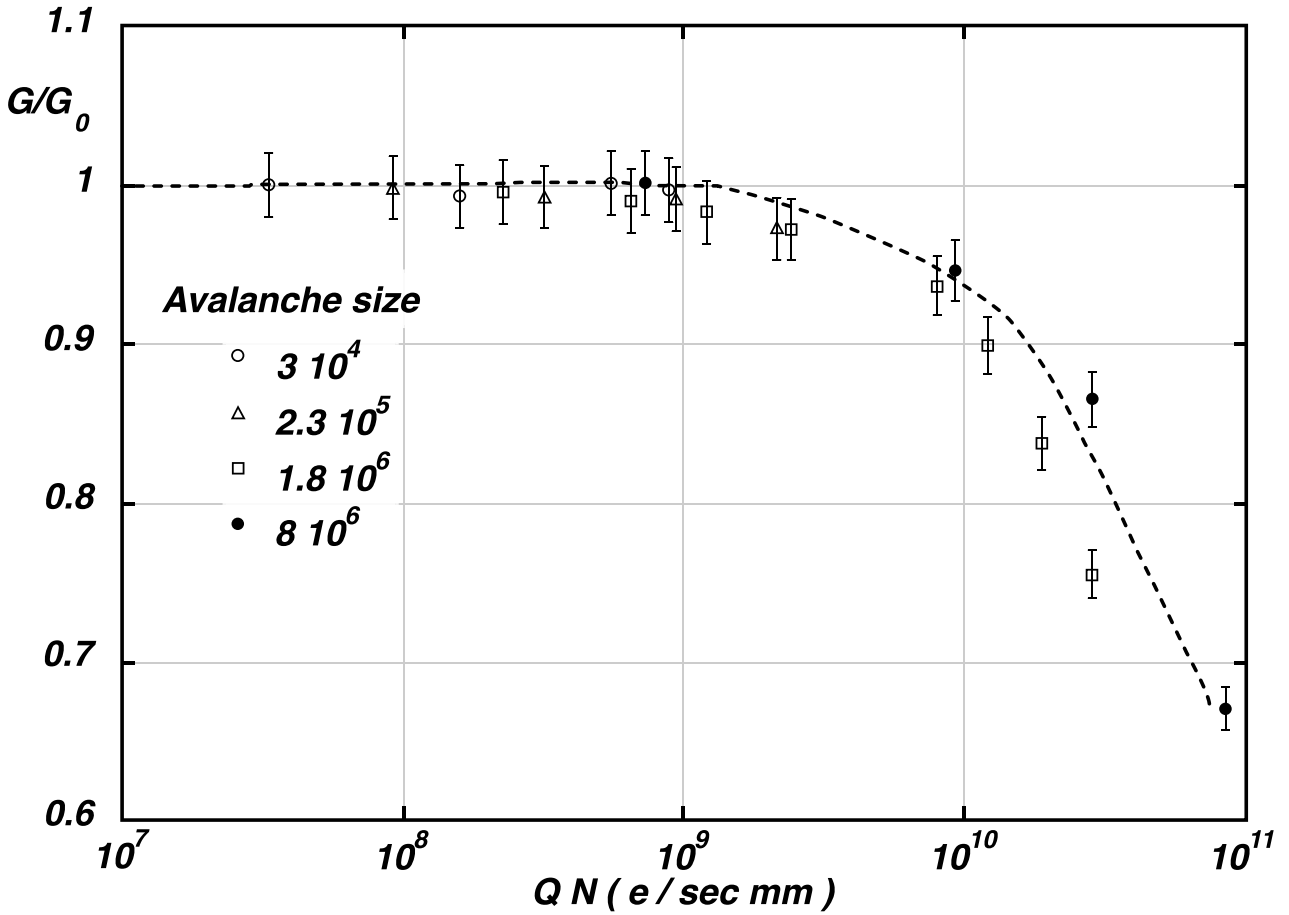


**Figure 35.8:** Charge rate dependence of normalized gas gain  $G/G_0$  (relative to zero counting rate) in proportional thin-wire detectors [89].  $Q$  is the total charge in single avalanche;  $N$  is the particle rate per wire length.

gases (*e.g.*,  $\text{CF}_4$ ) or oxygen may result in an etching action that can overcome polymer formation, or even eliminate already existing deposits. However, the issue of long-term survival of gas detectors with these gases is controversial [90]. Under optimum operating conditions, a total collected charge of a few coulombs per cm of wire can usually be reached before noticeable degradation occurs. This corresponds, for one mm spacing and at a gain of  $10^4$ , to a total particle flux of  $\sim 10^{14}$  MIPs/cm<sup>2</sup>.

**35.6.4. Micro-Pattern Gas Detectors :** Revised March 2010 by Fabio Sauli (CERN) and Maxim Titov (CEA Saclay)

Despite various improvements, position-sensitive detectors based on wire structures are limited by basic diffusion processes and space charge effects to localization accuracies of 50–100  $\mu\text{m}$  [91]. Modern photolithographic technology led to the development of novel Micro-Pattern Gas Detector (MPGD) concepts [92], revolutionizing cell size limitations for many gas detector applications. By using pitch size of a few hundred  $\mu\text{m}$ , an order of magnitude improvement in granularity over wire chambers, these detectors offer intrinsic high rate capability ( $> 10^6$  Hz/mm<sup>2</sup>), excellent spatial resolution ( $\sim 30 \mu\text{m}$ ), multi-particle resolution ( $\sim 500 \mu\text{m}$ ), and single photo-electron time resolution in the ns range.



The Micro-Strip Gas Chamber (MSGC), invented in 1988, was the first of the micro-structure gas chambers [93]. It consists of a set of tiny parallel metal strips laid on a thin resistive support, alternatively connected as anodes and cathodes. Owing to the small anode-to-cathode distance ( $\sim 100 \mu\text{m}$ ), the fast collection of positive ions reduces space charge build-up, and provides a greatly increased rate capability. Unfortunately, the fragile electrode structure of the MSGC turned out to be easily destroyed by discharges induced by heavily ionizing particles [94]. Nevertheless, detailed studies of their properties, and in particular, on the radiation-induced processes leading to discharge breakdown, led to the development of the more powerful devices: GEM and Micromegas. These have improved reliability and radiation hardness. The absence of space-charge effects in GEM detectors at the highest rates reached so far and the fine granularity of MPGDs improve the maximum rate capability by more than two orders of magnitude (Fig. 35.9) [81,95]. Even larger rate capability has been reported for Micromegas [96].

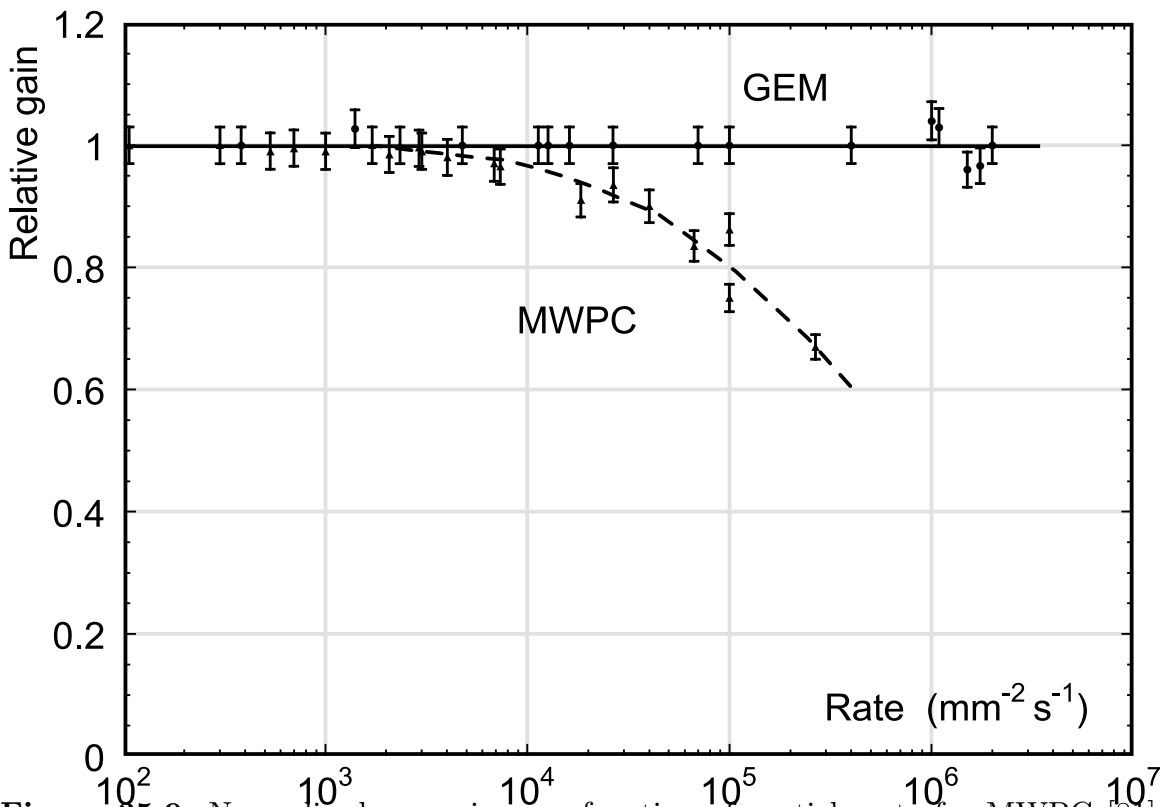


**Figure 35.9:** Normalized gas gain as a function of particle rate for MWPC [81] and GEM [95].

The Gas Electron Multiplier (GEM) detector consists of a thin-foil copper-insulator-copper sandwich chemically perforated to obtain a high density of holes in which avalanches occur [97]. The hole diameter is typically between  $25 \mu\text{m}$  and  $150 \mu\text{m}$ , while the corresponding distance between holes varies between  $50 \mu\text{m}$  and  $200 \mu\text{m}$ . The central insulator is usually (in the original design) the polymer Kapton, with a thickness of  $50 \mu\text{m}$ . Application of a potential difference between the two sides of the GEM generates the electric fields indicated in Fig. 35.10. Each hole acts as an independent proportional

counter. Electrons released by the primary ionization particle in the upper conversion region (above the GEM foil) drift into the holes, where charge multiplication occurs in the high electric field (50–70 kV/cm). Most of avalanche electrons are transferred into the gap below the GEM. Several GEM foils can be cascaded, allowing the multi-layer GEM detectors to operate at overall gas gain above  $10^4$  in the presence of highly ionizing particles, while strongly reducing the risk of discharges. This is a major advantage of the GEM technology [98]. Localization can then be performed by collecting the charge on a patterned one- or two-dimensional readout board of arbitrary pattern, placed below the last GEM.

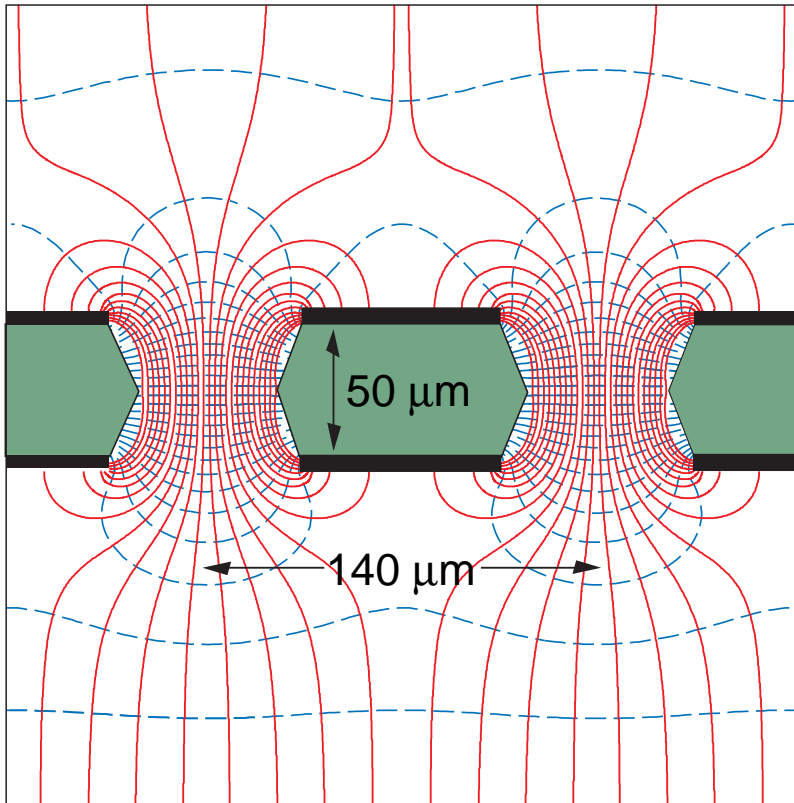


**Figure 35.10:** Schematic view and typical dimensions of the hole structure in the GEM amplification cell. Electric field lines (solid) and equipotentials (dashed) are shown.

The micro-mesh gaseous structure (Micromegas) is a thin parallel-plate avalanche counter, as shown in Fig. 35.11 [99]. It consists of a drift region and a narrow multiplication gap (25–150  $\mu\text{m}$ ) between a thin metal grid (micromesh) and the readout electrode (strips or pads of conductor printed on an insulator board). Electrons from the primary ionization drift through the holes of the mesh into the narrow multiplication gap, where they are amplified. The electric field is homogeneous both in the drift (electric field  $\sim 1$  kV/cm) and amplification (50–70 kV/cm) gaps. In the narrow multiplication region, gain variations due to small variations of the amplification gap are approximately compensated by an inverse variation of the amplification coefficient, resulting in a more

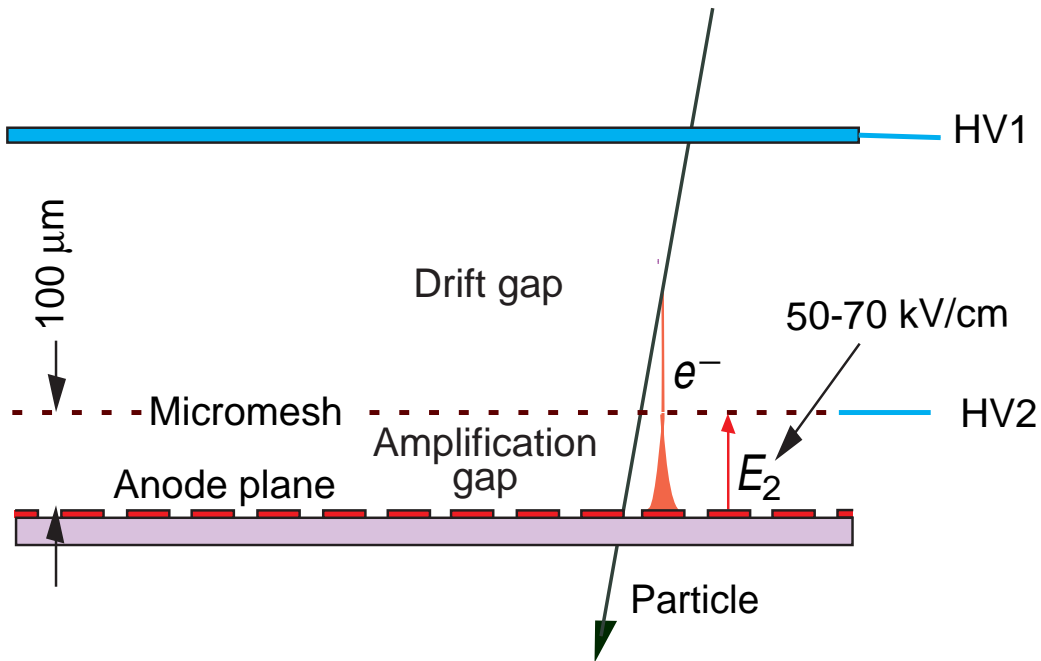


**Figure 35.11:** Schematic drawing of the Micromegas detector.

uniform gain. The small amplification gap produces a narrow avalanche, giving rise to excellent spatial resolution:  $12\ \mu\text{m}$  accuracy, limited by the micro-mesh pitch, has been achieved for MIPs, as well as very good time resolution and energy resolution ( $\sim 12\%$  FWHM with  $6\ \text{keV}$  x rays) [100].

The performance and robustness of GEM and Micromegas have encouraged their use in high-energy and nuclear physics, UV and visible photon detection, astroparticle and neutrino physics, neutron detection and medical physics. Most structures were originally optimized for high-rate particle tracking in nuclear and high-energy physics experiments. COMPASS, a high-luminosity experiment at CERN, pioneered the use of large-area ( $\sim 40 \times 40\ \text{cm}^2$ ) GEM and Micromegas detectors close to the beam line with particle rates of  $25\ \text{kHz}/\text{mm}^2$ . Both technologies achieved a tracking efficiency of close to  $100\%$  at gas gains of about  $10^4$ , a spatial resolution of  $70\text{--}100\ \mu\text{m}$  and a time resolution of  $\sim 10\ \text{ns}$ . GEM detectors are also used for triggering in the LHCb Muon System and for tracking in the TOTEM Telescopes. Both GEM and Micromegas devices are foreseen for the upgrade of the LHC experiments and for one of the readout options for the Time Projection Chamber (TPC) at the International Linear Collider (ILC). The development of new fabrication techniques—“bulk” Micromegas technology [101] and single-mask GEMs [102]—is a big step toward industrial production of large-size MPGDs. In some applications requiring very large-area coverage with moderate spatial resolution, coarse macro-patterned detectors, such as Thick GEMs (THGEM) [103] or patterned resistive-plate devices [104] might offer economically interesting solutions.

Sensitive and low-noise electronics enlarge the range of the MPGD applications. Recently, the GEM and Micromegas detectors were read out by high-granularity ( $\sim 50\ \mu\text{m}$  pitch) CMOS chips assembled directly below the GEM or Micromegas amplification structures [105]. These detectors use the bump-bonding pads of a pixel chip as an

integrated charge collecting anode. With this arrangement signals are induced at the input gate of a charge-sensitive preamplifier (top metal layer of the CMOS chip). Every pixel is then directly connected to the amplification and digitization circuits, integrated in the underlying active layers of the CMOS technology, yielding timing and charge measurements as well as precise spatial information in 3D.

The operation of a MPGD with a Timepix CMOS chip has demonstrated the possibility of reconstructing 3D-space points of individual primary electron clusters with  $\sim 30 \mu\text{m}$  spatial resolution and event-time resolution with nanosecond precision. This has become indispensable for tracking and triggering and also for discriminating between ionizing tracks and photon conversions. The GEM, in conjunction with a CMOS ASIC,\* can directly view the absorption process of a few keV x-ray quanta and simultaneously reconstruct the direction of emission, which is sensitive to the x-ray polarization. Thanks to these developments, a micro-pattern device with finely segmented CMOS readout can serve as a high-precision “electronic bubble chamber.” This may open new opportunities for x-ray polarimeters, detection of weakly interacting massive particles (WIMPs) and axions, Compton telescopes, and 3D imaging of nuclear recoils.

An elegant solution for the construction of the Micromegas with pixel readout is the integration of the amplification grid and CMOS chip by means of an advanced “wafer post-processing” technology [106]. This novel concept is called “Ingrid” (see Fig. 35.12). With this technique, the structure of a thin ( $1 \mu\text{m}$ ) aluminum grid is fabricated on top of an array of insulating pillars, which stands  $\sim 50 \mu\text{m}$  above the CMOS chip. The sub- $\mu\text{m}$  precision of the grid dimensions and avalanche gap size results in a uniform gas gain. The grid hole size, pitch and pattern can be easily adapted to match the geometry of any pixel readout chip.

Recent developments in radiation hardness research with state-of-the-art MPGDs are reviewed in Ref. 107. Earlier aging studies of GEM and Micromegas concepts revealed that they might be even less vulnerable to radiation-induced performance degradation than standard silicon microstrip detectors.

The RD51 collaboration was established in 2008 to further advance technological developments of micro-pattern detectors and associated electronic-readout systems for applications in basic and applied research [108].

**35.6.5. *Time-projection chambers*** : Written August 2015 by C. Lippmann (GSI Helmholtzzentrum für Schwerionenforschung, Darmstadt, Germany)

The Time Projection Chamber (TPC) concept was invented by David Nygren in the late 1970’s [85]. It consists of a cylindrical or square field cage filled with a detection medium that is usually a gas or a liquid. Charged particles produce tracks of ionization electrons that drift in a uniform electric field towards a position-sensitive amplification stage which provides a 2D projection of the particle trajectories. The third coordinate can be calculated from the arrival times of the drifted electrons. The start for this drift time measurement is usually derived from an external detector, e.g. a fast interaction trigger detector.

This section focuses on the gas-filled TPCs that are typically used in particle or nuclear

---

\* Application Specific Integrated Circuit

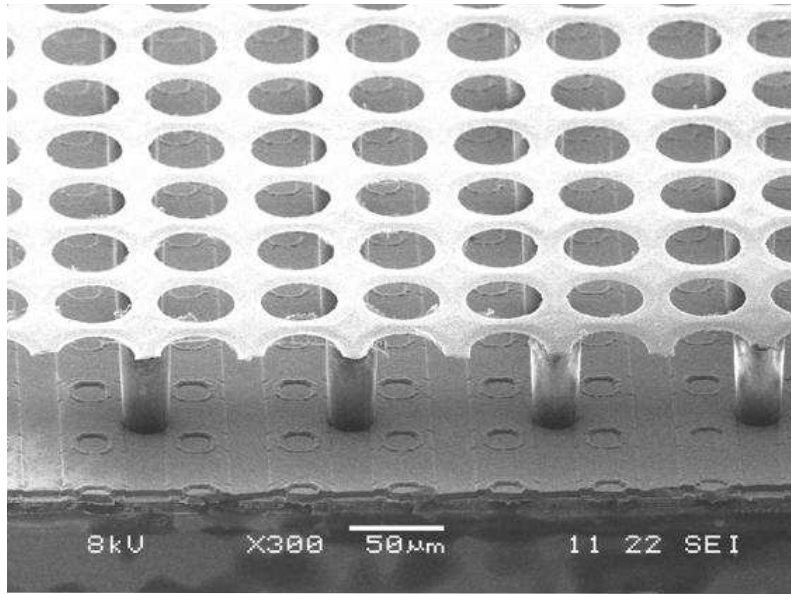


**Figure 35.12:** Photo of the Micromegas “Ingrid” detector. The grid holes can be accurately aligned with readout pixels of CMOS chip. The insulating pillars are centered between the grid holes, thus avoiding dead regions.

physics experiments at accelerators due to their low material budget. For neutrino physics (Sec. 35.10) or for detecting rare events (Sec. 36.4), on the contrary, usually high density and large active mass are required, and a liquid detection medium is favored.

The TPC enables full 3D measurements of charged particle tracks, which gives it a distinct advantage over other tracking detector designs which record information only in two-dimensional detector planes and have less overall segmentation. This advantage is often exploited for pattern recognition in events with large numbers of particles, e.g. heavy-ion collisions. Two examples of modern large-volume gaseous TPCs are shown in Fig. 35.13 and Fig. 35.14.

Identification of the charged particles crossing the TPC is possible by simultaneously measuring their momentum and specific energy deposit through ionisation ( $dE/dx$ ). The momentum, as well as the charge sign, are calculated from a helix fit to the particle trajectory in the presence of a magnetic field (typically parallel to the drift field). For this application, precise spatial measurements in the plane transverse to the magnetic field are most important. The specific energy deposit is estimated from many charge measurements along the particle trajectory (e.g. one measurement per anode wire or per row of readout pads). As the charge collected per readout segment depends on the track angle and on the ambient conditions, the measured values are corrected for the effective length of the track segments and for variations of the gas temperature and pressure. The most probable value of the corrected signal amplitudes provides the best estimator for the specific energy deposit (see Sec. 34.2.3); it is usually approximated by the truncated mean, i.e. the average of the 50%-70% smallest values. The resulting particle identification performance is illustrated in Fig. 35.15, for the ALICE TPC.

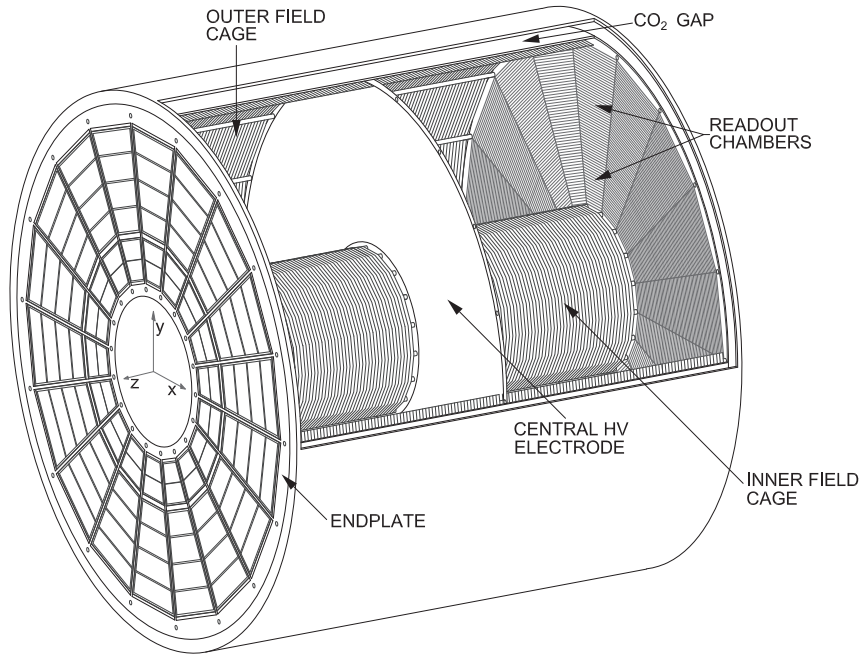


**Figure 35.13:** Schematic view of the ALICE TPC [109]. The drift volume with 5 m diameter is divided into two halves, each providing 2.5 m drift length.

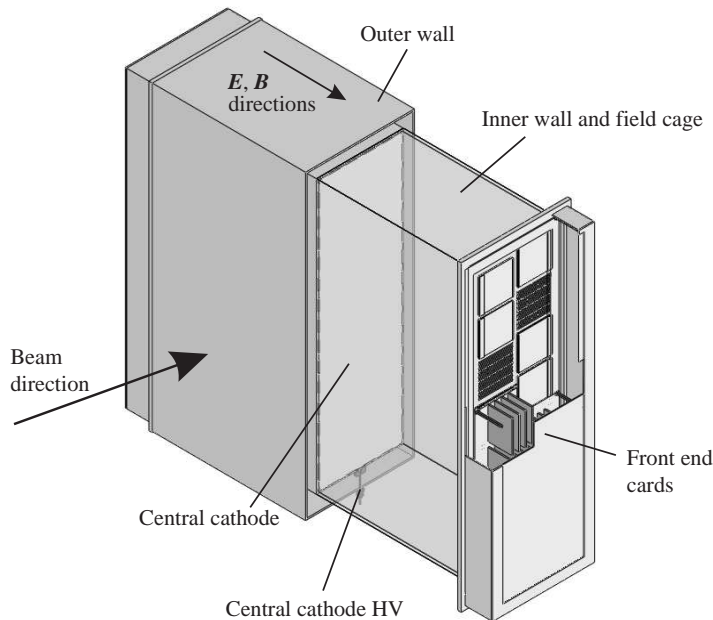


**Figure 35.14:** One of the 3 TPC modules for the near detector of the T2K experiment [110]. The size is  $2 \times 2 \times 0.8 \text{ m}^3$ . Micromegas devices are used for gas amplification and readout.

The dependence of the achievable energy resolution on the number of measurements

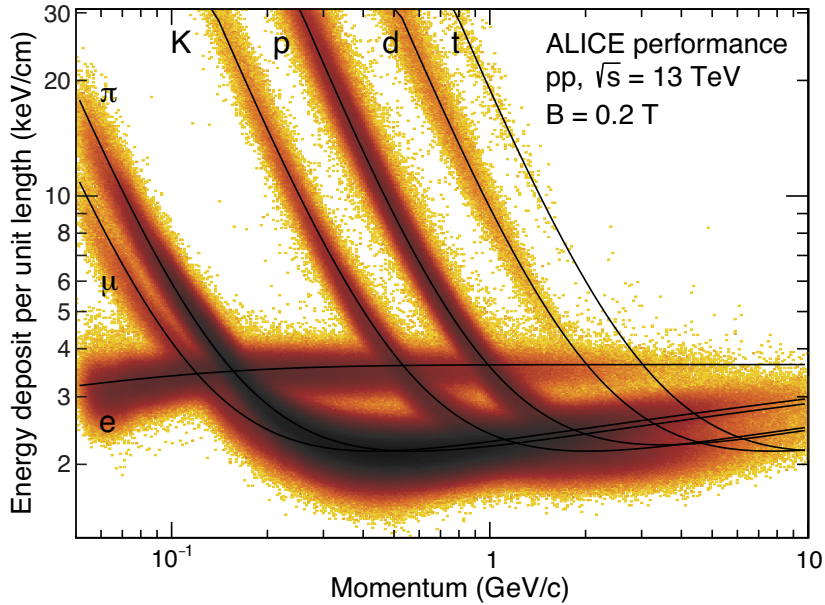


**Figure 35.15:** Energy deposit versus momentum measured in the ALICE TPC [111].

$N$ , on the thickness of the sampling layers  $t$ , and on the gas pressure  $P$  can be estimated using an empirical formula [112]:

$$\sigma_{dE/dx} = 0.41 N^{-0.43} (tP)^{-0.32}. \quad (35.16)$$

Typical values at nominal pressure are  $\sigma_{dE/dx} = 4.5$  to  $7.5\%$ , with  $t = 0.4$  to  $1.5$  cm and  $N = 40$  up to more than  $300$ . Due to the high gas pressure of  $8.5$  bar, the resolution achieved with the PEP-4/9 TPC was an unprecedented  $3\%$  [113].

The greatest challenges for a large TPC are due to the length of the drift of up to several meters. In particular, it can make the device sensitive to small distortions in the electric field. Such distortions can arise from a number of sources, e.g. imperfections in the field cage construction or the presence of ions in the drift volume. The electron drift in a TPC in the presence of a magnetic field is defined by Eq. (35.13). The  $\mathbf{E} \times \mathbf{B}$  term of Eq. (35.13) vanishes for perfectly aligned electric and magnetic fields, which can however be difficult to achieve in practice. Furthermore, the electron drift depends on the  $\omega\tau$  factor, which is defined by the chosen gas mixture and magnetic field strength. The electrons will tend to follow the magnetic field lines for  $\omega\tau > 1$  or the electric field lines for  $\omega\tau < 1$ . The former mode of operation makes the TPC less sensitive to non-uniformities of the electric field, which is usually desirable.

The drift of the ionization electrons is superposed with a random diffusion motion which degrades their position information. The ultimate resolution of a single position measurement is limited to around

$$\sigma_x = \frac{\sigma_D \sqrt{L}}{\sqrt{n}}, \quad (35.17)$$

where  $\sigma_D$  is the transverse diffusion coefficient for 1 cm drift,  $L$  is the drift length in cm and  $n$  is the effective number of electrons collected. Without a magnetic field,  $\sigma_{D,B=0} \sqrt{L}$  is typically a few mm after a drift of  $L = 100$  cm. However, in a strong magnetic field parallel to the drift field, a large value of  $\omega\tau$  can significantly reduce diffusion:

$$\frac{\sigma_{D,B>0}}{\sigma_{D,B=0}} = \frac{1}{\sqrt{1 + \omega^2\tau^2}}. \quad (35.18)$$

This factor can reach values of up to 10. In practice, the final resolution limit due to diffusion will typically be around  $\sigma_x = 100 \mu\text{m}$ .

The drift and diffusion of electrons depend strongly on the nature of the gas that is used. The optimal gas mixture varies according to the environment in which the TPC will operate. In all cases, the oxygen concentration must be kept very low (few ten parts per million in a large TPC) in order to avoid electron loss through attachment. Ideally, the drift velocity should depend only weakly on the electric field at the nominal operating condition. The classic Ar/CH<sub>4</sub> (90:10) mixture, known as P10, has a drift velocity maximum of 5 cm/ $\mu\text{s}$  at an electric field of only 125 V/cm (Fig. 35.4). In this regime, the electron arrival time is not affected by small variations in the ambient conditions. Moreover, low electric fields simplify the design and operation of the field cage. The mixture has a large transverse diffusion at  $B = 0$ , but this can be reduced significantly in a strong magnetic field due to the relatively large value of  $\omega\tau$ .

For certain applications, organic gases like CH<sub>4</sub> are not desirable, since they may cause aging. An alternative is to replace CH<sub>4</sub> with CO<sub>2</sub>. An Ar/CO<sub>2</sub> (90:10) mixture features a low transverse diffusion at all magnetic field strengths, but does not provide a saturated drift velocity for the typical electric fields used in TPCs (up to a few 100 V/cm), so it is quite sensitive to the ambient conditions. Freon admixtures like CF<sub>4</sub> can be an attractive option for a TPC as well, since the resulting gas mixtures provide high drift velocities at low electric fields. However, the use of CF<sub>4</sub> always needs to be thoroughly validated for compatibility with all materials of the detector and the gas system.

Historically, the amplification stages used in gaseous TPCs have been planes of anode wires operated in proportional mode. The performance is limited by effects related to the feature size of a few mm (wire spacing). Since near the wires the electric and magnetic fields are not parallel, the incoming ionisation electrons are displaced in the direction of the wires (“wire  $E \times B$  effect”), which degrades the resolution. The smaller feature sizes of Micro-Pattern Gas Detectors (MPGDs) like GEMs and Micromegas lead to many advantages as compared to wire planes (see Sec. 35.6.4). In particular,  $E \times B$  effects in the amplification stage are much smaller. Moreover, the signal induction process in MPGDs leads to a very narrow pad response, allowing for a much finer segmentation and improving the separation of two nearby tracks. Combinations of MPGDs with silicon sensors have resulted in the highest granularity readout systems so far (see Sec. 35.6.4). These devices make it possible to count the number of ionization clusters along the length of a track, which can, in principle, improve the particle identification capability. However, the big challenge for such a system is the huge number of read-out channels for a TPC of a typical size.

The accumulation of the positive ions created by the ionization from the particle tracks can lead to time-dependent distortions of the drift field. Due to their small drift velocity,



ions from many events may coexist in the drift volume. To reduce the effect of such a build-up of space charge, Argon can be replaced by Neon as the main component of the gas mixture. Neon features a lower number of ionisation electrons per unit of track length (see Table 35.5) and a higher ion mobility (see Table 35.6).

Of much greater concern are the ions produced in the gas amplification stage. In order to prevent them from entering the drift volume, large TPCs built until now usually have a gating grid. The gating grid can be switched to transparent mode (usually in the presence of an interaction trigger) to allow the ionization electrons to pass into the amplification region. After all electrons have reached the amplification region, it is usually closed such that it is rendered opaque to electrons and ions.

Alternatively, new readout schemes are being developed using MPGDs. These can be optimized in a way that they release many fewer positive ions than wire planes operating at the same effective gain. This is an exciting possibility for future TPCs.

**35.6.6. Transition radiation detectors (TRD's) :** Revised August 2017 by P. Nevski (BNL) and A. Romaniouk (Moscow Eng. & Phys. Inst.)

Transition radiation (TR) x-rays are produced when a highly relativistic particle ( $\gamma \gtrsim 10^3$ ) crosses a refractive index interface, as discussed in Sec. 34.7. Since the TR yield is about 1% per boundary crossing, radiation from multiple surface crossings is used in practical detectors. The x-rays, ranging from a few keV to a few dozen keV or more, are emitted in a forward direction at small angles ( $\sim$  few mrad) to the particle trajectory. The TR intensity for a single boundary crossing always increases with  $\gamma$ , but, for multiple boundary crossings, interference leads to saturation above a Lorentz factor  $\gamma_{\text{sat}} = 0.6 \omega_1 \sqrt{\ell_1 \ell_2} / c$  [114], where  $\omega_1$  is the radiator material plasma frequency,  $\ell_1$  is its thickness, and  $\ell_2$  the spacing. The probability density function of TR is a fairly complex function of  $\gamma$ , radiator parameters, angle ( $\theta$ ) and photon energy ( $\omega$ ). Integration over the angle yields the TR spectrum, which typically features many maxima (see Sec. 34.7). Most of the radiation is emitted near the last maximum of the spectra determined by radiator material parameters at  $\omega_{\text{max}} = \ell_1 \omega_1^2 / 2\pi c$ . The effective TR photon emission starts at about  $\gamma_{\text{thr}} = \ell_1 \omega_1 / c$ . By varying radiator parameters one may optimize the particle separation for a given range of the  $\gamma$ -factor. The angular distribution of TR photons has a few maxima and extends up to  $\theta_{\text{max}} = (1/\gamma^2 + \omega_1^2/\omega^2)^{1/2}$  (see Ref. 87 in Sec. 34.7). The largest part of the TR energy is emitted around the most probable angle  $\theta = (1/\gamma^2 + \omega_2^2/\omega^2)^{1/2}$ , where  $\omega_2$  is the plasma frequency of the gas surrounding the radiator material elements.

In the simplest concept, a detector module might consist of low- $Z$  TR radiator followed by a high- $Z$  active layer made of proportional counters filled with a Xe-rich gas mixture. The atomic number considerations follow from the dominant photoelectric absorption cross section per atom going roughly as  $Z^n/E_x^3$ , where  $n$  varies between 4 and 5 over the region of interest, and the x-ray energy is  $E_x$ .<sup>\*</sup> To minimize self-absorption, materials such as polypropylene, Mylar, carbon, and (rarely) lithium in the form of foils, fibers or foams are used as radiators. The TR signal in the active regions is in most cases

---

<sup>\*</sup> Photon absorption coefficients for the elements (via a NIST link), and  $dE/dx|_{\text{min}}$  and plasma energies for many materials are given in [pdg.lbl.gov/AtomicNuclearProperties](http://pdg.lbl.gov/AtomicNuclearProperties).

superimposed upon the particle ionization losses, which are proportional to  $Z$ . In most of the detectors used in particle physics the radiator parameters are chosen to provide  $\gamma_{\text{sat}} \approx 2000$ . Those detectors normally work as threshold devices, ensuring the best electron/pion separation in the momentum range  $1 \text{ GeV}/c \lesssim p \lesssim 150 \text{ GeV}/c$ .

One can distinguish two design concepts—“thick” and “thin” detectors:

In “thick” detectors the radiator, optimized for a minimum total radiation length at maximum TR yield and total TR absorption in the detector, consists of few hundred foils (for instance 300  $20 \mu\text{m}$  thick polypropylene foils). Most of the TR photons are absorbed in the radiator itself. To maximise the number of TR photons reaching the detector, part of the radiator far from the active layers is often made of thicker foils, which shifts the x-ray spectrum to higher energies. The detector thickness, about 2-4 cm for Xe-filled gas chambers, is optimized to absorb the incoming x-ray spectrum. A classical detector is composed of several similar modules which respond nearly independently. Such detectors were used in the UA2, NA34 and other experiments [115], and are being used in the ALICE experiment [116], [117].

In another TRD concept a fine granular radiator/detector structure exploits the soft part of the TR spectrum more efficiently and thereby may act also as an integral part of the tracking detector providing many points of measurements on the particle track. This can be achieved, for instance, by distributing small-diameter straw-tube detectors uniformly or in thin layers throughout the radiator material. Even with a relatively thin radiator stack, radiation below 5 keV is mostly lost in the radiators themselves. However for photon energies above this value, the absorption is reduced and the radiation can be registered by several consecutive detector layers, thus creating a strong TR build-up effect. This approach allows to realise a TRD as an integral part of a tracking detector. Descriptions of detectors using this approach in both accelerator and space experiments can be found in [116,117]. For example, in the ATLAS TR tracker (TRT), charged particles cross about 35 effective straw tube layers embedded in the radiator material [116]. The effective thickness of the Xe gas per straw is about 2.2 mm and the average number of foils per straw is about 40 with an effective foil thickness of about  $18 \mu\text{m}$ .

Although the values mentioned above are typical for most of the plastic radiators used with Xe-based detectors, they vary significantly depending on the detector parameters: radiator material, thickness and spacing, the geometry and position of the sensitive chambers, *etc.* Thus careful simulations are usually needed to build a detector optimized for a particular application. For TRD simulations the codes are based on well understood TR emission formulas (see for instance Ref. 87 in Sec. 34.7). They give a reasonably good agreement of the TR energy spectra with data (see in [117] and [120]), both for the stand-alone simulation programs (see ATLAS TRT in [116]) and for GEANT4 based ones [118], [119]. However non of them include correct angular distribution of the TR photons.

The discrimination between electrons and pions can be based on the charge deposition measured in each detection module, on the number of clusters – energy depositions observed above an optimal threshold (usually it is 5–7 keV), or on more sophisticated methods such as analyzing the pulse shape as a function of time. The total energy

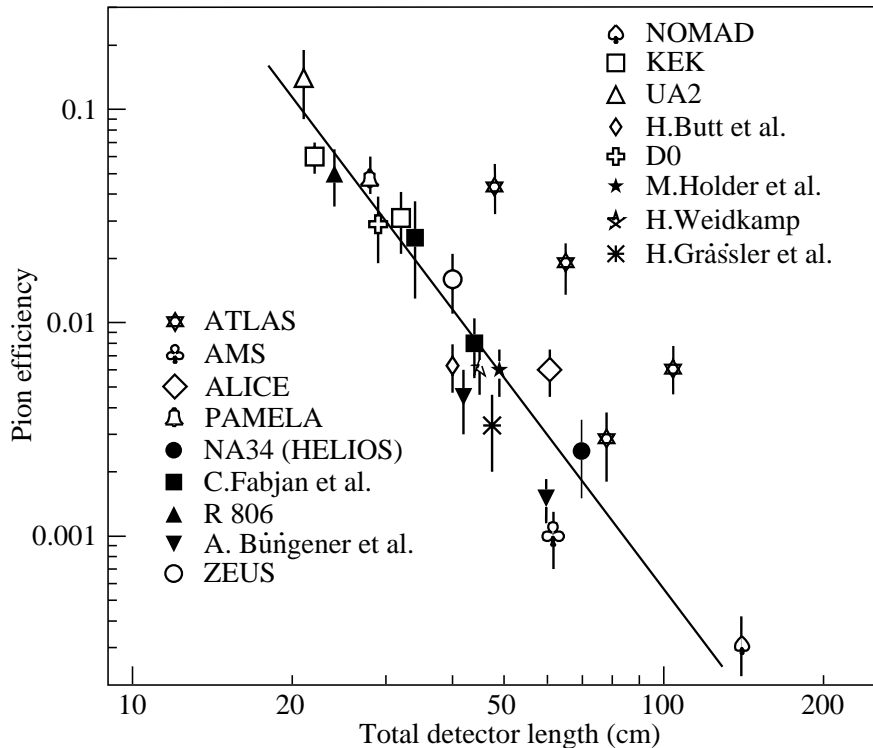


**Figure 35.16:** Pion efficiency measured (or predicted) for different TRDs as a function of the detector length for a fixed electron efficiency of 90%. The plot is taken from [115]. Results from more recent detectors are added from [116] and [117].

measurement technique is more suitable for thick gas volumes, which absorb most of the TR radiation and where the ionization loss fluctuations are relatively small. The cluster-counting method works better for detectors with thin gas layers, where the fluctuations of the ionization losses are bigger. Cluster-counting replaces the Landau-Vavilov distribution of background ionization energy losses with the Poisson statistics of  $\delta$ -electrons, responsible for the distribution tails. The latter distribution is narrower than the Landau-Vavilov distribution. In practice, most of the experiments use a likelihood method, which exploits detailed knowledge of the detector response for different particles and gives the best separation. The more parameters that are considered, the better separation power may be achieved. For example, for the TRD in the AMS experiment the rejection power achieved in the real experiment is better by almost one order of magnitude than that obtained in the beam test if stringent criteria for track selection are applied, see in [117]. Another example is the neural network method used by the ALICE TRD (ALICE point in Fig. 35.16) which gives another factor of 2–3 in rejection power with respect to the likelihood method [121].

The major factor in the performance of any TRD is its overall length. This is illustrated in Fig. 35.16, which shows, for a variety of detectors, the pion efficiency at a fixed electron efficiency of 90% as a function of the overall detector length. As TRD performance depends on particle energy, the experimental data in this figure covering

a range of particle energies from 1 GeV to 40 GeV, are rescaled to an energy of 10 GeV when possible. Phenomenologically, the rejection power against pions increases as  $5 \cdot 10^{L/38}$ , where the range of validity is  $L \approx 20\text{--}100$  cm. Apart from the beam energy variations, the observed scattering of the points in the plot reflects how effectively the detector space is used and how well the exact response to different particles is taken into account in the analysis. For instance, the ATLAS TRT was built as a compromise between TR and tracking requirements; that is why the test-beam prototype result (lower point) is better than the real TRT performance at the LHC shown in Fig. 35.16 for different regions in the detector (in agreement with MC).

In most cases, recent TRDs combine particle identification with charged-track measurement in the same detector [116,117,122]. This is particularly important for collider experiments, where the available space for the inner detector is very limited. For a modest increase of the radiation length due to the radiator ( $\sim 4\%$  X0), a significant enhancement of the electron identification was obtained in the case of the ATLAS TRT. Here, the combination of the two detector functions provides a powerful tool for electron identification even at very high particle densities.

In addition to the enhancement of the electron identification during offline data analysis, TRD signatures are often used in the trigger algorithms at collider experiments. The ALICE experiment [117] is a good example for the use of the TRD in a First Level Trigger. In the ATLAS experiment, the TRT information is used in the High Level Trigger (HLT) algorithms. At increasing luminosities, the electron trigger output rate becomes so high, that a significant increase of the calorimeter energy threshold is required to keep it at an acceptable level. This may affect the trigger efficiency of very important physics channels (e.g.  $W \rightarrow e\nu$  inclusive decay). Even a very soft TR cut at the HLT level, which preserves high electron efficiency (98%), allows to suppress a significant part of fake triggers and enhance the purity for physics events with electrons in a final state. The TRT also plays a crucial role in the studies where an electron suppression is required (e.g. hadronic mode of  $\tau$ -decays). TR information is a completely independent tool for electron identification and allows to study systematic uncertainties of other electron reconstruction methods.

Electron identification is not the only TRD application. Recent TRDs for particle astrophysics are designed to directly measure the Lorentz factor of high-energy nuclei by using the quadratic dependence of the TR yield on nuclear charge; see, for instance, in [116]. The radiator configuration ( $\ell_1, \ell_2$ ) is tuned to extend the TR yield rise up to  $\gamma \approx 10^5$  using the more energetic part of the TR spectrum (up to 100 keV). High density radiator materials (such as Al) are the best for this purpose. Direct absorption of the TR-photons of these energies with thin detectors becomes problematic and TR detection methods based on Compton scattering have been proposed, see in [116], [117].

The high granularity of the Si-pixel or the Si-microstrip detectors provides spatial separation of the TR photons and  $dE/dx$  losses at relatively modest distances between radiator and detector. These detectors may be the basis for novel devices which combine precise tracking and PID properties. TR measurements using a pixel detector with  $20 \mu\text{m}$  pitch size are described in [117]. The presence of a magnetic field could enhance the separation between TR photons and  $dE/dx$  losses. Simulations made on the basis of

the beam-test results has shown that in a magnetic field of 2 T and for the geometry of the ATLAS Si-tracker proposed for sLHC, a rejection factor of  $> 30$  can be obtained for an electron efficiency above 90% in the particle momentum range from 2 to 30 GeV/c, see in [116] and [117]. New detector techniques for TRDs are also under development. In particular, GasPixel detectors allow to obtain a space point accuracy of  $< 30 \mu\text{m}$  and exploit all details of the particle tracks to highlight individual TR clusters in the gas, see in [117]. Thin films of heavy scintillators might be a very attractive option for non-gas based TRD [117].

**35.6.7. Resistive-plate chambers :** Revised August 2017 by G. Aielli (U. Roma Tor Vergata).

The resistive-plate chamber (RPC) is a gaseous detector developed by R. Santonico and R. Cardarelli in the early 1980's [123] \*. Although its original purpose was to provide a competitive alternative to large scintillator counters, the RPC's potential for timing tracker systems was quickly recognized given its excellent temporal and spatial resolutions and the ease of constructing large-format single detectors. The RPC, as sketched in Fig. 35.17, is a large planar capacitor with two parallel high bulk resistivity electrode plates ( $10^9$ – $10^{13} \Omega\cdot\text{cm}$ ) separated by a set of insulating spacers. The spacers define a gap in the range from a few millimeters down to 0.1 mm with a precision of a few  $\sim \mu\text{m}$ . The gap is filled with a suitable atmospheric-pressure gas mixture which serves as a target for ionizing radiation. Primary ionization for sub-millimeter gas gaps can be insufficient, thus multiple gaps can be combined to ensure an acceptable detection efficiency [125].

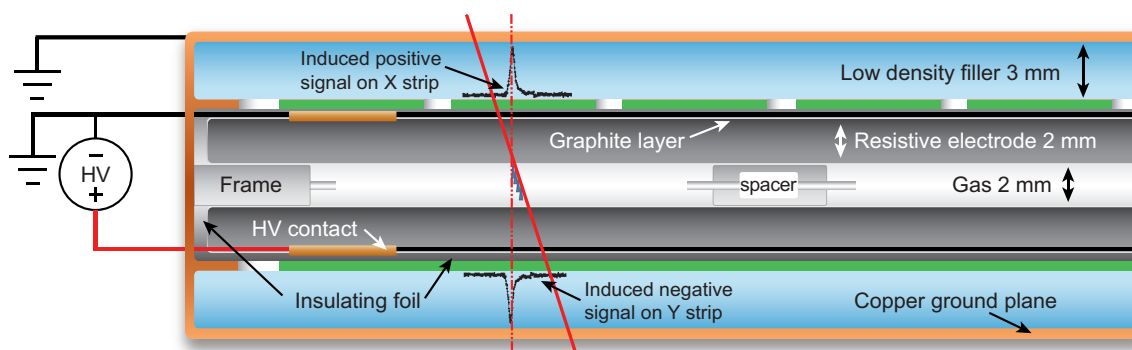


**Figure 35.17:** Schematic cross section of a generic single gap RPC.

The electrodes are most commonly made of high pressure phenolic-melaminic laminate (HPL), improperly referred to as "bakelite", or glass. A moderate electrode resistivity ( $\sim 10^5 \Omega/\square$ ) establishes a uniform electric field of several kV/mm across the gap, which initiates an electron avalanche following primary ionization. The above resistivity is low enough to ensure uniformity of the electric field, yet still transparent to fast signal transients from avalanches. This field configuration allows an excellent space-time localization of the signal. Due to the high electrode resistivity in RPCs, the electrode

\* The RPC was based on earlier work on a spark counter with one metallic and one high-resistivity plate [124].

time constant is much longer than discharge processes. Therefore only the locally-stored electrostatic energy contributes to the discharge, which prevents the formation of sparks and leaves the rest of the detector field unaffected. The gas-facing surface of HPL electrodes are commonly coated with a few  $\mu\text{m}$ -thick layer of polymerized linseed oil. This layer has a similar resistivity as the electrode, and is smooth to aid the uniformity of the electric field. It also protects the electrode from the free radicals generated in the discharge e.g. in presence of hydrocarbons or fluorocarbons. As with other gaseous detectors, the gas mixture is optimized for each specific application. In general it needs to contain a component to quench UV photons, thus avoiding discharge propagation. An electronegative component controls the avalanche growth in case of very high electric fields [126,127]. To first order, each primary ionization in an RPC is exponentially amplified according to its distance from the anode. Therefore RPC signals span a large dynamic range, unlike gaseous detectors where ionization and amplification occur in separate regions (e.g. wire chambers or MPGDs). For increasingly stronger fields, the avalanche exponential growth progressively saturates to linear [128], and finally reaches a strongly-saturated "streamer" transition which exhausts all the locally-available energy [129]. A set of metallic readout electrodes (e.g. pads or strips) placed behind the resistive electrodes detect the charge pulse induced by the fast movement of the avalanche electrons. The signal is isotropically distributed with respect to the field direction and present with equal but opposite amplitude on the two electrodes. This feature allows for 2D localization of the signal with uniform spatial resolution. The induced charge density projected in 1D can be calculated for a simplified RPC model [130] as:  $\sigma(x) = A/\cosh[(x - \bar{x})/\delta]$  where  $\bar{x}$  is the center of the avalanche and  $\delta = (g + 2d)/\pi$  depends on the gap and electrode width ( $g$  and  $d$ , respectively). The spatial extent of actual signals are generally larger than those given by this model [131,132]. Conductivity of the graphite layer results in the most prominent broadening. Cross-talk from parasitic coupling of neighboring electrodes can also spread the signal spatially. Although the broadened charge distribution preserves most of the original spatial resolution, it can adversely impact signal clustering, so the detector layout must be calculated according to the expected application. Sensitivity to high-frequency electron avalanche signals over large RPC areas requires a correspondingly adequate Faraday cage and readout structure design. In particular, the front end electronics must be time-sensitive with a fast response and low noise, although these requirements are usually in competition [133].

**35.6.7.1. RPC types and applications:** RPCs are generally classified in two categories depending on the gas gap structure: single gap RPCs (described above) and multiple gap RPCs (typically referred as mRPCs or timing RPCs). While they are both based on the same principle they have different construction techniques, performance and limitations, making them suitable for different applications. Due to its simplicity and robustness, the single gap RPC is ideal for covering very large surfaces. Typical detector systems can have sensitive surface areas up to  $\sim 10^4 \text{ m}^2$ , with single module areas of a few  $\text{m}^2$ , and a space-time resolution down to  $\sim 0.4 \text{ ns} \times 100 \mu\text{m}$  [134,135]. Typical applications are in muon systems (e.g. the muon trigger systems of the LHC experiments) or ground and underground based cosmic rays and neutrino arrays [136]. Moreover, single gap RPCs have recently found an application in tracking calorimetry [137]. The mRPC

allows for smaller gas gap thicknesses while still maintaining a sufficient gaseous target. The most common version [138] consists of a stack of floating glass electrodes separated by monofilament (i.e. fishing line), sandwiched between two external electrodes which provide the high-voltage bias. The floating glass electrodes assume a potential determined by the avalanche processes occurring between them. mRPCs have been largely used in TOF systems and in applications such as timing PET.

**35.6.7.2. Time and space resolution:** The RPC field configuration generates an avalanche which is strongly correlated in space and time to the original ionizing event. Space-time uncertainties generally arise from the statistical fluctuations of the ionization and multiplication processes, and from the characteristics of the readout and front-end electronics. The intrinsic signal latency is commonly in the ns range, making the RPC suitable for applications where a low latency is essential. A higher time resolution and shorter signal duration is correlated with a thinner gas gap, although a higher electric field is required for sufficient avalanche development [138,139]. Typical timing performances are from around 1 ns with a 2 mm gas gap, down to 20 ps for a stack of several 0.1 mm gaps [140]. The mechanical delicacy of sub-mm-gap structures makes this technique less suitable for large detector areas. Digital strip readouts are commonly used, with spatial resolution determined by the strip pitch and the cluster size ( $\sim 0.5$  cm). Recent developments toward higher spatial resolutions are mostly based on charge centroid techniques, benefiting from the availability of low-cost high-performance readout electronics. The present state of the art detectors have a combined space-time resolution of  $\sim 50$  ps  $\times$  40  $\mu$ m [141].

**35.6.7.3. Rate capability and ageing:** RPC rate capability is limited by the voltage drop on resistive electrodes,  $\Delta V = V_a - V_{\text{gas}} = I \cdot R$  [142]. Here  $V_a$  is the applied voltage,  $V_{\text{gas}}$  is the effective voltage on the gas,  $R = \rho \cdot d/S$  is the total electrode resistance and  $I$  is the working current. Expressing  $I$  as the particle flux  $\Phi$  times an average charge per avalanche  $\langle Q \rangle$  gives  $\Delta V/\Phi = \rho \cdot d \cdot \langle Q \rangle$ . A large  $I$  not only limits the rate capability but also affects the long term performance of the detector. Discharges deplete the conductive properties of HPL electrodes [143]. In the presence of fluorocarbons and water, discharges generate hydrofluoric acid (HF) which damages internal detector surfaces, particularly glass electrodes [144]. HF damage can be mitigated by preventing water vapor contamination (for glass electrodes) or by sufficient flushing of the gas gap (for HPL electrodes). Operating in the streamer regime puts low requirements on the front end electronics sensitivity, but generally limits the counting rate capability to  $\sim 100$  Hz/cm<sup>2</sup> and requires stability over a large gain range. Higher-rate operation can be achieved by reducing gas gain in favor of electronic amplification, operating the detector in avalanche mode. Increasing concentrations of electronegative gases, such as C<sub>2</sub>H<sub>2</sub>F<sub>4</sub> and SF<sub>6</sub> [127], shifts the streamer transition to higher gains. The avalanche signal has a higher dynamic range, a drawback which can be compensated with appropriate electronics. With these techniques, stable performance at high rates (e.g. 10 kHz/cm<sup>2</sup>) has been achieved for large area single gap RPCs [133]. Additional techniques rely on the natural redundancy and small gain of multiple gap structures [145] and electrodes made with lower resistivity materials [146].

### 35.7. Semiconductor detectors

Updated November 2013 by H. Spieler.

Semiconductor detectors provide a unique combination of energy and position resolution. In collider detectors they are most widely used as position sensing devices and photodetectors (Sec. 35.2). Integrated circuit technology allows the formation of high-density micron-scale electrodes on large (15–20 cm diameter) wafers, providing excellent position resolution. Furthermore, the density of silicon and its small ionization energy yield adequate signals with active layers only 100–300  $\mu\text{m}$  thick, so the signals are also fast (typically tens of ns). The high energy resolution is a key parameter in x-ray, gamma, and charged particle spectroscopy, *e.g.*, in neutrinoless double beta decay searches. Silicon and germanium are the most commonly used materials, but gallium-arsenide, CdTe, CdZnTe, and other materials are also useful. CdZnTe provides a higher stopping power and the ratio of Cd to Zn concentrations changes the bandgap. Ge detectors are commonly operated at liquid nitrogen temperature to reduce the bias current, which depends exponentially on temperature. Semiconductor detectors depend crucially on low-noise electronics (see Sec. 35.8), so the detection sensitivity is determined by signal charge and capacitance. For a comprehensive discussion of semiconductor detectors and electronics see Ref. 147 or the tutorial website <http://www-physics.lbl.gov/spieler>.

#### 35.7.1. Materials Requirements :

Semiconductor detectors are essentially solid state ionization chambers. Absorbed energy forms electron-hole pairs, *i.e.*, negative and positive charge carriers, which under an applied electric field move towards their respective collection electrodes, where they induce a signal current. The energy required to form an electron-hole pair is proportional to the bandgap. In tracking detectors the energy loss in the detector should be minimal, whereas for energy spectroscopy the stopping power should be maximized, so for gamma rays high- $Z$  materials are desirable.

Measurements on silicon photodiodes [148] show that for photon energies below 4 eV one electron-hole ( $e-h$ ) pair is formed per incident photon. The mean energy  $E_i$  required to produce an  $e-h$  pair peaks at 4.4 eV for a photon energy around 6 eV. Above  $\sim 1.5$  keV it assumes a constant value, 3.67 eV at room temperature. It is larger than the bandgap energy because momentum conservation requires excitation of lattice vibrations (phonons). For minimum-ionizing particles, the most probable charge deposition in a 300  $\mu\text{m}$  thick silicon detector is about 3.5 fC (22000 electrons). Other typical ionization energies are 2.96 eV in Ge, 4.2 eV in GaAs, and 4.43 eV in CdTe.

Since both electronic and lattice excitations are involved, the variance in the number of charge carriers  $N = E/E_i$  produced by an absorbed energy  $E$  is reduced by the Fano factor  $F$  (about 0.1 in Si and Ge). Thus,  $\sigma_N = \sqrt{FN}$  and the energy resolution  $\sigma_E/E = \sqrt{FE_i/E}$ . However, the measured signal fluctuations are usually dominated by electronic noise or energy loss fluctuations in the detector. The electronic noise contributions depend on the pulse shaping in the signal processing electronics, so the choice of the shaping time is critical (see Sec. 35.8).

A smaller bandgap would produce a larger signal and improve energy resolution, but the intrinsic resistance of the material is critical. Thermal excitation, given by the Fermi-Dirac distribution, promotes electrons into the conduction band, so the thermally



excited carrier concentration increases exponentially with decreasing bandgaps. In pure Si the carrier concentration is  $\sim 10^{10} \text{cm}^{-3}$  at 300 K, corresponding to a resistivity  $\rho \approx 400 \text{k}\Omega \text{cm}$ . In reality, crystal imperfections and minute impurity concentrations limit Si carrier concentrations to  $\sim 10^{11} \text{cm}^{-3}$  at 300 K, corresponding to a resistivity  $\rho \approx 40 \text{k}\Omega \text{cm}$ . In practice, resistivities up to  $20 \text{k}\Omega \text{cm}$  are available, with mass production ranging from 5 to  $10 \text{k}\Omega \text{cm}$ . Signal currents at keV scale energies are of order  $\mu\text{A}$ . However, for a resistivity of  $10^4 \Omega\text{cm}$  a  $300 \mu\text{m}$  thick sensor with  $1 \text{cm}^2$  area would have a resistance of  $300 \Omega$ , so 30 V would lead to a current flow of 100 mA and a power dissipation of 3 W. On the other hand, high-quality single crystals of Si and Ge can be grown economically with suitably large volumes, so to mitigate the effect of resistivity one resorts to reverse-biased diode structures. Although this reduces the bias current relative to a resistive material, the thermally excited leakage current can still be excessive at room temperature, so Ge diodes are typically operated at liquid nitrogen temperature (77 K).

A major effort is to find high- $Z$  materials with a bandgap that is sufficiently high to allow room-temperature operation while still providing good energy resolution. Compound semiconductors, *e.g.*, CdZnTe, can allow this, but typically suffer from charge collection problems, characterized by the product  $\mu\tau$  of mobility and carrier lifetime. In Si and Ge  $\mu\tau > 1 \text{cm}^2 \text{V}^{-1}$  for both electrons and holes, whereas in compound semiconductors it is in the range  $10^{-3}$ – $10^{-8}$ . Since for holes  $\mu\tau$  is typically an order of magnitude smaller than for electrons, detector configurations where the electron contribution to the charge signal dominates—*e.g.*, strip or pixel structures—can provide better performance.

### 35.7.2. Detector Configurations :

A  $p$ - $n$  junction operated at reverse bias forms a sensitive region depleted of mobile charge and sets up an electric field that sweeps charge liberated by radiation to the electrodes. Detectors typically use an asymmetric structure, *e.g.*, a highly doped  $p$  electrode and a lightly doped  $n$  region, so that the depletion region extends predominantly into the lightly doped volume.

In a planar device the thickness of the depleted region is

$$W = \sqrt{2\epsilon(V + V_{bi})/Ne} = \sqrt{2\rho\mu\epsilon(V + V_{bi})}, \quad (35.19)$$

where  $V$  = external bias voltage

$V_{bi}$  = “built-in” voltage ( $\approx 0.5 \text{ V}$  for resistivities typically used in Si detectors)

$N$  = doping concentration

$e$  = electronic charge

$\epsilon$  = dielectric constant =  $11.9 \epsilon_0 \approx 1 \text{ pF/cm}$  in Si

$\rho$  = resistivity (typically 1–10  $\text{k}\Omega \text{cm}$  in Si)

$\mu$  = charge carrier mobility

=  $1350 \text{ cm}^2 \text{V}^{-1} \text{s}^{-1}$  for electrons in Si

=  $450 \text{ cm}^2 \text{V}^{-1} \text{s}^{-1}$  for holes in Si

In Si

$$W = 0.5 [\mu\text{m}/\sqrt{\Omega\text{-cm} \cdot \text{V}}] \times \sqrt{\rho(V + V_{bi})} \text{ for } n\text{-type Si, and}$$

$$W = 0.3 [\mu\text{m}/\sqrt{\Omega\text{-cm} \cdot \text{V}}] \times \sqrt{\rho(V + V_{bi})} \text{ for } p\text{-type Si.}$$

The conductive  $p$  and  $n$  regions together with the depleted volume form a capacitor with the capacitance per unit area

$$C = \epsilon/W \approx 1 \text{ [pF/cm]} / W \text{ in Si.} \quad (35.20)$$

In strip and pixel detectors the capacitance is dominated by the fringing capacitance to neighboring electrodes. For example, the strip-to-strip Si fringing capacitance is  $\sim 1\text{--}1.5 \text{ pF cm}^{-1}$  of strip length at a strip pitch of  $25\text{--}50 \text{ }\mu\text{m}$ .

Large volume ( $\sim 10^2\text{--}10^3 \text{ cm}^3$ ) Ge detectors are commonly configured as coaxial detectors, *e.g.*, a cylindrical  $n$ -type crystal with  $5\text{--}10 \text{ cm}$  diameter and  $10 \text{ cm}$  length with an inner  $5\text{--}10 \text{ mm}$  diameter  $n^+$  electrode and an outer  $p^+$  layer forming the diode junction. Ge can be grown with very low impurity levels,  $10^9\text{--}10^{10} \text{ cm}^{-3}$  (HPGe), so these large volumes can be depleted with several kV.

### 35.7.3. Signal Formation :

The signal pulse shape depends on the instantaneous carrier velocity  $v(x) = \mu E(x)$  and the electrode geometry, which determines the distribution of induced charge (*e.g.*, see Ref. 147, pp. 71–83). Charge collection time decreases with increasing bias voltage, and can be reduced further by operating the detector with “overbias,” *i.e.*, a bias voltage exceeding the value required to fully deplete the device. Note that in partial depletion the electric field goes to zero, whereas going beyond full depletion adds a constantly distributed field. The collection time is limited by velocity saturation at high fields (in Si approaching  $10^7 \text{ cm/s}$  at  $E > 10^4 \text{ V/cm}$ ); at an average field of  $10^4 \text{ V/cm}$  the collection time is about  $15 \text{ ps}/\mu\text{m}$  for electrons and  $30 \text{ ps}/\mu\text{m}$  for holes. In typical fully-depleted detectors  $300 \text{ }\mu\text{m}$  thick, electrons are collected within about  $10 \text{ ns}$ , and holes within about  $25 \text{ ns}$ .

Position resolution is limited by transverse diffusion during charge collection (typically  $5 \text{ }\mu\text{m}$  for  $300 \text{ }\mu\text{m}$  thickness) and by knock-on electrons. Resolutions of  $2\text{--}4 \text{ }\mu\text{m}$  (rms) have been obtained in beam tests. In magnetic fields, the Lorentz drift deflects the electron and hole trajectories and the detector must be tilted to reduce spatial spreading (see “Hall effect” in semiconductor textbooks).

Electrodes can be in the form of cm-scale pads, strips, or  $\mu\text{m}$ -scale pixels. Various readout structures have been developed for pixels, *e.g.*, CCDs, DEPFETs, monolithic pixel devices that integrate sensor and electronics (MAPS), and hybrid pixel devices that utilize separate sensors and readout ICs connected by two-dimensional arrays of solder bumps. For an overview and further discussion see Ref. 147.

In gamma ray spectroscopy ( $E_\gamma > 10^2 \text{ keV}$ ) Compton scattering dominates, so for a significant fraction of events the incident gamma energy is not completely absorbed, *i.e.*, the Compton scattered photon escapes from the detector and the energy deposited by the Compton electron is only a fraction of the total. Distinguishing multi-interaction events, *e.g.*, multiple Compton scatters with a final photoelectric absorption, from single Compton scatters allows background suppression. Since the individual interactions take place in different parts of the detector volume, these events can be distinguished by segmenting the outer electrode of a coaxial detector and analyzing the current pulse shapes. The different collection times can be made more distinguishable by using “point” electrodes, where most of the signal is induced when charges are close to the electrode,

similarly to strip or pixel detectors. Charge clusters arriving from different positions in the detector will arrive at different times and produce current pulses whose major components are separated in time. Point electrodes also reduce the electrode capacitance, which reduces electronic noise, but careful design is necessary to avoid low-field regions in the detector volume.

**35.7.4. Radiation Damage :** Radiation damage occurs through two basic mechanisms:

1. Bulk damage due to displacement of atoms from their lattice sites. This leads to increased leakage current, carrier trapping, and build-up of space charge that changes the required operating voltage. Displacement damage depends on the nonionizing energy loss and the energy imparted to the recoil atoms, which can initiate a chain of subsequent displacements, *i.e.*, damage clusters. Hence, it is critical to consider both particle type and energy.
2. Surface damage due to charge build-up in surface layers, which leads to increased surface leakage currents. In strip detectors the inter-strip isolation is affected. The effects of charge build-up are strongly dependent on the device structure and on fabrication details. Since the damage is proportional to the absorbed energy (when ionization dominates), the dose can be specified in rad (or Gray) independent of particle type.

The increase in reverse bias current due to bulk damage is  $\Delta I_r = \alpha \Phi$  per unit volume, where  $\Phi$  is the particle fluence and  $\alpha$  the damage coefficient ( $\alpha \approx 3 \times 10^{-17}$  A/cm for minimum ionizing protons and pions after long-term annealing;  $\alpha \approx 2 \times 10^{-17}$  A/cm for 1 MeV neutrons). The reverse bias current depends strongly on temperature

$$\frac{I_R(T_2)}{I_R(T_1)} = \left(\frac{T_2}{T_1}\right)^2 \exp\left[-\frac{E}{2k} \left(\frac{T_1 - T_2}{T_1 T_2}\right)\right], \quad (35.21)$$

where  $E = 1.2$  eV, so rather modest cooling can reduce the current substantially ( $\sim 6$ -fold current reduction in cooling from room temperature to  $0^\circ\text{C}$ ).

Displacement damage forms acceptor-like states. These trap electrons, building up a negative space charge, which in turn requires an increase in the applied voltage to sweep signal charge through the detector thickness. This has the same effect as a change in resistivity, *i.e.*, the required voltage drops initially with fluence, until the positive and negative space charge balance and very little voltage is required to collect all signal charge. At larger fluences the negative space charge dominates, and the required operating voltage increases ( $V \propto N$ ). The safe limit on operating voltage ultimately limits the detector lifetime. Strip detectors specifically designed for high voltages have been extensively operated at bias voltages  $>500$  V. Since the effect of radiation damage depends on the electronic activity of defects, various techniques have been applied to neutralize the damage sites. For example, additional doping with oxygen can increase the allowable charged hadron fluence roughly three-fold [149]. Detectors with columnar electrodes normal to the surface can also extend operational lifetime [150]. The increase in leakage current with fluence, on the other hand, appears to be unaffected by resistivity and whether the material is *n* or *p*-type. At fluences beyond  $10^{15}$   $\text{cm}^{-2}$  decreased carrier lifetime becomes critical [151,152].

Strip and pixel detectors have remained functional at fluences beyond  $10^{15}$  cm<sup>-2</sup> for minimum ionizing protons. At this damage level, charge loss due to recombination and trapping becomes significant and the high signal-to-noise ratio obtainable with low-capacitance pixel structures extends detector lifetime. The higher mobility of electrons makes them less sensitive to carrier lifetime than holes, so detector configurations that emphasize the electron contribution to the charge signal are advantageous, *e.g.*, n<sup>+</sup> strips or pixels on a p- or n-substrate. The occupancy of the defect charge states is strongly temperature dependent; competing processes can increase or decrease the required operating voltage. It is critical to choose the operating temperature judiciously ( $-10$  to  $0^\circ\text{C}$  in typical collider detectors) and limit warm-up periods during maintenance. For a more detailed summary see Ref. 153 and the web-sites of the ROSE and RD50 collaborations at <http://RD48.web.cern.ch/rd48> and <http://RD50.web.cern.ch/rd50>. Materials engineering, *e.g.*, introducing oxygen interstitials, can improve certain aspects and is under investigation. At high fluences diamond is an alternative, but operates as an insulator rather than a reverse-biased diode.

Currently, the lifetime of detector systems is still limited by the detectors; in the electronics use of standard “deep submicron” CMOS fabrication processes with appropriately designed circuitry has increased the radiation resistance to fluences  $> 10^{15}$  cm<sup>-2</sup> of minimum ionizing protons or pions. For a comprehensive discussion of radiation effects see Ref. 154.

### 35.8. Low-noise electronics

Revised November 2013 by H. Spieler.

Many detectors rely critically on low-noise electronics, either to improve energy resolution or to allow a low detection threshold. A typical detector front-end is shown in Fig. 35.18.

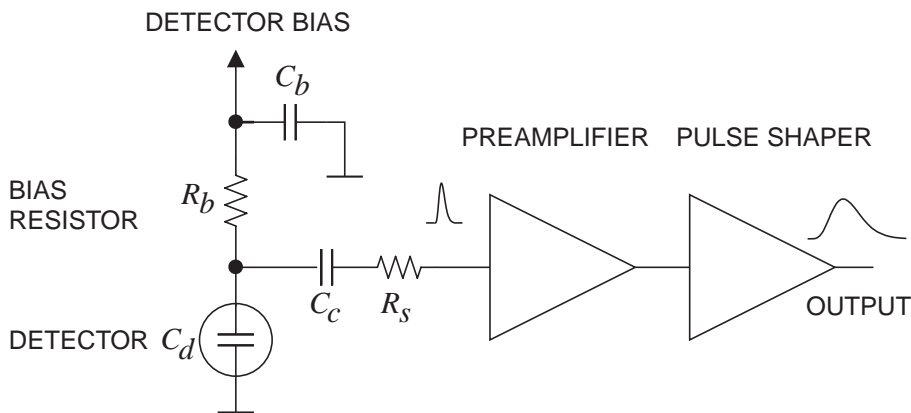


**Figure 35.18:** Typical detector front-end circuit.

The detector is represented by a capacitance  $C_d$ , a relevant model for most detectors. Bias voltage is applied through resistor  $R_b$  and the signal is coupled to the preamplifier through a blocking capacitor  $C_c$ . The series resistance  $R_s$  represents the sum of all resistances present in the input signal path, *e.g.* the electrode resistance, any input

protection networks, and parasitic resistances in the input transistor. The preamplifier provides gain and feeds a pulse shaper, which tailors the overall frequency response to optimize signal-to-noise ratio while limiting the duration of the signal pulse to accommodate the signal pulse rate. Even if not explicitly stated, all amplifiers provide some form of pulse shaping due to their limited frequency response.

The equivalent circuit for the noise analysis (Fig. 35.19) includes both current and voltage noise sources. The leakage current of a semiconductor detector, for example, fluctuates due to continuous electron emission statistics. The statistical fluctuations in the charge measurement will scale with the square root of the total number of recorded charges, so this noise contribution increases with the width of the shaped output pulse. This “shot noise”  $i_{nd}$  is represented by a current noise generator in parallel with the detector. Resistors exhibit noise due to thermal velocity fluctuations of the charge carriers. This yields a constant noise power density vs. frequency, so increasing the bandwidth of the shaped output pulse, *i.e.* reducing the shaping time, will increase the noise. This noise source can be modeled either as a voltage or current generator. Generally, resistors shunting the input act as noise current sources and resistors in series with the input act as noise voltage sources (which is why some in the detector community refer to current and voltage noise as “parallel” and “series” noise). Since the bias resistor effectively shunts the input, as the capacitor  $C_b$  passes current fluctuations to ground, it acts as a current generator  $i_{nb}$  and its noise current has the same effect as the shot noise current from the detector. Any other shunt resistances can be incorporated in the same way. Conversely, the series resistor  $R_s$  acts as a voltage generator. The electronic noise of the amplifier is described fully by a combination of voltage and current sources at its input, shown as  $e_{na}$  and  $i_{na}$ .

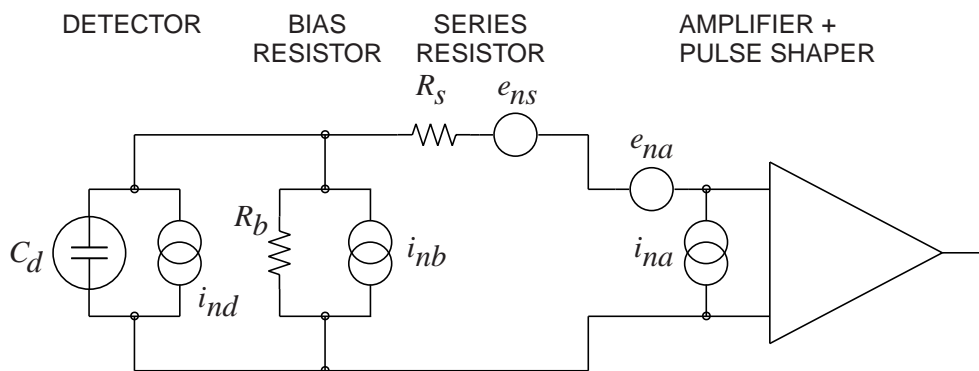


Figure 35.19: Equivalent circuit for noise analysis.

Shot noise and thermal noise have a “white” frequency distribution, *i.e.* the spectral power densities  $dP_n/df \propto di_n^2/df \propto de_n^2/df$  are constant with the magnitudes

$$\begin{aligned}
 i_{nd}^2 &= 2eI_d , \\
 i_{nb}^2 &= \frac{4kT}{R_b} , \\
 e_{ns}^2 &= 4kTR_s ,
 \end{aligned}
 \tag{35.22}$$

where  $e$  is the electronic charge,  $I_d$  the detector bias current,  $k$  the Boltzmann constant and  $T$  the temperature. Typical amplifier noise parameters  $e_{na}$  and  $i_{na}$  are of order  $\text{nV}/\sqrt{\text{Hz}}$  and  $\text{pA}/\sqrt{\text{Hz}}$ . Trapping and detrapping processes in resistors, dielectrics and semiconductors can introduce additional fluctuations whose noise power frequently exhibits a  $1/f$  spectrum. The spectral density of the  $1/f$  noise voltage is

$$e_{nf}^2 = \frac{A_f}{f}, \quad (35.23)$$

where the noise coefficient  $A_f$  is device specific and of order  $10^{-10}$ – $10^{-12} \text{V}^2$ .

A fraction of the noise current flows through the detector capacitance, resulting in a frequency-dependent noise voltage  $i_n/(\omega C_d)$ , which is added to the noise voltage in the input circuit. Thus, the current noise contribution increases with lowering frequency, so its contribution increases with shaping pulse width. Since the individual noise contributions are random and uncorrelated, they add in quadrature. The total noise at the output of the pulse shaper is obtained by integrating over the full bandwidth of the system. Superimposed on repetitive detector signal pulses of constant magnitude, purely random noise produces a Gaussian signal distribution.

Since radiation detectors typically convert the deposited energy into charge, the system's noise level is conveniently expressed as an equivalent noise charge  $Q_n$ , which is equal to the detector signal that yields a signal-to-noise ratio of one. The equivalent noise charge is commonly expressed in Coulombs, the corresponding number of electrons, or the equivalent deposited energy (eV). For a capacitive sensor

$$Q_n^2 = i_n^2 F_i T_s + e_n^2 F_v \frac{C^2}{T_s} + F_{vf} A_f C^2, \quad (35.24)$$

where  $C$  is the sum of all capacitances shunting the input,  $F_i$ ,  $F_v$ , and  $F_{vf}$  depend on the shape of the pulse determined by the shaper and  $T_s$  is a characteristic time, for example, the peaking time of a semi-gaussian pulse or the sampling interval in a correlated double sampler. The form factors  $F_i$ ,  $F_v$  are easily calculated

$$F_i = \frac{1}{2T_s} \int_{-\infty}^{\infty} [W(t)]^2 dt, \quad F_v = \frac{T_s}{2} \int_{-\infty}^{\infty} \left[ \frac{dW(t)}{dt} \right]^2 dt, \quad (35.25)$$

where for time-invariant pulse-shaping  $W(t)$  is simply the system's impulse response (the output signal seen on an oscilloscope) for a short input pulse with the peak output signal normalized to unity. For more details see Refs. 155 and 156.

A pulse shaper formed by a single differentiator and integrator with equal time constants has  $F_i = F_v = 0.9$  and  $F_{vf} = 4$ , independent of the shaping time constant. The overall noise bandwidth, however, depends on the time constant, *i.e.* the characteristic time  $T_s$ . The contribution from noise currents increases with shaping time, *i.e.*, pulse duration, whereas the voltage noise decreases with increasing shaping time, *i.e.* reduced bandwidth. Noise with a  $1/f$  spectrum depends only on the ratio of upper to lower cutoff frequencies (integrator to differentiator time constants), so for a given shaper topology

the  $1/f$  contribution to  $Q_n$  is independent of  $T_S$ . Furthermore, the contribution of noise voltage sources to  $Q_n$  increases with detector capacitance. Pulse shapers can be designed to reduce the effect of current noise, *e.g.*, mitigate radiation damage. Increasing pulse symmetry tends to decrease  $F_i$  and increase  $F_v$  (*e.g.*, to 0.45 and 1.0 for a shaper with one  $CR$  differentiator and four cascaded integrators). For the circuit shown in Fig. 35.19,

$$Q_n^2 = \left(2eI_d + 4kT/R_b + i_{na}^2\right)F_iT_S + (4kTR_s + e_{na}^2)F_vC_d^2/T_S + F_vfA_fC_d^2. \quad (35.26)$$

As the characteristic time  $T_S$  is changed, the total noise goes through a minimum, where the current and voltage contributions are equal. Fig. 35.20 shows a typical example. At short shaping times the voltage noise dominates, whereas at long shaping times the current noise takes over. The noise minimum is flattened by the presence of  $1/f$  noise. Increasing the detector capacitance will increase the voltage noise and shift the noise minimum to longer shaping times.

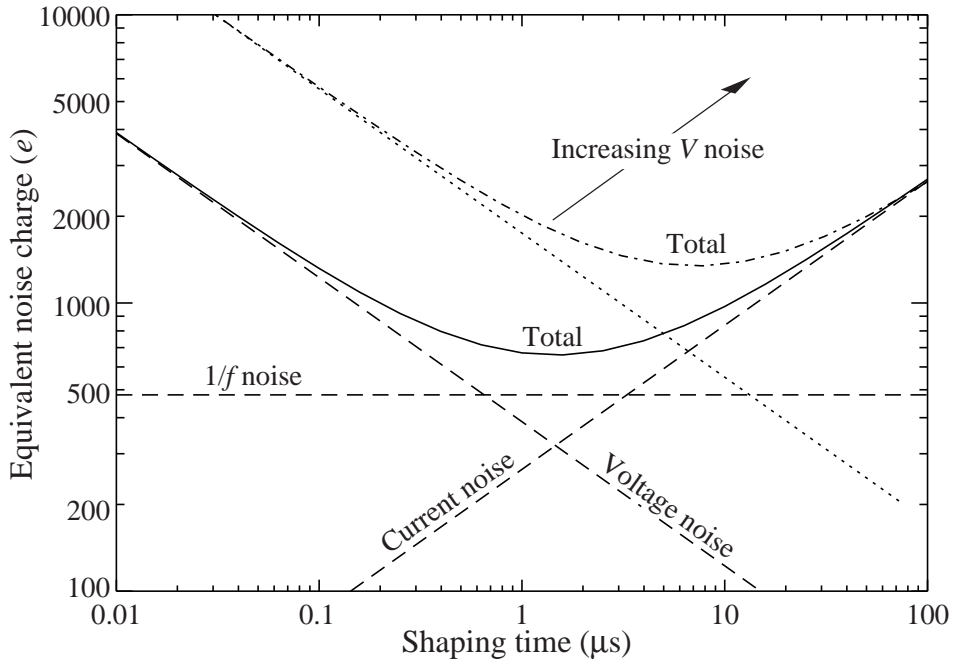


**Figure 35.20:** Equivalent noise charge *vs* shaping time. Changing the voltage or current noise contribution shifts the noise minimum. Increased voltage noise is shown as an example.

For quick estimates, one can use the following equation, which assumes an FET amplifier (negligible  $i_{na}$ ) and a simple  $CR$ - $RC$  shaper with time constants  $\tau$  (equal to the peaking time):

$$\begin{aligned} (Q_n/e)^2 = & 12 \left[ \frac{1}{\text{nA} \cdot \text{ns}} \right] I_d \tau + 6 \times 10^5 \left[ \frac{\text{k}\Omega}{\text{ns}} \right] \frac{\tau}{R_b} \\ & + 3.6 \times 10^4 \left[ \frac{\text{ns}}{(\text{pF})^2 (\text{nV})^2 / \text{Hz}} \right] e_n^2 \frac{C^2}{\tau}. \end{aligned} \quad (35.27)$$

Noise is improved by reducing the detector capacitance and leakage current, judiciously selecting all resistances in the input circuit, and choosing the optimum shaping time constant. Another noise contribution to consider is that noise cross-couples from the neighboring front-ends in strip and pixel detectors through the inter-electrode capacitance.

The noise parameters of the amplifier depend primarily on the input device. In field effect transistors, the noise current contribution is very small, so reducing the detector leakage current and increasing the bias resistance will allow long shaping times with correspondingly lower noise. In bipolar transistors, the base current sets a lower bound on the noise current, so these devices are best at short shaping times. In special cases where the noise of a transistor scales with geometry, *i.e.*, decreasing noise voltage with increasing input capacitance, the lowest noise is obtained when the input capacitance of the transistor is equal to the detector capacitance, albeit at the expense of power dissipation. Capacitive matching is useful with field-effect transistors, but not bipolar transistors. In bipolar transistors, the minimum obtainable noise is independent of shaping time, but only at the optimum collector current  $I_C$ , which does depend on shaping time.

$$Q_{n,\min}^2 = 4kT \frac{C}{\sqrt{\beta_{DC}}} \sqrt{F_i F_v} \quad \text{at} \quad I_c = \frac{kT}{e} C \sqrt{\beta_{DC}} \sqrt{\frac{F_v}{F_i} \frac{1}{T_S}}, \quad (35.28)$$

where  $\beta_{DC}$  is the DC current gain. For a  $CR$ - $RC$  shaper and  $\beta_{DC} = 100$ ,

$$Q_{n,\min}/e \approx 250 \sqrt{C/\text{pF}}. \quad (35.29)$$

Practical noise levels range from  $\sim 1e$  for CCD's at long shaping times to  $\sim 10^4 e$  in high-capacitance liquid argon calorimeters. Silicon strip detectors typically operate at  $\sim 10^3$  electrons, whereas pixel detectors with fast readout provide noise of several hundred electrons.

In timing measurements, the slope-to-noise ratio must be optimized, rather than the signal-to-noise ratio alone, so the rise time  $t_r$  of the pulse is important. The "jitter"  $\sigma_t$  of the timing distribution is

$$\sigma_t = \frac{\sigma_n}{(dS/dt)_{S_T}} \approx \frac{t_r}{S/N}, \quad (35.30)$$

where  $\sigma_n$  is the rms noise and the derivative of the signal  $dS/dt$  is evaluated at the trigger level  $S_T$ . To increase  $dS/dt$  without incurring excessive noise, the amplifier bandwidth should match the rise-time of the detector signal. The 10 to 90% rise time of an amplifier with bandwidth  $f_U$  is  $0.35/f_U$ . For example, an oscilloscope with 350 MHz bandwidth has a 1 ns rise time. When amplifiers are cascaded, which is invariably necessary, the individual rise times add in quadrature.

$$t_r \approx \sqrt{t_{r1}^2 + t_{r2}^2 + \dots + t_{rn}^2}. \quad (35.31)$$

Increasing signal-to-noise ratio also improves time resolution, so minimizing the total capacitance at the input is also important. At high signal-to-noise ratios, the time jitter can be much smaller than the rise time. The timing distribution may shift with



signal level (“walk”), but this can be corrected by various means, either in hardware or software [8].

The basic principles discussed above apply to both analog and digital signal processing. In digital signal processing the pulse shaper shown in Fig. 35.18 is replaced by an analog to digital converter (ADC) followed by a digital processor that determines the pulse shape. Digital signal processing allows great flexibility in implementing filtering functions. The software can be changed readily to adapt to a wide variety of operating conditions and it is possible to implement filters that are impractical or even impossible using analog circuitry. However, this comes at the expense of increased circuit complexity and increased demands on the ADC compared to analog shaping.

If the sampling rate of the ADC is too low, high frequency components will be transferred to lower frequencies (“aliasing”). The sampling rate of the ADC must be high enough to capture the maximum frequency component of the input signal. Apart from missing information on the fast components of the pulse, undersampling introduces spurious artifacts. If the frequency range of the input signal is much greater, the noise at the higher frequencies will be transferred to lower frequencies and increase the noise level in the frequency range of pulses formed in the subsequent digital shaper. The Nyquist criterion states that the sampling frequency must be at least twice the maximum relevant input frequency. This requires that the bandwidth of the circuitry preceding the ADC must be limited. The most reliable technique is to insert a low-pass filter.

The digitization process also introduces inherent noise, since the voltage range  $\Delta V$  corresponding to a minimum bit introduces quasi-random fluctuations relative to the exact amplitude

$$\sigma_n = \frac{\Delta V}{\sqrt{12}}. \quad (35.32)$$

When the Nyquist condition is fulfilled the noise bandwidth  $\Delta f_n$  is spread nearly uniformly and extends to  $1/2$  the sampling frequency  $f_S$ , so the spectral noise density

$$e_n = \frac{\sigma_n}{\sqrt{\Delta f_n}} = \frac{\Delta V}{\sqrt{12}} \cdot \frac{1}{\sqrt{f_S/2}} = \frac{\Delta V}{\sqrt{6}f_S}. \quad (35.33)$$

Sampling at a higher frequency spreads the total noise over a larger frequency range, so oversampling can be used to increase the effective resolution. In practice, this quantization noise is increased by differential nonlinearity. Furthermore, the equivalent input noise of ADCs is often rather high, so the overall gain of the stages preceding the ADC must be sufficiently large for the preamplifier input noise to override.

When implemented properly, digital signal processing provides significant advantages in systems where the shape of detector signal pulses changes greatly, for example in large semiconductor detectors for gamma rays or in gaseous detectors (*e.g.* TPCs) where the duration of the current pulse varies with drift time, which can range over orders of magnitude. Where is analog signal processing best (most efficient)? In systems that require fast time response the high power requirements of high-speed ADCs are prohibitive. Systems that are not sensitive to pulse shape can use fixed shaper constants and rather simple filters, which can be either continuous or sampled. In high density

systems that require small circuit area and low power (*e.g.* strip and pixel detectors), analog filtering often yields the required response and tends to be most efficient.

It is important to consider that additional noise is often introduced by external electronics, *e.g.* power supplies and digital systems. External noise can couple to the input. Often the “common grounding” allows additional noise current to couple to the current loop connecting the detector to the preamp. Recognizing additional noise sources and minimizing cross-coupling to the detector current loop is often important. Understanding basic physics and its practical effects is important in forming a broad view of the detector system and recognizing potential problems (*e.g.* modified data), rather than merely following standard recipes.

For a more detailed introduction to detector signal processing and electronics see Ref. 147 or the tutorial website <http://www-physics.lbl.gov/spieler>.

### 35.9. Calorimeters

A calorimeter is designed to measure a particle’s (or jet’s) energy and direction for an (ideally) contained electromagnetic (EM) or hadronic shower. The characteristic interaction distance for an electromagnetic interaction is the radiation length  $X_0$ , which ranges from  $13.8 \text{ g cm}^{-2}$  in iron to  $6.0 \text{ g cm}^{-2}$  in uranium.\* Similarly, the characteristic nuclear interaction length  $\lambda_I$  varies from  $132.1 \text{ g cm}^{-2}$  (Fe) to  $209 \text{ g cm}^{-2}$  (U).† In either case, a calorimeter must be many interaction lengths deep, where “many” is determined by physical size, cost, and other factors. EM calorimeters tend to be  $15\text{--}30 X_0$  deep, while hadronic calorimeters are usually compromised at  $5\text{--}8 \lambda_I$ . In real experiments there is likely to be an EM calorimeter in front of the hadronic section, which in turn has less sampling density in the back, so the hadronic cascade occurs in a succession of different structures.

In all cases there is a premium on small  $\lambda_I/\rho$  and  $X_0/\rho$  (both with units of length). These quantities are shown for  $Z > 20$  for the chemical elements in Fig. 35.21. For the hadronic case, metallic absorbers in the W–Au region are best, followed by U. The Ru–Pd region elements are rare and expensive. Lead is a bad choice. Given cost considerations, Fe and Cu might be appropriate choices. For EM calorimeters high  $Z$  is preferred, and lead is not a bad choice.

These considerations are for *sampling calorimeters* consisting of metallic absorber sandwiched or (threaded) with an active material which generates signal. The active medium may be a scintillator, an ionizing noble liquid, a gas chamber, a semiconductor, or a Cherenkov radiator. The average interaction length is thus greater than that of the absorber alone, sometimes substantially so.

There are also *homogeneous calorimeters*, in which the entire volume is sensitive, *i.e.*, contributes signal. Homogeneous calorimeters (so far usually electromagnetic) may be built with inorganic heavy (high density, high  $\langle Z \rangle$ ) scintillating crystals, or non-scintillating Cherenkov radiators such as lead glass and lead fluoride. Scintillation

---

\*  $X_0 = 120 \text{ g cm}^{-2} Z^{-2/3}$  to better than 5% for  $Z > 23$ .

†  $\lambda_I = 37.8 \text{ g cm}^{-2} A^{0.312}$  to within 0.8% for  $Z > 15$ .

See [pdg.lbl.gov/AtomicNuclearProperties](http://pdg.lbl.gov/AtomicNuclearProperties) for actual values.

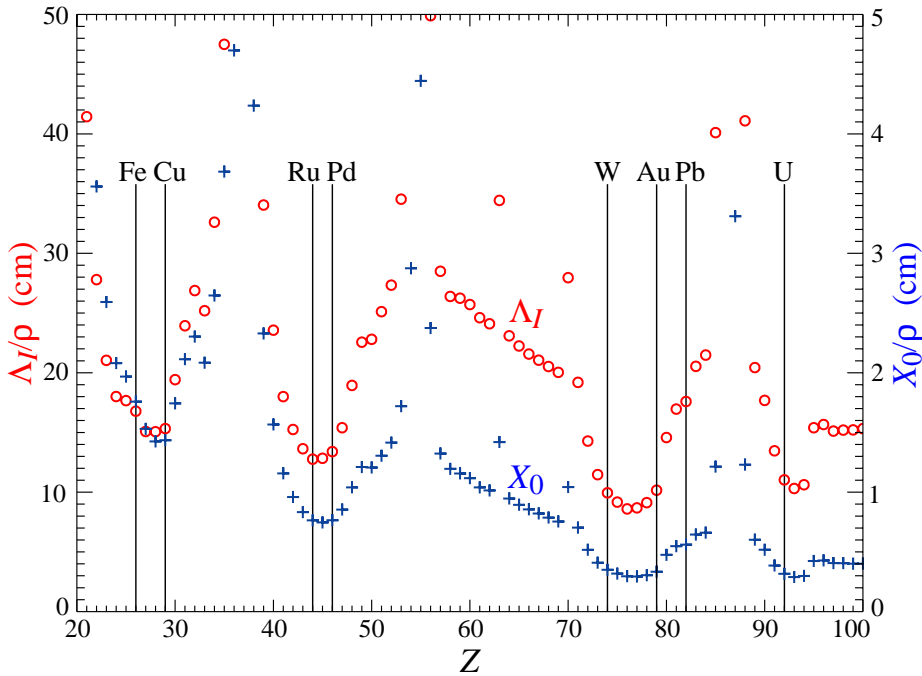


**Figure 35.21:** Nuclear interaction length  $\lambda_I/\rho$  (circles) and radiation length  $X_0/\rho$  (+’s) in cm for the chemical elements with  $Z > 20$  and  $\lambda_I < 50$  cm.

light and/or ionization in noble liquids can be detected. Nuclear interaction lengths in inorganic crystals range from 17.8 cm ( $\text{LuAlO}_3$ ) to 42.2 cm ( $\text{NaI}$ ). Popular choices have been  $\text{BGO}$  with  $\lambda_I = 22.3$  cm and  $X_0 = 1.12$  cm, and  $\text{PbWO}_4$  (20.3 cm and 0.89 cm). Properties of these and other commonly used inorganic crystal scintillators can be found in Table 35.4.

### 35.9.1. *Electromagnetic calorimeters :*

Revised September 2015 by R.-Y. Zhu (California Institute of Technology).

The development of electromagnetic showers is discussed in the section on “Passage of Particles Through Matter” (Sec. 34 of this *Review*). Formulae are given which approximately describe average showers, but since the physics of electromagnetic showers is well understood, detailed and reliable Monte Carlo simulation is possible.  $\text{EGS4}$  [157] and  $\text{GEANT}$  [158] have emerged as the standards.

There are homogeneous and sampling electromagnetic calorimeters. In a homogeneous calorimeter the entire volume is sensitive, *i.e.*, contributes signal. Homogeneous electromagnetic calorimeters may be built with inorganic heavy (high- $Z$ ) scintillating crystals such as  $\text{BaF}_2$ ,  $\text{BGO}$ ,  $\text{CsI}$ ,  $\text{LYSO}$ ,  $\text{NaI}$  and  $\text{PWO}$ , non-scintillating Cherenkov radiators such as lead glass and lead fluoride ( $\text{PbF}_2$ ), or ionizing noble liquids. Properties of commonly used inorganic crystal scintillators can be found in Table 35.4. A sampling calorimeter consists of an active medium which generates signal and a passive medium which functions as an absorber. The active medium may be a scintillator, an ionizing noble liquid, a semiconductor, or a gas chamber. The passive medium is usually a material of high density, such as lead, tungsten, iron, copper, or depleted uranium.

The energy resolution  $\sigma_E/E$  of a calorimeter can be parameterized as  $a/\sqrt{E} \oplus b \oplus c/E$ ,

where  $\oplus$  represents addition in quadrature and  $E$  is in GeV. The stochastic term  $a$  represents statistics-related fluctuations such as intrinsic shower fluctuations, photoelectron statistics, dead material at the front of the calorimeter, and sampling fluctuations. For a fixed number of radiation lengths, the stochastic term  $a$  for a sampling calorimeter is expected to be proportional to  $\sqrt{t/f}$ , where  $t$  is plate thickness and  $f$  is sampling fraction [159,160]. While  $a$  is at a few percent level for a homogeneous calorimeter, it is typically 10% for sampling calorimeters.

The main contributions to the systematic, or constant, term  $b$  are detector non-uniformity and calibration uncertainty. In the case of the hadronic cascades discussed below, non-compensation also contributes to the constant term. One additional contribution to the constant term for calorimeters built for modern high-energy physics experiments, operated in a high-beam intensity environment, is radiation damage of the active medium. This can be mitigated by developing radiation-hard active media [52], by reducing the signal path length [55] and by frequent *in situ* calibration and monitoring [51,160]. With effort, the constant term  $b$  can be reduced to below one percent. The term  $c$  is due to electronic noise summed over readout channels within a few Molière radii. The best energy resolution for electromagnetic shower measurement is obtained in total absorption homogeneous calorimeters, *e.g.* calorimeters built with heavy crystal scintillators. These are used when ultimate performance is pursued.

The position resolution depends on the effective Molière radius and the transverse granularity of the calorimeter. Like the energy resolution, it can be factored as  $a/\sqrt{E} \oplus b$ , where  $a$  is a few to 20 mm and  $b$  can be as small as a fraction of mm for a dense calorimeter with fine granularity. Electromagnetic calorimeters may also provide direction measurement for electrons and photons. This is important for photon-related physics when there are uncertainties in event origin, since photons do not leave information in the particle tracking system. Typical photon angular resolution is about  $45 \text{ mrad}/\sqrt{E}$ , which can be provided by implementing longitudinal segmentation [161] for a sampling calorimeter or by adding a preshower detector [162] for a homogeneous calorimeter without longitudinal segmentation.

Novel technologies have been developed for electromagnetic calorimetry. New heavy crystal scintillators, such as PWO and LYSO:Ce (see Sec. 35.4), have attracted much attention. In some cases, such as PWO, it has received broad applications in high-energy and nuclear physics experiments. The “spaghetti” structure has been developed for sampling calorimetry with scintillating fibers as the sensitive medium. The “shashlik” structure has been developed for sampling calorimetry with wavelength shifting fibers functioning as both the converter and transporter for light generated in the sensitive medium. The “accordion” structure has been developed for sampling calorimetry with ionizing noble liquid as the sensitive medium.

Table 35.8 provides a brief description of typical electromagnetic calorimeters built recently for high-energy physics experiments. Also listed in this table are calorimeter depths in radiation lengths ( $X_0$ ) and the achieved energy resolution. Whenever possible, the performance of calorimeters *in situ* is quoted, which is usually in good agreement with prototype test beam results as well as EGS or GEANT simulations, provided that all systematic effects are properly included. Detailed references on detector design and

performance can be found in Appendix C of reference [160] and Proceedings of the International Conference series on Calorimetry in High Energy Physics.

**Table 35.8:** Resolution of typical electromagnetic calorimeters.  $E$  is in GeV.

Technology (Experiment)	Depth	Energy resolution	Date
NaI(Tl) (Crystal Ball)	$20X_0$	$2.7\%/E^{1/4}$	1983
Bi <sub>4</sub> Ge <sub>3</sub> O <sub>12</sub> (BGO) (L3)	$22X_0$	$2\%/\sqrt{E} \oplus 0.7\%$	1993
CsI (KTeV)	$27X_0$	$2\%/\sqrt{E} \oplus 0.45\%$	1996
CsI(Tl) (BaBar)	$16-18X_0$	$2.3\%/E^{1/4} \oplus 1.4\%$	1999
CsI(Tl) (BELLE)	$16X_0$	1.7% for $E_\gamma > 3.5$ GeV	1998
PbWO <sub>4</sub> (PWO) (CMS)	$25X_0$	$3\%/\sqrt{E} \oplus 0.5\% \oplus 0.2/E$	1997
Lead glass (OPAL)	$20.5X_0$	$5\%/\sqrt{E}$	1990
Liquid Kr (NA48)	$27X_0$	$3.2\%/\sqrt{E} \oplus 0.42\% \oplus 0.09/E$	1998
Scintillator/depleted U (ZEUS)	$20-30X_0$	$18\%/\sqrt{E}$	1988
Scintillator/Pb (CDF)	$18X_0$	$13.5\%/\sqrt{E}$	1988
Scintillator fiber/Pb spaghetti (KLOE)	$15X_0$	$5.7\%/\sqrt{E} \oplus 0.6\%$	1995
Liquid Ar/Pb (NA31)	$27X_0$	$7.5\%/\sqrt{E} \oplus 0.5\% \oplus 0.1/E$	1988
Liquid Ar/Pb (SLD)	$21X_0$	$8\%/\sqrt{E}$	1993
Liquid Ar/Pb (H1)	$20-30X_0$	$12\%/\sqrt{E} \oplus 1\%$	1998
Liquid Ar/depl. U (DØ)	$20.5X_0$	$16\%/\sqrt{E} \oplus 0.3\% \oplus 0.3/E$	1993
Liquid Ar/Pb accordion (ATLAS)	$25X_0$	$10\%/\sqrt{E} \oplus 0.4\% \oplus 0.3/E$	1996

## 35.9.2. Hadronic calorimeters : [1–5,160]

Revised September 2013 by D. E. Groom (LBNL).

Hadronic calorimetry is considerably more difficult than EM calorimetry. For the same cascade containment fraction discussed in the previous section, the calorimeter would need to be  $\sim 30$  times deeper. Electromagnetic energy deposit from the decay of a small number of  $\pi^0$ 's are usually detected with greater efficiency than are the hadronic parts of the cascade, themselves subject to large fluctuations in neutron production, undetectable energy loss to nuclear disassociation, and other effects.

Most large hadron calorimeters are parts of large  $4\pi$  detectors at colliding beam facilities. At present these are sampling calorimeters: plates of absorber (Fe, Pb, Cu, or occasionally U or W) alternating with plastic scintillators (plates, tiles, bars), liquid argon (LAr), or gaseous detectors. The ionization is measured directly, as in LAr calorimeters, or via scintillation light observed by photodetectors (usually PMT's or silicon photodiodes). Wavelength-shifting fibers are often used to solve difficult problems of geometry and light collection uniformity. Silicon sensors are being studied for ILC detectors; in this case  $e-h$  pairs are collected. There are as many variants of these schemes as there are calorimeters, including variations in geometry of the absorber and sensors, *e.g.*, scintillating fibers threading an absorber [163], and the "accordion" LAr detector [164]. The latter has zig-zag absorber plates to minimize channeling effects; the calorimeter is hermetic (no cracks), and plates are oriented so that cascades cross the same plate repeatedly. Another departure from the traditional sandwich structure is the LAr-tube design shown in Fig. 35.22(a) [165].

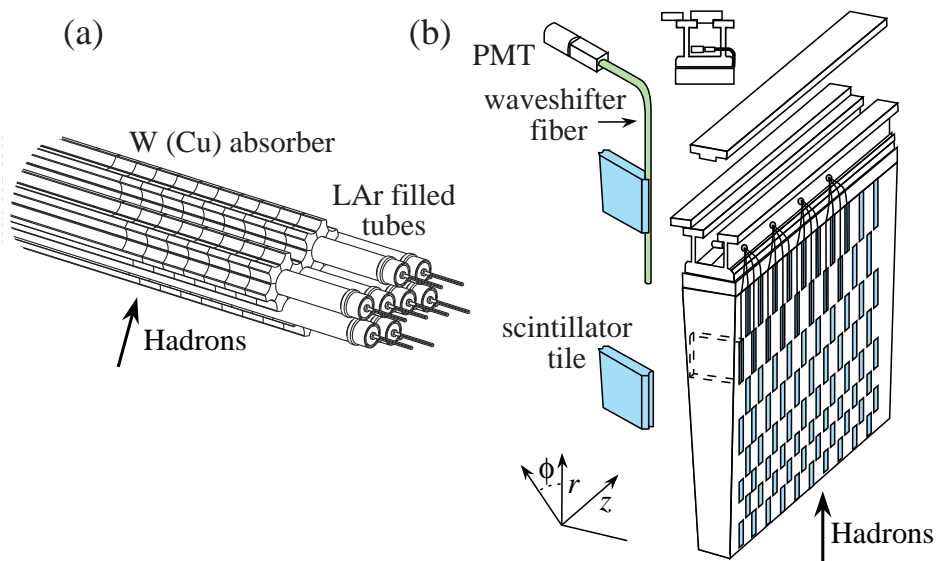


**Figure 35.22:** (a) ATLAS forward hadronic calorimeter structure (FCal2, 3) [165]. Tubes containing LAr are embedded in a mainly tungsten matrix. (b) ATLAS central calorimeter wedge; iron with plastic scintillator tile with wavelength-shifting fiber readout [166].

A relatively new variant in hadron calorimetry is the detection of Cerenkov light. Such

a calorimeter is sensitive to relativistic  $e^\pm$ 's in the EM showers plus a few relativistic pions. An example is the radiation-hard forward calorimeter in CMS, with iron absorber and quartz fiber readout by PMT's [167].

Ideally the calorimeter is segmented in  $\phi$  and  $\theta$  (or  $\eta = -\ln \tan(\theta/2)$ ). Fine segmentation, while desirable, is limited by cost, readout complexity, practical geometry, and the transverse size of the cascades—but see Ref. 168. An example, a wedge of the ATLAS central barrel calorimeter, is shown in Fig. 35.22(b) [166].

Much of the following discussion assumes an idealized calorimeter, with the same structure throughout and without leakage. “Real” calorimeters usually have an EM detector in front and a coarse “catcher” in the back. Complete containment is generally impractical.

In an inelastic hadronic collision a significant fraction  $f_{em}$  of the energy is removed from further hadronic interaction by the production of secondary  $\pi^0$ 's and  $\eta$ 's, whose decay photons generate high-energy electromagnetic (EM) showers. Charged secondaries ( $\pi^\pm$ ,  $p$ , ...) deposit energy via ionization and excitation, but also interact with nuclei, producing spallation protons and neutrons, evaporation neutrons, and spallation products. The charged collision products produce detectable ionization, as do the showering  $\gamma$ -rays from the prompt de-excitation of highly excited nuclei. The recoiling nuclei generate little or no detectable signal. The neutrons lose kinetic energy in elastic collisions, thermalize on a time scale of several  $\mu$ s, and are captured, with the production of more  $\gamma$ -rays—usually outside the acceptance gate of the electronics. Between endothermic spallation losses, nuclear recoils, and late neutron capture, a significant fraction of the hadronic energy (20%–40%, depending on the absorber and energy of the incident particle) is used to overcome nuclear binding energies and is therefore lost or “invisible.”

In contrast to EM showers, hadronic cascade processes are characterized by the production of relatively few high-energy particles. The lost energy and  $f_{em}$  are highly variable from event to event. Until there is event-by-event knowledge of both the EM fraction and the invisible energy loss, the energy resolution of a hadron calorimeter will remain significantly worse than that of its EM counterpart.

The efficiency  $e$  with which EM deposit is detected varies from event to event, but because of the large multiplicity in EM showers the variation is small. In contrast, because a variable fraction of the hadronic energy deposit is detectable, the efficiency  $h$  with which hadronic energy is detected is subject to considerably larger fluctuations. It thus makes sense to consider the ratio  $h/e$  as a stochastic variable.

Most energy deposit is by very low-energy electrons and charged hadrons. Because so many generations are involved in a high-energy cascade, the hadron spectra in a given material are essentially independent of energy except for overall normalization [170]. For this reason  $\langle h/e \rangle$  is a robust concept, independently of hadron energy and species.

If the detection efficiency for the EM sector is  $e$  and that for the hadronic sector is  $h$ , then the ratio of the mean response to a pion relative to that for an electron is

$$\langle \pi/e \rangle = \langle f_{em} \rangle + \langle f_h \rangle \langle h/e \rangle^* = 1 - (1 - \langle h/e \rangle) \langle f_h \rangle \quad (35.34)$$

It has been shown by a simple induction argument and verified by experiment, that the

---

\* Technically, we should write  $\langle f_h(h/e) \rangle$ , but we approximate it as  $\langle f_h \rangle \langle h/e \rangle$  to facilitate

decrease in the average value of the hadronic energy fraction  $\langle f_h \rangle = 1 - \langle f_{em} \rangle$  as the projectile energy  $E$  increases is fairly well described by the power law [169,170]

$$\langle f_h \rangle \approx (E/E_0)^{m-1} \quad (\text{for } E > E_0), \quad (35.35)$$

at least up to a few hundred GeV. The exponent  $m$  depends logarithmically on the mean multiplicity and the mean fractional loss to  $\pi^0$  production in a single interaction. It is in the range 0.80–0.87.  $E_0$ , roughly the energy for the onset of inelastic collisions, is 1 GeV or a little less for incident pions [169]. Both  $m$  and  $E_0$  must be obtained experimentally for a given calorimeter configuration.

Only the product  $(1 - \langle h/e \rangle)E_0^{1-m}$  can be obtained by measuring  $\langle \pi/e \rangle$  as a function of energy. Since  $1 - m$  is small and  $E_0 \approx 1$  GeV for pion-induced cascades, this fact is usually ignored and  $\langle h/e \rangle$  is reported.

In a hadron-nucleus collision a large fraction of the incident energy is carried by a “leading particle” with the same quark content as the incident hadron. If the projectile is a charged pion, the leading particle is usually a pion, which can be neutral and hence contributes to the EM sector. This is not true for incident protons. The result is an increased mean hadronic fraction for incident protons:  $E_0 \approx 2.6$  GeV [169–172].

By definition,  $0 \leq f_{em} \leq 1$ . Its variance  $\sigma_{f_{em}}^2$  changes only slowly with energy, but perforce  $\langle f_{em} \rangle \rightarrow 1$  as the projectile energy increases. An empirical power law (unrelated to Eq. (35.34)) of the form  $\sigma_{f_{em}} = (E/E_1)^{1-\ell}$  (where  $\ell < 1$ ) describes the energy dependence of the variance adequately and has the right asymptotic properties [160]. For  $\langle h/e \rangle \neq 1$  (*noncompensation*), fluctuations in  $f_{em}$  significantly contribute to or even dominate the resolution. Since the  $f_{em}$  distribution has a high-energy tail, the calorimeter response is non-Gaussian with a high-energy tail if  $\langle h/e \rangle < 1$ . Noncompensation thus seriously degrades resolution and produces a nonlinear response.

It is clearly desirable to *compensate* the response, *i.e.*, to design the calorimeter such that  $\langle h/e \rangle = 1$ . This is possible only with a sampling calorimeter, where several variables can be chosen or tuned:

1. Decrease the EM sensitivity. EM cross sections increase with  $Z$ ,<sup>†</sup> and most of the energy in an EM shower is deposited by low-energy electrons. A disproportionate fraction of the EM energy is thus deposited in the higher- $Z$  absorber. Lower- $Z$  cladding, such as the steel cladding on ZEUS U plates, preferentially absorbs low-energy  $\gamma$ 's in EM showers and thus also lowers the electronic response. G10 signal boards in the DØ calorimeters and G10 next to silicon readout detectors has the same effect. The degree of EM signal suppression can be somewhat controlled by tuning the sensor/absorber thickness ratio.
2. Increase the hadronic sensitivity. The abundant neutrons produced in the cascade have large  $n$ - $p$  elastic scattering cross sections, so that low-energy scattered protons are produced in hydrogenous sampling materials such as butane-filled proportional counters or plastic scintillator. (The maximal fractional energy loss when a neutron

---

the rest of the discussion.

<sup>†</sup> The asymptotic pair-production cross section scales roughly as  $Z^{0.75}$ , and  $|dE/dx|$  slowly decreases with increasing  $Z$ .



scatters from a nucleus with mass number  $A$  is  $4A/(1+A)^2$ .) The down side in the scintillator case is that the signal from a highly-ionizing stopping proton can be reduced by as much as 90% by recombination and quenching parameterized by Birks' Law (Eq. (35.2)).

3. Fabjan and Willis proposed that the additional signal generated in the aftermath of fission in  $^{238}\text{U}$  absorber plates should compensate nuclear fluctuations [173]. The production of fission fragments due to fast  $n$  capture was later observed [174]. However, while a very large amount of energy is released, it is mostly carried by low-velocity, very highly ionizing fission fragments which produce very little observable signal because of recombination and quenching. But in fact much of the compensation observed with the ZEUS  $^{238}\text{U}$ /scintillator calorimeter was mainly the result of methods 1 and 2 above.

Motivated very much by the work of Brau, Gabriel, Brückmann, and Wigmans [175], several groups built calorimeters which were very nearly compensating. The degree of compensation was sensitive to the acceptance gate width, and so could be somewhat further tuned. These included

- a) HELIOS with 2.5 mm thick scintillator plates sandwiched between 2 mm thick  $^{238}\text{U}$  plates (one of several structures);  $\sigma/E = 0.34/\sqrt{E}$  was obtained,
- b) ZEUS, 2.6 cm thick scintillator plates between 3.3 mm  $^{238}\text{U}$  plates;  $\sigma/E = 0.35/\sqrt{E}$ ,
- c) a ZEUS prototype with 10 mm Pb plates and 2.5 mm scintillator sheets;  $\sigma/E = 0.44/\sqrt{E}$ , and
- d) DØ, where the sandwich cell consists of a 4–6 mm thick  $^{238}\text{U}$  plate, 2.3 mm LAr, a G-10 signal board, and another 2.3 mm LAr gap;  $\sigma/E \approx 0.45/\sqrt{E}$ .

Given geometrical and cost constraints, the calorimeters used in modern collider detectors are not compensating:  $\langle h/e \rangle \approx 0.7$ , for the ATLAS central barrel calorimeter, is typical.

A more versatile approach to compensation is provided by a *dual-readout calorimeter*, in which the signal is sensed by two readout systems with highly contrasting  $\langle h/e \rangle$ . Although the concept is more than two decades old [176], it was only recently been implemented by the DREAM collaboration [177]. The test beam calorimeter consisted of copper tubes, each filled with scintillator and quartz fibers. If the two signals  $C$  and  $S$  (quartz and scintillator) are both normalized to electron response, then for each event Eq. (35.34) takes the form

$$\begin{aligned} C &= E[f_{em} + \langle h/e \rangle|_C(1 - f_{em})] \\ S &= E[f_{em} + \langle h/e \rangle|_S(1 - f_{em})] \end{aligned} \quad (35.36)$$

for the Cherenkov and scintillator responses. On a dotplot of  $C/E$  vs  $S/E$ , events scatter about a line-segment locus described in Fig. 35.23. With increasing energy the distribution moves upward along the locus and becomes tighter. Equations 35.36 are linear in  $1/E$  and  $f_{em}$ , and are easily solved to obtain estimators of the *corrected* energy and  $f_{em}$  for each event. Both are subject to resolution effects, but contributions due to fluctuations in  $f_{em}$  are eliminated. The solution for the corrected energy is given by [170]:

$$E = \frac{\xi S - C}{\xi - 1}, \quad \text{where } \xi = \frac{1 - \langle h/e \rangle|_C}{1 - \langle h/e \rangle|_S} \quad (35.37)$$

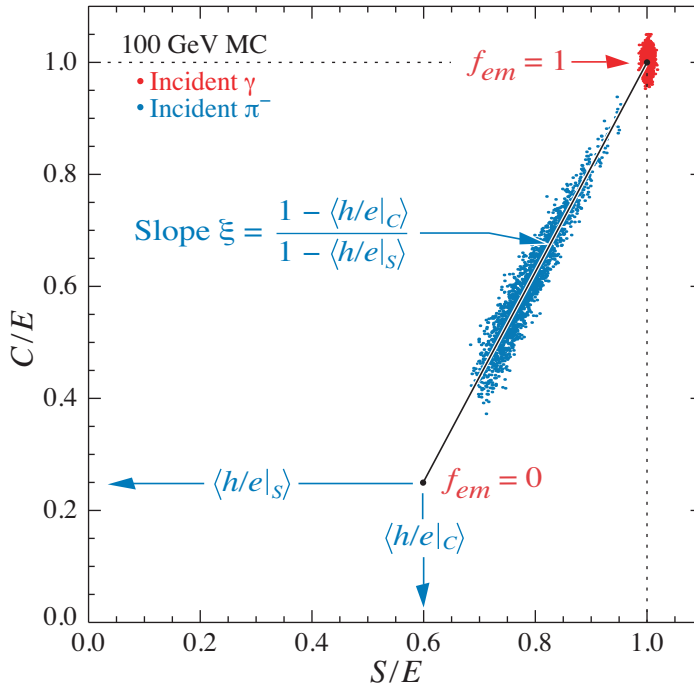


**Figure 35.23:** Dotplot of Monte Carlo C (Cherenkov) vs S (scintillator) signals for individual events in a dual readout calorimeter. Hadronic ( $\pi^-$ ) induced events are shown in blue, and scatter about the indicated event locus. Electromagnetic events cluster about  $(C,S) = (0,0)$ . In this case worse resolution (fewer p.e.'s) was assumed for the Cherenkov events, leading to the “elliptical” distribution.

$\xi$  is the energy-independent slope of the event locus on a plot of  $C$  vs  $S$ . It can be found either from the fitted slope or by measuring  $\pi/e$  as a function of  $E$ . Because we have no knowledge of  $h/e$  on an event-by-event basis, it has been replaced by  $\langle h/e \rangle$  in Eq. (35.37).  $\xi$  must be as far from unity as possible to optimize resolution, which means in practical terms that the scintillator readout of the calorimeter must be as compensating as possible.

Although the usually-dominant contribution of the  $f_{em}$  distribution to the resolution can be minimized by compensation or the use of dual calorimetry, there remain significant contributions to the resolution:

1. Incomplete corrections for leakage, differences in light collection efficiency, and electronics calibration.
2. Readout transducer shot noise (usually photoelectron statistics), plus electronic noise.
3. Sampling fluctuations. Only a small part of the energy deposit takes place in the scintillator or other sensor, and that fraction is subject to large fluctuations. This can be as high as  $40\%/\sqrt{E}$  (lead/scintillator). It is even greater in the Fe/scint case because of the very small sampling fraction (if the calorimeter is to be compensating), and substantially lower in a U/scint calorimeter. It is obviously zero for a homogeneous calorimeter.
4. Intrinsic fluctuations. The many ways ionization can be produced in a hadronic shower have different detection efficiencies and are subject to stochastic fluctuations. In particular, a very large fraction of the hadronic energy ( $\sim 20\%$  for Fe/scint,  $\sim 40\%$

for U/scint) is “invisible,” going into nuclear dissociation, thermalized neutrons, etc. The lost fraction depends on readout—it will be greater for a Cherenkov readout, less for an organic scintillator readout.

Except in a sampling calorimeter especially designed for the purpose, sampling and intrinsic resolution contributions cannot be separated. This may have been best studied by Drews *et al.* [178], who used a calorimeter in which even- and odd-numbered scintillators were separately read out. Sums and differences of the variances were used to separate sampling and intrinsic contributions.

The fractional energy resolution can be represented by

$$\frac{\sigma}{E} = \frac{a_1(E)}{\sqrt{E}} \oplus \left| 1 - \left\langle \frac{h}{e} \right\rangle \right| \left( \frac{E}{E_1} \right)^{1-\ell} \quad (35.38)$$

The coefficient  $a_1$  is expected to have mild energy dependence for a number of reasons. For example, the sampling variance is  $(\pi/e)E$  rather than  $E$ . The term  $(E/E_1)^{1-\ell}$  is the parametrization of  $\sigma_{f_{em}}$  discussed above. Usually a plot of  $(\sigma/E)^2$  vs  $1/E$  is well-described by a straight line (constant  $a_1$ ) with a finite intercept—the square of the right term in Eq. (35.38), is called “the constant term.” Precise data show the slight downturn [163].

After the first interaction of the incident hadron, the average longitudinal distribution rises to a smooth peak. The peak position increases slowly with energy. The distribution becomes nearly exponential after several interaction lengths. Examples from the CDHS magnetized iron-scintillator sandwich calorimeter test beam calibration runs [179] are shown in Fig. 35.24. Proton-induced cascades are somewhat shorter and broader than pion-induced cascades [172]. A gamma distribution fairly well describes the longitudinal development of an EM shower, as discussed in Sec. 34.5. Following this logic, Bock *et al.* suggested that the profile of a hadronic cascade could be fitted by the sum of two  $\Gamma$  distributions, one with a characteristic length  $X_0$  and the other with length  $\lambda_I$  [180]. Fits to this 4-parameter function are commonly used, *e.g.*, by the ATLAS Tilecal collaboration [172]. If the interaction point is not known (the usual case), the distribution must be convoluted with an exponential in the interaction length of the incident particle. Adragna *et al.* give an analytic form for the convoluted function [172].

The transverse energy deposit is characterized by a central core dominated by EM cascades, together with a wide “skirt” produced by wide-angle hadronic interactions [181].

The CALICE collaboration has tested a “tracking” calorimeter (AHCAL) with highly granular scintillator readout [168]. Since the position of the first interaction is observed, the average longitudinal and radial shower distributions are obtained.

While the average distributions might be useful in designing a calorimeter, they have little meaning for individual events, whose distributions are extremely variable because of the small number of particles involved early in the cascade.

Particle identification, primarily  $e-\pi$  discrimination, is accomplished in most calorimeters by depth development. An EM shower is mostly contained in  $15X_0$  while a hadronic shower takes about  $4\lambda_I$ . In high- $A$  absorbers such as Pb,  $X_0/\lambda_I \sim 0.03$ . In a fiber calorimeter, such as the RD52 dual-readout calorimeter [182],  $e-\pi$  discrimination is achieved by differences in the Cerenkov and scintillation signals, lateral spread, and timing differences, ultimately achieving about 500:1 discrimination.

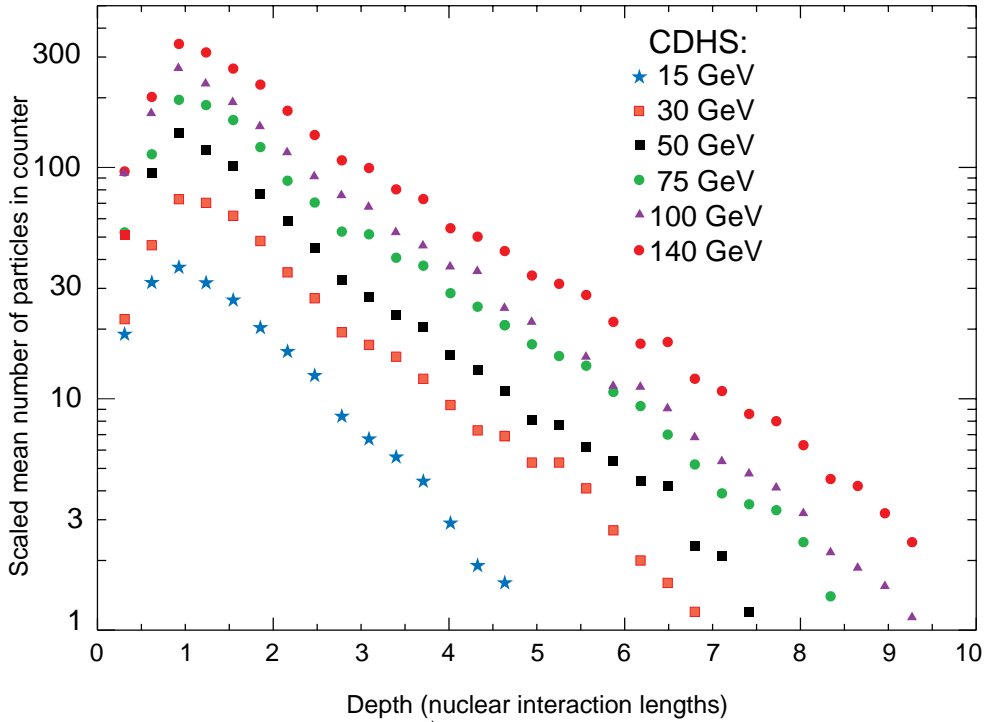


**Figure 35.24:** Mean profiles of  $\pi^+$  (mostly) induced cascades in the CDHS neutrino detector [179]. Corresponding results for the ATLAS tile calorimeter can be found in Ref. 172.

### 35.9.3. Free electron drift velocities in liquid ionization chambers :

Written August 2009 by W. Walkowiak (U. Siegen)

Drift velocities of free electrons in LAr [183] are given as a function of electric field strength for different temperatures of the medium in Fig. 35.25. The drift velocities in LAr have been measured using a double-gridded drift chamber with electrons produced by a laser pulse on a gold-plated cathode. The average temperature gradient of the drift velocity of the free electrons in LAr is described [183] by

$$\frac{\Delta v_d}{\Delta T v_d} = (-1.72 \pm 0.08) \% / \text{K}.$$

Earlier measurements [184–187] used different techniques and show systematic deviations of the drift velocities for free electrons which cannot be explained by the temperature dependence mentioned above.

Drift velocities of free electrons in LXe [185] as a function of electric field strength are also displayed in Fig. 35.25. The drift velocity saturates for  $|\mathbf{E}| > 3$  kV/cm, and decreases with increasing temperature for LXe as well as measured e.g. by [188].

The addition of small concentrations of other molecules like  $\text{N}_2$ ,  $\text{H}_2$  and  $\text{CH}_4$  in solution to the liquid typically increases the drift velocities of free electrons above the saturation value [185,186], see example for  $\text{CH}_4$  admixture to LAr in Fig. 35.25. Therefore, actual drift velocities are critically dependent on even small additions or contaminations.

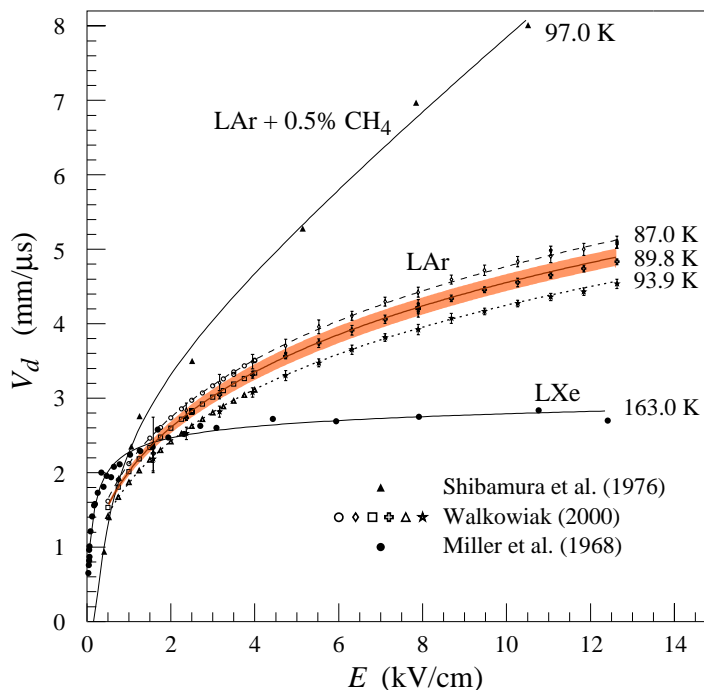


**Figure 35.25:** Drift velocity of free electrons as a function of electric field strength for LAr [183], LAr + 0.5% CH<sub>4</sub> [185] and LXe [184]. The average temperatures of the liquids are indicated. Results of a fit to an empirical function [189] are superimposed. In case of LAr at 91 K the error band for the global fit [183] including statistical and systematic errors as well as correlations of the data points is given. Only statistical errors are shown for the individual LAr data points.

## 35.10. Accelerator-based Neutrino Detectors

Revised August 2017 by M.O. Wascko (Imperial College London).

### 35.10.1. Introduction :

Accelerator-based neutrino experiments span many orders of magnitude in neutrino energy, from a few MeV to hundreds of GeV. This wide range of neutrino energy is driven by the many physics applications of accelerator-based neutrino beams. Foremost among them is neutrino oscillation, which varies as the ratio  $L/E_\nu$ , where  $L$  is the neutrino baseline (distance traveled), and  $E_\nu$  is the neutrino energy. But accelerator-based neutrino beams have also been used to study the nature of the weak interaction, to probe nucleon form factors and structure functions, and to study nuclear structure.

The first accelerator-based neutrino experiment used neutrinos from the decays of high energy pions in flight to show that the neutrinos emitted from pion decay are different from the neutrinos emitted by beta decay [190]. The field of accelerator-based neutrino experiments would likely not have expanded beyond this without Simon van der Meer's invention of the magnetic focusing horn [191], which significantly increased the flux of neutrinos aimed toward the detector. In this mini-review, we focus on experiments employing decay-in-flight beams—pions, kaons, charmed mesons, and taus—producing fluxes of neutrinos and antineutrinos from  $\sim 10$  MeV to  $\sim 100$  GeV.

Neutrino interactions with matter proceed only through the weak interaction, making

the cross section extremely small and requiring high fluxes of neutrinos and large detector masses in order to achieve satisfactory event rates. Therefore, neutrino detector design is a balancing act taking into account sufficient numbers of nuclear targets (often achieved with inactive detector materials), adequate sampling/segmentation to ensure accurate reconstruction of the tracks and showers produced by neutrino-interaction secondary particles, and practical readout systems to allow timely analysis of data.

### 35.10.2. *Signals and Backgrounds :*

The neutrino interaction processes available increase with increasing neutrino energy as interaction thresholds are crossed; in general neutrino-interaction cross sections grow with energy; for a detailed discussion of neutrino interactions see [192]. The multiplicity of secondary particles from each interaction process grows in complexity with neutrino energy, while the forward-boost due to increasing  $E_\nu$  compresses the occupied phase space in the lab frame, impacting detector designs. Because decay-in-flight beams produce neutrinos at well-defined times, leading to very small duty factors, the predominant backgrounds usually stem from unwanted beam-induced neutrino interactions, i.e. neutrinos interacting via other processes than the one being studied. A noteworthy exception is time projection chambers, wherein the long drift times can admit substantially more cosmic backgrounds than most other detection methods. Cosmic backgrounds are more rare at higher energies because the secondary particles produced by neutrino interactions yield detector signals that resemble cosmic backgrounds less and less.

Below, we describe a few of the dominant neutrino interaction processes, with a focus on the final state particle content and topologies.

#### 35.10.2.1. *Charged-Current Quasi-Elastic Scattering and Pion Production:*

Below  $\sim 2$  GeV neutrino energy, the dominant neutrino-nucleus interaction process is quasi-elastic (QE) scattering. In the charged current (CC) mode, the CCQE base neutrino reaction is  $\nu_\ell n \rightarrow \ell^- p$ , where  $\ell = e, \mu, \tau$ , and similarly for antineutrinos,  $\bar{\nu}_\ell p \rightarrow \ell^+ n$ . The final state particles are a charged lepton, and perhaps a recoiling nucleon if it is given enough energy to escape the nucleus. Detectors designed to observe this process should have good single-particle track resolution for muon neutrino interactions, but should have good  $\mu/e$  separation for electron neutrino interactions. Because the interaction cross section falls sharply with  $Q^2$ , the lepton typically carries away more of the neutrino's kinetic energy than the recoiling nucleon. The fraction of backward-scattered leptons is large, however, so detectors with  $4\pi$  coverage are desirable. The dominant backgrounds in this channel tend to come from single pion production events in which the pion is not detected.

Near 1 GeV, the quasi-elastic cross section is eclipsed by pion production processes. A typical single pion production (CC1 $\pi$ ) reaction is  $\nu_\ell n \rightarrow \ell^- \pi^+ n$ , but many more final state particle combinations are possible. Single pion production proceeds through the coherent channel and many incoherent processes, dominated by resonance production. With increasing neutrino energy, higher-order resonances can be excited, leading to multiple pions in the final state. Separating these processes from quasi-elastic scattering, and indeed from each other, requires tagging, and ideally reconstructing, the pions. Since these processes can produce neutral pions, electromagnetic (EM) shower reconstruction

is more important here than it is for the quasi-elastic channel. The predominant backgrounds for pion production change with increasing neutrino energy. Detection of pion processes is also complicated because near threshold the quasi-elastic channel creates pion backgrounds through final state interactions of the recoiling nucleon, and at higher energies backgrounds come from migration of multiple pion events in which one or more pions is not detected.

#### **35.10.2.2. *Deep Inelastic Scattering:***

Beyond a few GeV, the neutrino has enough energy to probe the nucleon at the parton scale, leading to deep inelastic scattering (DIS). In the charged-current channel, the DIS neutrino reaction is  $\nu_\ell N \rightarrow \ell^- X$ , where  $N$  is a nucleon and  $X$  encompasses the entire recoiling hadronic system. The final state particle reconstruction revolves around accurate reconstruction of the lepton momentum and containment and reconstruction of the hadronic shower energy. Because of the high neutrino energies involved, DIS events are very forward boosted, and can have extremely long particle tracks. For this reason, detectors measuring DIS interactions must be large to contain the hadronic showers in the detector volume.

#### **35.10.2.3. *Neutral Currents:***

Neutrino interactions proceeding through the neutral current (NC) channel are identified by the lack of a charged lepton in the final state. For example, the NC elastic reaction is  $\nu_\ell N \rightarrow \nu_\ell N$ , and the NC DIS reaction is  $\nu_\ell N \rightarrow \nu_\ell X$ . NC interactions are suppressed relative to CC interactions by a factor involving the weak mixing angle; the primary backgrounds for NC interactions come from CC interactions in which the charged lepton is misidentified.

### **35.10.3. *Instances of Neutrino Detector Technology :***

Below we describe many of the actual detectors that have been built and operated for use in accelerator-based neutrino beams.

#### **35.10.3.1. *Spark Chambers:***

In the first accelerator-based neutrino beam experiment, Lederman, Schwartz, and Steinberger [190] used an internally-triggered spark chamber detector, filled with 10 tons of Al planes and surrounded by external scintillator veto planes, to distinguish muon tracks from electron showers, and hence muon neutrinos from electron neutrinos. The inactive Al planes served as the neutrino interaction target and as radiators for EM shower development. The detector successfully showed the presence of muon tracks from neutrino interactions. It was also sensitive to the hadronic showers induced by NC interactions, which were unknown at the time. In 1963, CERN also built and ran a large (20 ton) Al plane spark chamber in a wideband beam based on the PS accelerator. [193]. More than a decade later, the Aachen-Padova [195] experiment at CERN employed a 30 ton Al spark chamber in the PS-WBB.

**Table 35.9:** Properties of detectors for accelerator-based neutrino beams.

Name	Type	Target	Mass* (t)	Location	$\langle E_\nu \rangle$ (GeV)	Dates
Lederman et al.	Spark	Al	10	BNL	0.2–2	1962
CERN-spark	Spark	Al	20	CERN	1.5	1964
Serpukhov	Spark	Al	20	IHEP	4	1977
Aachen-Padova	Spark	Al	30	CERN	1.5	1976–77
Gargamelle	Bubble	Freon	6	CERN	1.5,20	1972,1977
BEBC	Bubble	H,D,Ne-H	2–42	CERN	50,150 & 20	1977–84
SKAT	Bubble	Freon	8	IHEP	4	1977–1987
ANL-12ft	Bubble	H,D	1–2	ANL	0.5	1970
BNL-7ft	Bubble	H,D	0.4–0.9	BNL	1.3,3	1976–82
Fermilab-15ft	Bubble	D,Ne	1–20	FNAL	50,180&25,100	1974–92
CITF	Iron	Fe	92	FNAL	50,180	1977–83
CDHS	Iron	Fe	750	CERN	50,150	1977–83
MINOS	Iron	Fe	980,5.4k	FNAL	4–15	2005–2016
INGRID	Iron	Fe	99	J-PARC	0.7–3	2009–
Super-Kamiokande	Cherenkov	H <sub>2</sub> O	22,500	Kamioka	0.6	1996–
K2K-1kt	Cherenkov	H <sub>2</sub> O	25	KEK	0.8	1998–2004
MiniBooNE	Cherenkov	CH <sub>2</sub>	440	FNAL	0.6	2002–12
HWPF	Scintillation	CH <sub>2</sub>	2	FNAL	2	2014–
LSND	Scintillation	CH <sub>2</sub>	130	LANL	0.06	1993–98
NOvA	Scintillation	CH <sub>2</sub>	300,14k	FNAL/Ash River	2	2013–
SciBar	Scintillation	CH	12	KEK/FNAL	0.8,0.6	2004,2007–8
ICARUS	LArTPC	Ar	760	LNGS	20	2006–12
Argoneut	LArTPC	Ar	0.025	FNAL	3	2009–10
MicroBooNE	LArTPC	Ar	170	FNAL	0.8	2014–
FNAL-E-531	Emulsion	Ag, Br	0.009	FNAL	25	1984
CHORUS	Emulsion	Ag, Br	1.6	CERN	20	1995
DONuT	Emulsion	Fe	0.26	FNAL	100	1997
OPERA	Emulsion	Pb	1.3k	LNGS	20	2006–12
NINJA	Emulsion	Fe	0.001	J-PARC	0.6	2016–
CHARM	Hybrid	CaCO <sub>3</sub> O	150	CERN	20	1977
CHARM-II	Hybrid	Si	692	CERN	20	1983
BNL-E-734	Hybrid	CH <sub>2</sub>	172	BNL	1.3	1987
BNL-E-776	Hybrid	concrete	240	BNL	3	1990
NOMAD	Hybrid	CH	3	CERN	20	1995–98
CCFR	Hybrid	Fe	690	FNAL	90,260	1991
NuTeV	Hybrid	Fe	690	FNAL	70,180	1996–97
MINERvA	Hybrid	CH,H <sub>2</sub> O,Fe,Pb,C,He	8	FNAL	3,8	2009–
T2K-ND280	Hybrid	CH,H <sub>2</sub> O,Pb,Cu	4	J-PARC	0.6	2009–

\* Fiducial.



**35.10.3.2. Bubble Chambers:**

Several large bubble chamber detectors were employed as accelerator neutrino detectors in the 1970s and 80s, performing many of the first studies of the properties of the weak interaction. Bubble chambers provide exquisite granularity in the reconstruction of secondary particles, allowing very accurate separation of interaction processes. However, the extremely slow and labor-intensive acquisition and analysis of the data from photographic film led to them being phased out in favor of electronically read out detectors.

The Gargamelle [196] detector at CERN used Freon and propane gas targets to make the first observation of neutrino-induced NC interactions and more. The BEBC [197] detector at CERN was a bubble chamber that was alternately filled with liquid hydrogen, deuterium, and a neon-hydrogen mixture; BEBC was also outfitted with a track-sensitive detector to improve event tagging, and sometimes used with a small emulsion chamber. The SKAT [194] Freon bubble chamber was exposed to wideband neutrino and antineutrino beams at the Serpukhov laboratory in the former Soviet Union. A series of American bubble chambers in the 1970's and 1980's made measurements on free nucleons that are still crucial inputs for neutrino-nucleus scattering predictions. The 12-foot bubble chamber at ANL [210] in the USA used both deuterium and hydrogen targets, as did the 7-foot bubble chamber at BNL [199]. Fermilab's 15 foot bubble chamber [200] used deuterium and neon targets.

**35.10.3.3. Iron Tracking Calorimeters:**

Because of the forward boost of high energy interactions, long detectors made of magnetized iron interspersed with active detector layers have been very successfully employed. The long magnetized detectors allow measurements of the momentum of penetrating muons. The iron planes also act as shower-inducing layers, allowing separation of EM and hadronic showers; the large number of iron planes provide enough mass for high statistics and/or shower containment. Magnetized iron spectrometers have been used for studies of the weak interaction, measurements of structure functions, and searches for neutrino oscillation. Non-magnetized iron detectors have also been successfully employed as neutrino monitors for oscillation experiments and also for neutrino-nucleus interaction studies.

The Caltech-Fermilab counter (CITF) [210] combined a 92 ton iron-scintillator target-calorimeter detector with a downstream toroidal magnet to perform early studies of weak interactions—including observations of neutral currents. The CDHS [211] detector used layers of magnetized iron modules interspersed with wire drift chambers, with a fiducial mass of 750 t, to detect neutrinos in the range 30–300 GeV. Within each iron module, 5 cm (or 15 cm) iron plates were interspersed with scintillation counters. The MINOS [214] detectors, a near detector of 980 t at FNAL and a far detector of 5400 t in the Soudan mine, were functionally identical magnetized iron calorimeters, comprised of iron plates interleaved with layers of 4 cm wide plastic scintillator strips in alternating orientations. The T2K [234] on-axis detector, INGRID, consists of 16 non-magnetized iron scintillator sandwich detectors, each with nine 6.5 cm iron plane (7.1 t total) interspersed between layers of 5 cm wide plastic scintillator strips readout out by multi-pixel photon counters (MPPCs) coupled to WLS fibers. Fourteen of the

INGRID modules are arranged in a cross-hair configuration centered on the neutrino beam axis.

#### **35.10.3.4.** *Cherenkov Detectors:*

Open volume water Cherenkov detectors were originally built to search for proton decay. Large volumes of ultra-pure water were lined with photomultipliers to collect Cherenkov light emitted by the passage of relativistic charged particles. See Sec. 36.3.1 for a detailed discussion of deep liquid detectors for rare processes. The Cherenkov light, which has significant production in the visible range, appears on the walls of the detectors in distinctive ring patterns, and topological characteristics of the rings are employed to separate muon-induced rings from electron-induced with very high accuracy. As neutrino detectors, Cherenkov detectors optimize the design balance since the entire neutrino target is also active detector medium.

When used to detect  $\sim$  GeV neutrinos, the detector medium acts as a natural filter for final state particles below the Cherenkov threshold; this feature has been exploited successfully by the K2K, MiniBooNE (using mineral oil instead of water), and T2K neutrino oscillation experiments. This makes event reconstruction simple and robust since electrons and muons have very different signatures, but does require making assumptions when inferring neutrino energy since not all final state particles are observed. At higher energies Cherenkov detectors become less accurate because the overlapping rings from many final state particles become increasingly difficult to resolve.

The second-generation Cherenkov detector in Japan, Super-Kamiokande [202] (Super-K), comprises 22.5 kt of water viewed by 50 cm photomultiplier tubes with 40% photocathode coverage; it is surrounded by an outer detector region viewed by 20 cm photomultipliers. Super-K is the far detector for K2K and T2K, and is described in greater detail elsewhere in this review. The K2K experiment also employed a 1 kt water Cherenkov detector in the suite of near detectors [203], with 40% photocathode coverage. The MiniBooNE detector at FNAL was a 0.8 kt [204] mineral oil Cherenkov detector, with 20 cm photomultipliers giving 10% photocathode coverage, surrounded by a veto detector also with 20 cm photomultipliers.

#### **35.10.3.5.** *Scintillation Detectors:*

Liquid and solid scintillator detectors also employ fully (or nearly fully) active detector media. Typically organic scintillators, which emit into the ultraviolet range, are dissolved in mineral oil or plastic and read out by photomultipliers coupled to wavelength shifters (WLS). Open volume scintillation detectors lined with photomultipliers are conceptually similar to Cherenkov detectors, although energy reconstruction is calorimetric in nature as opposed to kinematic (see also Sec. 36.3.1). For higher energies and higher particle multiplicities, it becomes beneficial to use segmented detectors to help distinguish particle tracks and showers from each other.

The HWPF collaboration [206] employed a 2 t liquid scintillator total-absorption hadron calorimeter followed by a magnetic spectrometer to observe neutral current events in the early days of Fermilab. The LSND [207] detector at LANL was a 130 t open volume liquid scintillator detector employed to detect relatively low energy ( $<300$  MeV) neutrinos. The NOvA [209] detectors use segmented volumes of liquid scintillator in which the scintillation light is collected by WLS fibers in the segments that are coupled

to avalanche photodiodes (APDs) at the ends of the volumes. The NOvA far detector, located in Ash River, MN, is comprised of 896 layers of 15.6 m long extruded PVC scintillator cells for a total mass of 14 kt; the NOvA near detector is comprised of 214 layers of 4.1 m scintillator volumes for a total mass of 300 t. Both are placed in the NuMI beamline at  $0.8^\circ$  off-axis. The SciBar (Scintillation Bar) detector was originally built for K2K at KEK in Japan and then re-used for SciBooNE [208] at FNAL. SciBar used plastic scintillator strips with 1.5 cm $\times$ 2.5 cm rectangular cross section, read out by multianode photomultipliers (MAPMTs) coupled to WLS fibers, arranged in alternating horizontal and vertical layers. Both SciBooNE and K2K employed an EM calorimeter downstream of SciBar and a muon range detector (MRD) downstream of that.

### 35.10.3.6. *Liquid Argon Time Projection Chambers:*

Liquid argon time projection chambers (LAr-TPCs) were conceived in the 1970s as a way to achieve a fully active detector with sub-centimeter track reconstruction [215]. A massive volume of purified liquid argon is put under a strong electric field (hundreds of V/cm), so that the liberated electrons from the paths of ionizing particles can be drifted to the edge of the volume and read out, directly by collecting charge from wire planes or non-destructively through charge induction in the wire planes. A dual-phase readout method is also being developed, in which the charge is drifted vertically and then passed through an amplification region inside a gas volume above the liquid volume; the bottom of the liquid volume is equipped with a PMT array for detecting scintillation photons from the liquid argon. The first large scale LAr-TPC was the ICARUS T-600 module [216], comprising 760 t of liquid argon with a charge drift length of 1.5 m read out by wires with 3 mm pitch, which operated in LNGS, both standalone and also exposed to the CNGS high energy neutrino beam. The ICARUS detector has been transported to Fermilab and is being installed in an on-axis position in the Booster Neutrino Beamline, where it will also be exposed to off-axis neutrinos from the NuMI beamline. The ArgoNeuT [217] detector at FNAL, with fiducial mass 25 kg of argon read out with 4 mm pitch wires, was exposed to the NuMI neutrino and antineutrino beams. The MicroBooNE [218] detector at FNAL comprises 170 t of liquid Ar, read out with 3 mm wire pitch, which began collecting data in the Booster Neutrino Beam Oct 2015. A LAr-TPC has also been chosen as the detector design for the future DUNE neutrino oscillation experiment, from FNAL to Sanford Underground Research Facility; both single and dual phase modules are planned.

### 35.10.3.7. *Emulsion Detectors:*

Photographic film emulsions have been employed in particle physics experiments since the 1940s [219]. Thanks to advances in scanning technology and automation [223], they have been successfully employed as neutrino detectors. Emulsions are used for experiments observing CC tau neutrino interactions, where the short lifetime of the tau,  $\tau_\tau = 2.90 \times 10^{-13}$ s, leading to the short mean path length,  $c \times \tau = 87\mu\text{m}$ , requires extremely precise track resolution. They are employed in hybrid detectors in which the emulsion bricks are embedded inside fine-grained tracker detectors. In the data analysis, the tracker data are used to select events with characteristics typical of a tau decay in the final state, such as missing energy and unbalanced transverse momentum. The reconstructed tracks are projected back into an emulsion brick and used as the search

seed for a neutrino interaction vertex.

E531 [220] at Fermilab tested many of the emulsion-tracker hybrid techniques employed by later neutrino experiments, in a detector with approximately 9 kg of emulsion target. The CHORUS [221] experiment at CERN used 1,600 kg of emulsion, in a hybrid detector with a fiber tracker, high resolution calorimeter, and muon spectrometer, to search for  $\nu_\mu \rightarrow \nu_\tau$  oscillation. The DONuT [222] experiment at FNAL used a hybrid detector, with 260 kg of emulsion bricks interspersed with fiber trackers, followed by a magnetic spectrometer, and calorimeter, to make the first direct observation of tau neutrino CC interactions. The OPERA [224,225,226] experiment used an automated hybrid emulsion detector, with 1,300 t of emulsion, to make the first direct observation of the appearance of  $\nu_\tau$  in a  $\nu_\mu$  beam. Recently, the NINJA collaboration has developed an emulsion cloud chamber detector to observe neutrinos in the J-PARC neutrino beam [227].

### 35.10.3.8. *Hybrid Detectors:*

In the previous neutrino detector examples, one can point to a specific detection technology or configuration that defines a category of detectors. In this section we look at detectors that combine multiple elements or techniques, without one facet being specifically dominant or crucial; we call these detectors hybrids.

The CHARM detector [228] at CERN was built to study neutral-current interactions and search for muon neutrino oscillation. It was a fine-grained ionization calorimeter tracker with approximately 150 t of marble as neutrino target, surrounded by a magnetized iron muon system for tagging high angle muons, and followed downstream by a muon spectrometer. The CHARM II detector [229] at CERN comprised a target calorimeter followed by a downstream muon spectrometer. Each target calorimeter module consists of a 4.8 cm thick glass plate followed by a layer of plastic streamer tubes, with spacing 1 cm, instrumented with 2 cm wide pickup strips. Every fifth module is followed by a 3 cm thick scintillator layer. The total mass of the target calorimeter was 692 t.

The Brookhaven E-734 [230] detector was a tracking calorimeter made up of 172 t liquid scintillator modules interspersed with proportional drift tubes, followed by a dense EM calorimeter and a muon spectrometer downstream of that. The detector was exposed to a wideband horn-focused beam with peak neutrino energy near 1 GeV. The Brookhaven E-776 [231] experiment comprised a finely segmented EM calorimeter, with 2.54 cm concrete absorbers interspersed with planes of drift tubes and acrylic scintillation counters, with total mass 240 t, followed by a muon spectrometer.

The FNAL Lab-E neutrino detector was used by the CCFR [212] and NuTeV [213] collaborations to perform a series of experiments in the Fermilab high energy neutrino beam ( $50 \text{ GeV} < E_\nu < 300 \text{ GeV}$ ). The detector was comprised of six iron target calorimeter modules, with 690 t total target mass, followed by three muon spectrometer modules, followed by two drift chambers. Each iron target calorimeter module comprised 5.2 cm thick steel plates interspersed with liquid scintillation counters and drift chambers.

The NOMAD [232] detector at CERN consisted of central tracker detector inside a 0.4 T dipole magnet (the magnet was originally used by the UA1 experiment at CERN) followed by a hadronic calorimeter and muon detectors downstream of the magnet. The main neutrino target is 3 t of drift chambers followed downstream by transition radiation detectors which are followed by an EM calorimeter. NOMAD was exposed to the same

wideband neutrino beam as was CHORUS.

MINERvA [233] is a hybrid detector based around a central plastic scintillator tracker: 8.3 t of plastic scintillator strips with triangular cross section read out by MAPMTs coupled to WLS fibers. The scintillator tracker is surrounded by electromagnetic and hadronic calorimetry, which is achieved by interleaving thin lead (steel) layers between the scintillator layers for the ECAL (HCAL). MINERvA is situated upstream of the MINOS near detector which acts as a muon spectrometer. Upstream of the scintillator tracker is a nuclear target region containing inactive layers of C (graphite), Pb, Fe (steel), and O (water). MINERvA's physics goals span a wide range of neutrino-nucleus interaction studies, from form factors to nuclear effects.

T2K [234] in Japan employs two near detectors at 280 m from the neutrino beam target, one centered on the axis of the horn-focused J-PARC neutrino beam and one placed  $2.5^\circ$  off-axis. The on-axis detector, INGRID, is described above. The  $2.5^\circ$  off-axis detector, ND280, employs the UA1 magnet (at 0.2 T) previously used by NOMAD. Inside the magnet volume are three separate detector systems: the trackers, the Pi0 Detector (P0D), and several ECal modules. The tracker detectors comprise two fine-grained scintillator detectors (FGDs), read out by MPPCs coupled to WLS fibers, interleaved between three gas TPCs read out by micromegas planes. The downstream FGD contains inactive water layers in addition to the scintillators. Upstream of the tracker is the P0D, a sampling tracker calorimeter with active detector materials comprising plastic scintillator read out by MPPCs and WLS fibers, and inactive sheets of brass radiators and refillable water modules. Surrounding the tracker and P0D, but still inside the magnet, are lead-scintillator EM sampling calorimeters.

#### 35.10.4. Outlook :

Detectors for accelerator-based neutrino beams have been in use, and constantly evolving, for six decades now. The rich program of neutrino oscillation physics and attendant need for newer and better neutrino-nucleus scattering measurements means that more neutrino detectors with broader capabilities will be needed in the coming decades.

One of the most intriguing prospects is a large volume, high pressure gas time projection chamber (HPTPC). With the prospect of megawatt power accelerator-based neutrino beams, it is entirely feasible to collect high statistics data sets with a gas target. The low momentum thresholds for particle detection, and excellent momentum resolution and particle identification capabilities, of an HPTPC would open a new window into the physics of neutrino-nucleus scattering. Moreover, the ability to change the gas mixtures in the HPTPC would allow measurements in the same detector on multiple nuclear targets, which would, in turn, allow unprecedentedly accurate constraints and tuning of neutrino-nucleus interaction models.

## 35.11. Superconducting magnets for collider detectors

Revised August 2017 by Y. Makida (KEK)

**35.11.1. Solenoid Magnets** : In all cases SI unit are assumed, so that the magnetic field,  $B$ , is in Tesla, the stored energy,  $E$ , is in joules, the dimensions are in meters, and vacuum permeability of  $\mu_0 = 4\pi \times 10^{-7}$ .

The magnetic field ( $B$ ) in an simple solenoid with a flux return iron yoke, in which the magnetic field is lower than magnetic saturation of  $< 2$  T, is given by

$$B = \frac{\mu_0 n I}{L} \quad (35.39)$$

where  $n$  is the number of turns,  $I$  is the current and  $L$  is the coil length.

In an air-core solenoid case, the central field is given by

$$B(0,0) = \mu_0 n I \frac{1}{\sqrt{L^2 + 4R^2}}, \quad (35.40)$$

where  $R$  is the coil radius.

In most cases, momentum analysis is made by measuring the circular trajectory of the passing particles according to  $p = mv = qrB$ , where  $p$  is the momentum,  $m$  the mass,  $q$  the charge,  $r$  the bending radius. The sagitta,  $s$ , of the trajectory is given by

$$s = q B \ell^2 / 8p, \quad (35.41)$$

where  $\ell$  is the path length in the magnetic field. In a practical momentum measurement in colliding beam detectors, it is more effective to increase the magnetic volume than the field strength, since

$$dp/p \propto p/B \ell^2, \quad (35.42)$$

where  $\ell$  corresponds to the solenoid coil radius  $R$ . The energy stored in the magnetic field of any magnet is calculated by integrating  $B^2$  over all space:

$$E = \frac{1}{2\mu_0} \int B^2 dV \quad (35.43)$$

If the coil thin and inside an iron return yoke, (which is the case if it is to superconducting coil), then

$$E \approx (B^2/2\mu_0)\pi R^2 L. \quad (35.44)$$

For a detector in which the calorimetry is outside the aperture of the solenoid, the coil must be transparent in terms of radiation and absorption lengths. This usually means that the superconducting solenoid and its cryostat is of minimum real thickness and is made of a material with long radiation length. There are two major contributors to the thickness of a thin solenoid:

- 1) The conductor consisting of the current-carrying superconducting material (usually Nb-Ti/Cu) and the quench protecting stabilizer (usually aluminum) are wound on the

**Table 35.10:** Progress of superconducting magnets for particle physics detectors.

Experiment	Laboratory	$B$ [T]	Radius [m]	Length [m]	Energy [MJ]	$X/X_0$	$E/M$ [kJ/kg]
TOPAZ*	KEK	1.2	1.45	5.4	20	0.70	4.3
CDF*	Tsukuba/Fermi	1.5	1.5	5.07	30	0.84	5.4
VENUS*	KEK	0.75	1.75	5.64	12	0.52	2.8
AMY*	KEK	3	1.29	3	40	†	
CLEO-II*	Cornell	1.5	1.55	3.8	25	2.5	3.7
ALEPH*	Saclay/CERN	1.5	2.75	7.0	130	2.0	5.5
DELPHI*	RAL/CERN	1.2	2.8	7.4	109	1.7	4.2
ZEUS*	INFN/DESY	1.8	1.5	2.85	11	0.9	5.5
H1*	RAL/DESY	1.2	2.8	5.75	120	1.8	4.8
BaBar*	INFN/SLAC	1.5	1.5	3.46	27	†	3.6
D0*	Fermi	2.0	0.6	2.73	5.6	0.9	3.7
BELLE*	KEK	1.5	1.8	4	42	†	5.3
BES-III	IHEP	1.0	1.475	3.5	9.5	†	2.6
ATLAS-CS	ATLAS/CERN	2.0	1.25	5.3	38	0.66	7.0
ATLAS-BT	ATLAS/CERN	1	4.7–9.75	26	1080	(Toroid)†	
ATLAS-ET	ATLAS/CERN	1	0.825–5.35	5	$2 \times 250$	(Toroid)†	
CMS	CMS/CERN	4	6	12.5	2600	†	12
SiD**	ILC	5	2.9	5.6	1560	†	12
ILD**	ILC	4	3.8	7.5	2300	†	13
SiD**	CLIC	5	2.8	6.2	2300	†	14
ILD**	CLIC	4	3.8	7.9	2300	†	
FCC**		6	6	23	54000	†	12

\* No longer in service

\*\* Conceptual design in future

† EM calorimeter is inside solenoid, so small  $X/X_0$  is not a goal

inside of a structural support cylinder (usually aluminum also). The coil thickness scales as  $B^2 R$ , so the thickness in radiation lengths ( $X_0$ ) is

$$t_{\text{coil}}/X_0 = (R/\sigma_h X_0)(B^2/2\mu_0) , \quad (35.45)$$

where  $t_{\text{coil}}$  is the physical thickness of the coil,  $X_0$  the average radiation length of the coil/stabilizer material, and  $\sigma_h$  is the hoop stress in the coil [237].  $B^2/2\mu_0$  is the magnetic pressure. In large detector solenoids, the aluminum stabilizer and support cylinders dominate the thickness; the superconductor (Nb-TI/Cu) contributes a smaller fraction. The main coil and support cylinder components typically contribute about 2/3 of the total thickness in radiation lengths.

2) Another contribution to the material comes from the outer cylindrical shell of the vacuum vessel. Since this shell is susceptible to buckling collapse, its thickness is

determined by the diameter, length and the modulus of the material of which it is fabricated. The outer vacuum shell represents about 1/3 of the total thickness in radiation length.

### 35.11.2. Properties of collider detector magnets :

The physical dimensions, central field stored energy and thickness in radiation lengths normal to the beam line of the superconducting solenoids associated with the major collider are given in Table 35.10 [236]. Fig. 35.26 shows thickness in radiation lengths as a function of  $B^2R$  in various collider detector solenoids.

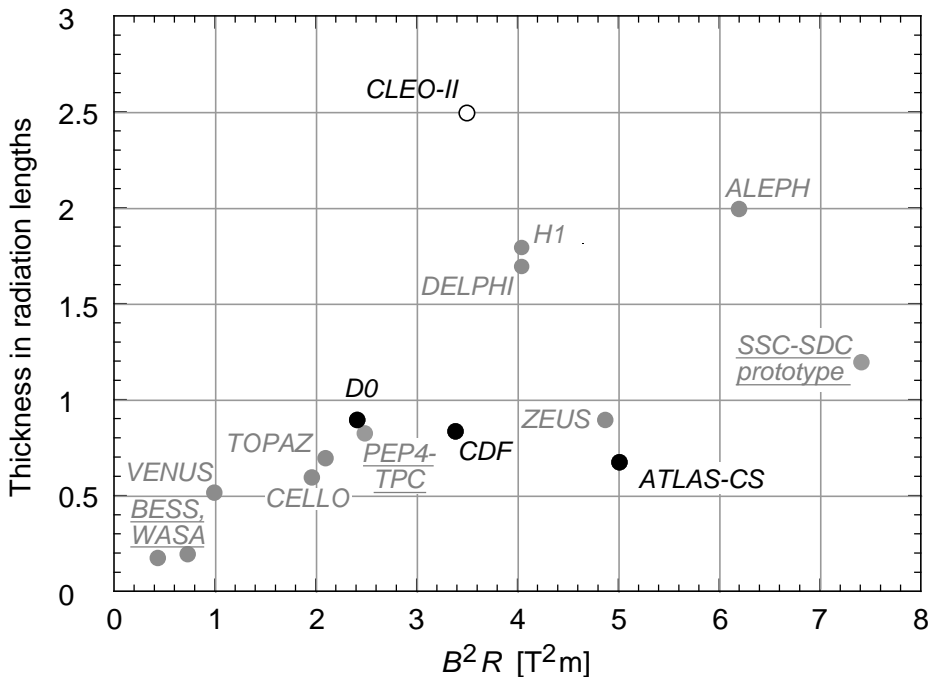


**Figure 35.26:** Magnet wall thickness in radiation length as a function of  $B^2R$  for various detector solenoids. Gray entries are for magnets no longer in use, and entries underlined are not listed in Table 35.10. Open circles are for magnets not designed to be “thin.” The SSC-SDC prototype provided important R&D for LHC magnets.

The ratio of stored energy to cold mass ( $E/M$ ) is a useful performance measure. It can also be expressed as the ratio of the stress,  $\sigma_h$ , to twice the equivalent density,  $\rho$ , in the coil [237]:

$$\frac{E}{M} = \frac{E}{\rho 2\pi t_{\text{coil}} RL} \approx \frac{\sigma_h}{2\rho} \quad (35.46)$$

The  $E/M$  ratio in the coil is approximately equivalent to  $H$ ,\* the enthalpy of the coil, and it determines the average coil temperature rise after energy absorption in a quench:

$$E/M = H(T_2) - H(T_1) \approx H(T_2) \quad (35.47)$$

\* The enthalpy, or heat content, is called  $H$  in the thermodynamics literature. It is not to be confused with the magnetic field intensity  $B/\mu$ .



where  $T_2$  is the average coil temperature after the full energy absorption in a quench, and  $T_1$  is the initial temperature.  $E/M$  ratios of 5, 10, and 20 kJ/kg correspond to  $\sim 65$ ,  $\sim 80$ , and  $\sim 100$  K, respectively. The  $E/M$  ratios of various detector magnets are shown in Fig. 35.27 as a function of total stored energy. One would like the cold mass to be as small as possible to minimize the thickness, but temperature rise during a quench must also be minimized. An  $E/M$  ratio as large as 12 kJ/kg is designed into the CMS solenoid, with the possibility that about half of the stored energy can go to an external dump resistor. Thus the coil temperature can be kept below 80 K if the energy extraction system works well. The limit is set by the maximum temperature that the coil design can tolerate during a quench. This maximum local temperature should be  $<130$  K ( $50$  K +  $80$  K), so that thermal expansion effects, which are remarkable beyond 80 K, in the coil are manageable less than 50 K.

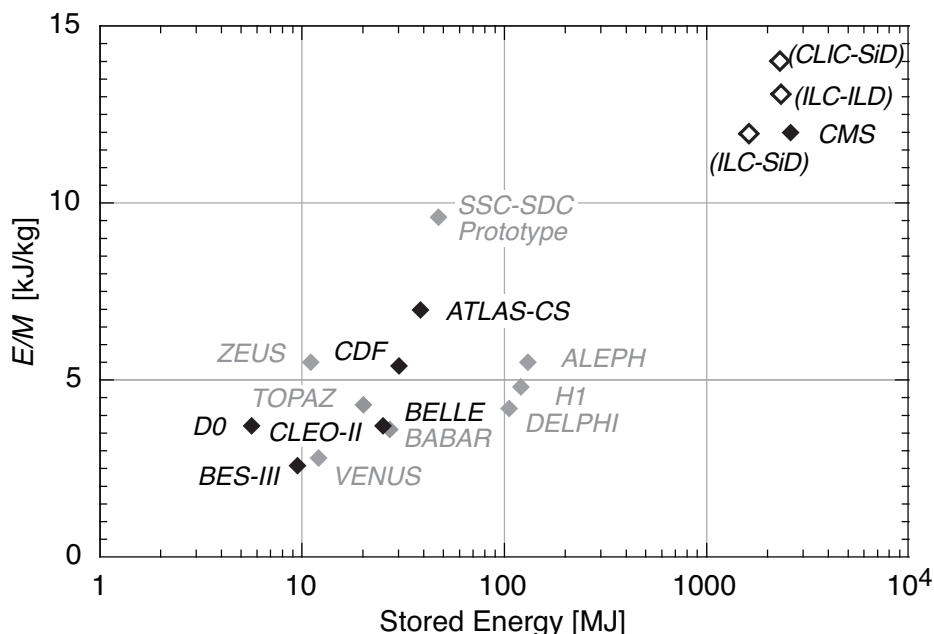


**Figure 35.27:** Ratio of stored energy to cold mass for major detector solenoids. Gray indicates magnets no longer in operation.

**35.11.3. Toroidal magnets :**

Toroidal coils uniquely provide a closed magnetic field without the necessity of an iron flux-return yoke. Because no field exists at the collision point and along the beam line, there is, in principle, no effect on the beam. On the other hand, the field profile generally has  $1/r$  dependence. The particle momentum may be determined by measurements of the deflection angle combined with the sagitta. The deflection (bending) power  $BL$  is

$$BL \approx \int_{R_i}^{R_0} \frac{B_i R_i dR}{R \sin \theta} = \frac{B_i R_i}{\sin \theta} \ln(R_0/R_i) , \quad (35.48)$$

where  $R_i$  is the inner coil radius,  $R_0$  is the outer coil radius, and  $\theta$  is the angle between the particle trajectory and the beam line axis . The momentum resolution given by the deflection may be expressed as

$$\frac{\Delta p}{p} \propto \frac{p}{BL} \approx \frac{p \sin \theta}{B_i R_i \ln(R_0/R_i)} . \quad (35.49)$$

The momentum resolution is better in the forward/backward (smaller  $\theta$ ) direction. The geometry has been found to be optimal when  $R_0/R_i \approx 3-4$ . In practical designs, the coil is divided into 6–12 lumped coils in order to have reasonable acceptance and accessibility. This causes the coil design to be much more complex. The mechanical structure needs to sustain the decentering force between adjacent coils, and the peak field in the coil is 3–5 times higher than the useful magnetic field for the momentum analysis [235].

**35.12. Measurement of particle momenta in a uniform magnetic field [238,239]**

The trajectory of a particle with momentum  $p$  (in GeV/ $c$ ) and charge  $ze$  in a constant magnetic field  $\vec{B}$  is a helix, with radius of curvature  $R$  and pitch angle  $\lambda$ . The radius of curvature and momentum component perpendicular to  $\vec{B}$  are related by

$$p \cos \lambda = 0.3 z B R , \quad (35.50)$$

where  $B$  is in tesla and  $R$  is in meters.

The distribution of measurements of the curvature  $k \equiv 1/R$  is approximately Gaussian. The curvature error for a large number of uniformly spaced measurements on the trajectory of a charged particle in a uniform magnetic field can be approximated by

$$(\delta k)^2 = (\delta k_{\text{res}})^2 + (\delta k_{\text{ms}})^2 , \quad (35.51)$$

where  $\delta k$  = curvature error

$\delta k_{\text{res}}$  = curvature error due to finite measurement resolution

$\delta k_{\text{ms}}$  = curvature error due to multiple scattering.

If many ( $\geq 10$ ) uniformly spaced position measurements are made along a trajectory in a uniform medium,

$$\delta k_{\text{res}} = \frac{\epsilon}{L'^2} \sqrt{\frac{720}{N+4}} , \quad (35.52)$$

where  $N$  = number of points measured along track

$L'$  = the projected length of the track onto the bending plane

$\epsilon$  = measurement error for each point, perpendicular to the trajectory.

If a vertex constraint is applied at the origin of the track, the coefficient under the radical becomes 320.

For arbitrary spacing of coordinates  $s_i$  measured along the projected trajectory and with variable measurement errors  $\epsilon_i$  the curvature error  $\delta k_{\text{res}}$  is calculated from:

$$(\delta k_{\text{res}})^2 = \frac{4}{w} \frac{V_{ss}}{V_{ss}V_{s^2s^2} - (V_{ss^2})^2}, \quad (35.53)$$

where  $V$  are covariances defined as  $V_{s^m s^n} = \langle s^m s^n \rangle - \langle s^m \rangle \langle s^n \rangle$  with  $\langle s^m \rangle = w^{-1} \sum (s_i^m / \epsilon_i^2)$  and  $w = \sum \epsilon_i^{-2}$ .

The contribution due to multiple Coulomb scattering is approximately

$$\delta k_{\text{ms}} \approx \frac{(0.016)(\text{GeV}/c)z}{Lp\beta \cos^2 \lambda} \sqrt{\frac{L}{X_0}}, \quad (35.54)$$

where  $p$  = momentum (GeV/ $c$ )

$z$  = charge of incident particle in units of  $e$

$L$  = the total track length

$X_0$  = radiation length of the scattering medium (in units of length; the  $X_0$  defined elsewhere must be multiplied by density)

$\beta$  = the kinematic variable  $v/c$ .

More accurate approximations for multiple scattering may be found in the section on Passage of Particles Through Matter (Sec. 34 of this *Review*). The contribution to the curvature error is given approximately by  $\delta k_{\text{ms}} \approx 8s_{\text{plane}}^{\text{rms}}/L^2$ , where  $s_{\text{plane}}^{\text{rms}}$  is defined there.

### References:

1. T. Ferbel (ed.), *Experimental Techniques in High Energy Physics*, Addison-Wesley, Menlo Park, CA (1987).
2. K. Kleinknecht, *Detectors for Particle Radiation*, Cambridge University Press, Cambridge (1998).
3. G.F. Knoll, *Radiation Detection and Measurement*, 3rd edition, John Wiley & Sons, New York (1999).
4. D.R. Green, *The Physics of Particle Detectors*, Cambridge Monographs on Particle Physics, Nuclear Physics and Cosmology, Cambridge University Press, Cambridge (2000).
5. C. Leroy and P.-G. Rancoita, *Principles of Radiation Interaction in Matter and Detection*, World Scientific, Singapore (2004).
6. C. Grupen, *Particle Detectors*, Cambridge Monographs on Particle Physics, Nuclear Physics and Cosmology, Cambridge University Press (2008).
7. ICARUS Collab., ICARUS-TM/2001-09 [LGNS-EXP 13/89 add.2/01] (2001).
8. H. Spieler, IEEE Trans. **NS29**, 1142 (1982).

9. K. Arisaka, Nucl. Instrum. Methods **A442**, 80 (2000).
10. T. Hakamata (ed.), *Photomultiplier Tubes: Basics and Applications*, 3rd edition, Hamamatsu Photonics K.K., Hamamatsu (2006).
11. A. Braem *et al.*, Nucl. Instrum. Methods **A518**, 574 (2004).
12. R. Arnold *et al.*, Nucl. Instrum. Methods **A314**, 465 (1992).
13. P. Mangeot *et al.*, Nucl. Instrum. Methods **A216**, 79 (1983);  
R. Apsimon *et al.*, IEEE Trans. **NS33**, 112 (1986);  
R. Arnold *et al.*, Nucl. Instrum. Methods **A270**, 255 (1988);  
D. Aston *et al.*, Nucl. Instrum. Methods **A283**, 582 (1989).
14. J. Janesick, *Scientific charge-coupled devices*, SPIE Press, Bellingham, WA (2001).
15. R. Haitz *et al.*, J. Appl. Phys. **36**, 3123 (1965);  
R. McIntyre, IEEE Trans. Electron Devices **13**, 164 (1966);  
H. Dautet *et al.*, Applied Optics, **32**, 3894 (1993);  
Perkin-Elmer Optoelectronics, *Avalanche Photodiodes: A User's Guide*, (2003).
16. P. Buzhan *et al.*, Nucl. Instrum. Methods **A504**, 48 (2003);  
Z. Sadygov *et al.*, Nucl. Instrum. Methods **A504**, 301 (2003);  
V. Golovin and V. Saveliev, Nucl. Instrum. Methods **A518**, 560 (2004).
17. M. Landstrass *et al.*, Diam. & Rel. Matter, **2**, 1033 (1993);  
R. McKeag and R. Jackman, Diam. & Rel. Matter, **7**, 513 (1998);  
R. Brascia *et al.*, Phys. Stat. Sol. **199**, 113 (2003).
18. M. Petrov, M. Stapelbroek, and W. Kleinmans, Appl. Phys. Lett. **51**, 406 (1987);  
M. Atac and M. Petrov, IEEE Trans. **NS36**, 163 (1989);  
M. Atac *et al.*, Nucl. Instrum. Methods **A314**, 56 (1994).
19. J.B. Birks, *The Theory and Practice of Scintillation Counting*, Pergamon, London (1964).
20. D. Clark, Nucl. Instrum. Methods **117**, 295 (1974).
21. J.B. Birks, Proc. Phys. Soc. **A64**, 874 (1951).
22. B. Bengtson and M. Moszynski, Nucl. Instrum. Methods **117**, 227 (1974);  
J. Bialkowski *et al.*, Nucl. Instrum. Methods **117**, 221 (1974).
23. C. P. Achenbach, arXiv:nuc1-ex/0404008 (2004).
24. I.B. Berlman, *Handbook of Fluorescence Spectra of Aromatic Molecules*, 2nd edition, Academic Press, New York (1971).
25. F. Sauli (ed.), *Instrumentation in High Energy Physics*, World Scientific, Singapore (1992), see pp. 218–279 by C. Zorn.
26. T. Foerster, Ann. Phys. **2**, 55 (1948).
27. J.M. Fluornoy, Rad. Phys. and Chem. **41**, 389 (1993).
28. D. Horstman and U. Holm, Rad. Phys. and Chem. **41**, 395 (1993).
29. D. Blomker *et al.*, Nucl. Instrum. Methods **A311**, 505 (1992);  
J. Mainusch *et al.*, Nucl. Instrum. Methods **A312**, 451 (1992).
30. K.F. Johnson and R.L. Clough (eds.), *Proceedings of the International Conference on Radiation-Tolerant Plastic Scintillators and Detectors*, Rad. Phys. and Chem. **41** (1993).
31. S.R. Borenstein and R.C. Strand, IEEE Trans. **NS31**, 396 (1984).
32. P. Sonderegger, Nucl. Instrum. Methods **A257**, 523 (1987).

33. P. Achenbach *et al.*, Nucl. Instrum. Methods **A593**, 353 (2008).
34. C.M. Hawkes *et al.*, Nucl. Instrum. Methods **A292**, 329 (1990).
35. N. Zaitseva *et al.*, Nucl. Instrum. Methods **A668**, 88 (2012).
36. S.E. Derenzo, W.-S. Choong and W.W. Moses, Phys. Med. Biol. **59**, 3261 (2014).
37. C. Melcher and J. Schweitzer, Nucl. Instrum. Methods **A314**, 212 (1992).
38. D.W. Cooke *et al.*, J. Appl. Phys. **88**, 7360 (2000).
39. J.M. Chen *et al.*, IEEE Trans. **NS54**, 718 (2007);  
J.M. Chen *et al.*, IEEE Trans. **NS54**, 1319 (2007).
40. E.V.D. van Loef *et al.*, Nucl. Instrum. Methods **A486**, 254 (2002).
41. W. Drozdowski *et al.*, IEEE Trans. **NS55**, 1391 (2008).
42. M.S. Alekhin *et al.*, Appl. Phys. Lett. **102**, 161915 (2013).
43. C. Kuntner *et al.*, Nucl. Instrum. Methods **A493**, 131 (2002).
44. N. Akchurin *et al.*, Nucl. Instrum. Methods **A595**, 359 (2008).
45. A. Para, FERMILAB-CONF-11-519-CD (2011);  
H. Wenzel *et al.*, FERMILAB-PUB-11-531-CD-E (2011).
46. R.H. Mao, L.Y. Zhang and R.Y. Zhu, IEEE Trans. **NS59**, 2229 (2012).
47. W.W. Moses, W.-S. Choong and S.E. Derenzo, Acta Physica Polonica **B7**, 725 (2014).
48. R.H. Mao, L.Y. Zhang and R.Y. Zhu, IEEE Trans. **NS55**, 2425 (2008).
49. B.D. Rooney and J.D. Valentine, IEEE Trans. **NS44**, 509 (1997).
50. W.W. Moses *et al.*, IEEE Trans. **NS55**, 1049 (2008).
51. G. Gratta, H. Newman, and R.Y. Zhu, Ann. Rev. Nucl. and Part. Sci. **44**, 453 (1994).
52. R.Y. Zhu, Nucl. Instrum. Methods **A413**, 297 (1998).
53. F. Yang *et al.*, IEEE Trans. **NS63**, 612 (2016).
54. F. Yang *et al.*, IEEE Trans. **NS64**, 665 (2017).
55. R.Y. Zhu, Journal of Physics: Conference Series **587**, 012055 (2015).
56. G. Dissertori *et al.*, Nucl. Instrum. Methods **745**, 1 (2014), and references therein.
57. R. Chipaux *et al.*, *Proc. of the 8th Int. Conf. on Inorganic Scintillators (SCINT2005)*, 369 (2005).
58. The CMS Electromagnetic Calorimeter Group, JINST **5** P03010 (2010).
59. M.G. Albrow *et al.*, JINST **7**, P10027 (2012).
60. B. Aubert *et al.* [BaBar Collab.], Nucl. Instrum. Methods **A479**, 1 (2002).
61. A. Abashian *et al.*, Nucl. Instrum. Methods **A479**, 117 (2002).
62. M. Shiozawa *et al.* [Super-Kamiokande Collab.], Nucl. Instrum. Methods **A433**, 240 (1999).
63. *Proceedings of the International Workshops on Ring Imaging Cherenkov Detectors*, Nucl. Instrum. Methods **A343**, 1 (1993); Nucl. Instrum. Methods **A371**, 1 (1996); Nucl. Instrum. Methods **A433**, 1 (1999); Nucl. Instrum. Methods **A502**, 1 (2003); Nucl. Instrum. Methods **A553**, 1 (2005); Nucl. Instrum. Methods **A595**, 1 (2008); Nucl. Instrum. Methods **A639**, 1 (2011); Nucl. Instrum. Methods **A766**, 1 (2014).
64. J. Litt and R. Meunier, Ann. Rev. Nucl. Sci. **23**, 1 (1973).
65. D. Bartlett *et al.*, Nucl. Instrum. Methods **A260**, 55 (1987).
66. B. Ratcliff, Nucl. Instrum. Methods **A502**, 211 (2003).

67. W. Blum, W. Riegler, and L. Rolandi, *Particle Detection with Drift Chambers*, Springer-Verlag, Berlin (2008).
68. L.G. Christophorou, *Atomic and Molecular Radiation Physics*, John Wiley & Sons, Hoboken (1971);  
I.B. Smirnov, Nucl. Instrum. Methods **A554**, 474 (2005);  
J. Berkowitz, *Atomic and Molecular Photoabsorption*, Academic Press, Cambridge (2002);  
<http://pdg.lbl.gov/2007/AtomicNuclearProperties>.
69. H. Bichsel, Nucl. Instrum. Methods **A562**, 154 (2006).
70. H. Fischle *et al.*, Nucl. Instrum. Methods **A301**, 202 (1991).
71. <http://rjd.web.cern.ch/rjd/cgi-bin/cross>.
72. A. Peisert and F. Sauli, CERN 84-08 (1984).
73. S. Biagi, Nucl. Instrum. Methods **A421**, 234 (1999).
74. <http://consult.cern.ch/writeup/magboltz/>.
75. E. McDaniel and E. Mason, *The Mobility and Diffusion of Ions in Gases*, John Wiley & Sons, Hoboken (1973);  
G. Shultz *et al.*, Rev. Phys. Appl. **12**, 67 (1977).
76. G. Charpak *et al.*, Nucl. Instrum. Methods **A62**, 262 (1968).
77. G. Charpak and F. Sauli, Ann. Rev. Nucl. Sci. **34**, 285 (1984).
78. T. Ferbel (ed.), *Experimental Techniques in High Energy Physics*, Addison-Wesley, Menlo Park, CA (1987), see “Principles of Operation of Multiwire Proportional and Drift Chambers”.
79. G. Charpak *et al.*, Nucl. Instrum. Methods **A167**, 455 (1979).
80. A.H. Walenta *et al.*, Nucl. Instrum. Methods **A92**, 373 (1971).
81. A. Breskin *et al.*, Nucl. Instrum. Methods **A124**, 189 (1975).
82. A. Breskin *et al.*, Nucl. Instrum. Methods **A156**, 147 (1978).
83. R. Bouclier *et al.*, Nucl. Instrum. Methods **A265**, 78 (1988).
84. H. Drumm *et al.*, Nucl. Instrum. Methods **A176**, 333 (1980).
85. D.R. Nygren and J.N. Marx, Phys. Today **31N10**, 46 (1978).
86. <http://www.ansoft.com>.
87. P. Beringer *et al.*, Nucl. Instrum. Methods **A254**, 542 (1987).
88. J. Virdee, Phys. Reports **403**, 401 (2004).
89. H. Walenta, Phys. Scripta **23**, 354 (1981).
90. J. Va’vra, Nucl. Instrum. Methods **A515**, 1 (2003);  
M. Titov, [arXiv:physics/0403055](https://arxiv.org/abs/physics/0403055) (2004).
91. M. Aleksa *et al.*, Nucl. Instrum. Methods **A446**, 435 (2000).
92. F. Sauli and A. Sharma, Ann. Rev. Nucl. Part. Sci. **49**, 341 (1999).
93. A. Oed, Nucl. Instrum. Methods **A263**, 351 (1988);  
A. Barr *et al.*, Nucl. Phys. (Proc. Supp.) **B61**, 264 (1988).
94. Y. Bagaturia *et al.*, Nucl. Instrum. Methods **A490**, 223 (2002).
95. J. Benloch *et al.*, IEEE Trans. **NS45**, 234 (1998).
96. Y. Giomataris, Nucl. Instrum. Methods **A419**, 239 (1998).
97. F. Sauli, Nucl. Instrum. Methods **A386**, 531 (1997);  
A. Bressan *et al.*, Nucl. Instrum. Methods **A425**, 262 (1999).

98. S. Bachmann *et al.*, Nucl. Instrum. Methods **A479**, 294 (2002);  
A. Bressan *et al.*, Nucl. Instrum. Methods **A424**, 321 (1999).
99. Y. Giomataris *et al.*, Nucl. Instrum. Methods **A376**, 29 (1996).
100. J. Derre *et al.*, Nucl. Instrum. Methods **A459**, 523 (2001);  
G. Charpak *et al.*, Nucl. Instrum. Methods **A478**, 26 (2002).
101. I. Giomataris *et al.*, Nucl. Instrum. Methods **A560**, 405 (2006).
102. S. Duarte Pinto *et al.*, IEEE NSS Conf. Record **N08-4**, 1426 (2008).
103. L. Periale *et al.*, Nucl. Instrum. Methods **A478**, 377 (2002);  
R. Chechik *et al.*, Nucl. Instrum. Methods **A535**, 303 (2004);  
A. Breskin *et al.*, Nucl. Instrum. Methods **A598**, 107 (2009).
104. A. Di Mauro *et al.*, Nucl. Instrum. Methods **A581**, 225 (2007).
105. R. Bellazzini *et al.*, Nucl. Instrum. Methods **A535**, 477 (2004);  
M. Campbell *et al.*, Nucl. Instrum. Methods **A540**, 295 (2005);  
A. Bamberger *et al.*, Nucl. Instrum. Methods **A573**, 361 (2007);  
T. Kim *et al.*, Nucl. Instrum. Methods **A599**, 173 (2008).
106. M. Chefdeville *et al.*, Nucl. Instrum. Methods **A556**, 490 (2006).
107. M. Titov, arXiv:physics/0403055 (2004).
108. <http://rd51-public.web.cern.ch/RD51-Public>.
109. J. Alme *et al.*, Nucl. Instrum. Methods **A622**, 316 (2010).
110. N. Abgrall *et al.*, Nucl. Instrum. Methods **A637**, 25 (2011).
111. ALICE Collab., ALICE-PUBLIC-2015-004 (2015).
112. A.H. Walenta *et al.*, Nucl. Instrum. Methods **161**, 45 (1979).
113. H. Aihara *et al.*, IEEE Trans. **NS30**, 63 (1983).
114. X. Artru *et al.*, Phys. Rev. **D12**, 1289 (1975);  
G.M. Garibian *et al.*, Nucl. Instrum. Methods **125**, 133 (1975).
115. B. Dolgoshein, Nucl. Instrum. Methods **A326**, 434 (1993).
116. *TRDs for the Third Millenium: Proc. 2nd Workshop on Advanced Transition Radiation Detectors for Accelerator and Space Applications*, Nucl. Instrum. Methods **A522**, 1 (2004).
117. *TRDs for the Third Millenium: Proc. 4th Workshop on Advanced Transition Radiation Detectors for Accelerator and Space Applications*, Nucl. Instrum. Methods **A706**, 1 (2013).
118. V.M. Grichine and S.S. Sadilov Nucl. Instrum. Methods **A522**, 122 (2004).
119. J. Apostolakis *et al.*, Rad. Phys. and Chem. **78**, 859 (2009).
120. B. Beischer *et al.*, Nucl. Instrum. Methods **A583**, 485 (2007).
121. A. Adronic and J.P. Wessels, Nucl. Instrum. Methods **A666**, 130 (2012).
122. M. Petris *et al.*, Nucl. Instrum. Methods **A714**, 17 (2007).
123. R. Santonico and R. Cardarelli, Nucl. Instrum. Methods **A187**, 377 (1981).
124. V.V. Parkhomchuck, Yu.N. Pestov, and N.V. Petrovykh, Nucl. Instrum. Methods **93**, 269 (1971).
125. E. Cerron Zeballos *et al.*, Nucl. Instrum. Methods **A374**, 132 (1996).
126. R. Cardarelli *et al.*, Nucl. Instrum. Methods **A333**, 399 (1993).
127. P. Camarri *et al.*, Nucl. Instrum. Methods **A414**, 317 (1998).
128. G. Aielli *et al.*, Nucl. Instrum. Methods **A508**, 6 (2003).

129. R. Cardarelli *et al.*, Nucl. Instrum. Methods **A382**, 470 (1996).
130. I. Crotty *et al.*, Nucl. Instrum. Methods **A505**, 203 (2006).
131. V. Ammosov *et al.*, Nucl. Instrum. Methods **A456**, 1-2 (2000).
132. W. Riegler and D. Burgarth, Nucl. Instrum. Methods **A481**, 130-13 (2001).
133. R. Cardarelli *et al.*, JINST **8**, P01003 (2013).
134. G. Aielli *et al.*, JINST **9**, C09030 (2014).
135. R. Santonico, JINST **9**, C11007 (2014).
136. R. Santonico *et al.*, Nucl. Instrum. Methods **A661**, S2 (2012).
137. M. Bedjidian *et al.*, JINST **6** P02001 (2011).
138. P. Fonte *et al.*, Nucl. Instrum. Methods **A443**, 201 (2000).
139. L. Paolozzi *et al.*, PoS(RPC2012)065 (2012).
140. S. An *et al.*, Nucl. Instrum. Methods **A594**, 39 (2008).
141. C. Iacobaeus *et al.*, Nucl. Instrum. Methods **A513**, 244 (2003).
142. G. Aielli *et al.*, Nucl. Instrum. Methods **A456**, 82 (2000).
143. G. Aielli *et al.*, IEEE Trans. **NS53**, 567 (2006).
144. H. Sakai *et al.*, Nucl. Instrum. Methods **A484**, 153 (2002).
145. R. Santonico, JINST **8**, P04023 (2013).
146. L. Lopes *et al.*, Nucl. Instrum. Methods **A533**, 69 (2003).
147. H. Spieler, *Semiconductor Detector Systems*, Oxford Univ. Press, Oxford (2005).
148. F. Scholze *et al.*, Nucl. Instrum. Methods **A439**, 208 (2000).
149. G. Lindström *et al.*, Nucl. Instrum. Methods **A465**, 60 (2001).
150. C. Da Via *et al.*, Nucl. Instrum. Methods **A509**, 86 (2003).
151. G. Kramberger *et al.*, Nucl. Instrum. Methods **A481**, 297 (2002).
152. O. Krasel *et al.*, IEEE Trans. **NS51**, 3055 (2004).
153. G. Lindström *et al.*, Nucl. Instrum. Methods **A426**, 1 (1999).
154. A. Holmes-Siedle and L. Adams, *Handbook of Radiation Effects*, 2nd edition, Oxford Univ. Press, Oxford (2002).
155. V. Radeka, IEEE Trans. **NS15**, 455 (1968);  
V. Radeka, IEEE Trans. **NS21**, 51 (1974).
156. F.S. Goulding, Nucl. Instrum. Methods **100**, 493 (1972);  
F.S. Goulding and D.A. Landis, IEEE Trans. **NS29**, 1125 (1982).
157. W.R. Nelson, H. Hirayama, and D.W.O. Rogers, SLAC-265 (1985).
158. R. Brun *et al.*, CERN DD/EE/84-1 (1987).
159. D. Hitlin *et al.*, Nucl. Instrum. Methods **137**, 225 (1976);  
See also W. J. Willis and V. Radeka, Nucl. Instrum. Methods **120**, 221 (1974), for a more detailed discussion.
160. R. Wigmans, *Calorimetry: Energy Measurement in Particle Physics*, Inter. Series of Monographs on Phys. **107**, Clarendon Press, Oxford (2000).
161. ATLAS Collab., CERN/LHCC 96-41 (1996).
162. CMS Collab., CERN/LHCC 97-33 (1997).
163. N. Akchurin *et al.*, Nucl. Instrum. Methods **A399**, 202 (1997).
164. B. Aubert *et al.*, Nucl. Instrum. Methods **A321**, 467 (1992).
165. A. Artamonov *et al.*, JINST **3**, P02010 (2008).
166. F. Ariztizabal *et al.*, Nucl. Instrum. Methods **A349**, 384 (1994).



167. S. Abdullin *et al.*, Eur. Phys. J. **C53**, 139 (2008).
168. M. Romalli, J. Phys. Conf. Series **404** 012050 (2012);  
C. Adloff *et al.*, arXiv:1306.3037 (2013).
169. T.A. Gabriel *et al.*, Nucl. Instrum. Methods **A338**, 336 (1994).
170. D.E. Groom, Nucl. Instrum. Methods **A572**, 633 (2007); Erratum: D.E. Groom,  
Nucl. Instrum. Methods **A593**, 638 (2008).
171. N. Akchurin *et al.*, Nucl. Instrum. Methods **A408**, 380 (1998); An energy-  
independent analysis of these data is given in Ref. 170.
172. P. Adragna *et al.*, Nucl. Instrum. Methods **A615**, 158 (2010).
173. C.W. Fabjan *et al.*, Phys. Lett. **B60**, 105 (1975).
174. C. Leroy, J. Sirois, and R. Wigmans, Nucl. Instrum. Methods **A252**, 4 (1986).
175. J.E. Brau and T.A. Gabriel, Nucl. Instrum. Methods **A238**, 489 (1985);  
H. Brückmann and H. Kowalski, ZEUS Int. Note 86/026 DESY, Hamburg (1986);  
R. Wigmans, Nucl. Instrum. Methods **A259**, 389 (1987);  
R. Wigmans, Nucl. Instrum. Methods **A265**, 273 (1988).
176. P. Mockett, SLAC-267, 335 (1987).
177. R. Wigmans, *Proc. 7th Inter. Conf. on Calorimetry in High Energy Physics*, 182  
World Scientific, River Edge, NJ, (1998);  
N. Akchurin *et al.*, Nucl. Instrum. Methods **A537**, 537 (2005).
178. G. Drews *et al.*, Nucl. Instrum. Methods **A335**, 335 (1990).
179. M. Holder *et al.*, Nucl. Instrum. Methods **151**, 69 (1978).
180. R.K. Bock, T. Hansl-Kozanecka, and T.P. Shah, Nucl. Instrum. Methods **186**, 533  
(1981);  
Y.A. Kulchitsky and V.B. Vinogradov, Nucl. Instrum. Methods **A455**, 499 (2000).
181. D. Acosta *et al.*, Nucl. Instrum. Methods **A316**, 184 (1997).
182. N. Akchurin, *et al.*, Nucl. Instrum. Methods **A735**, 120 (2013).
183. W. Walkowiak, Nucl. Instrum. Methods **A449**, 288 (2000).
184. L.S. Miller *et al.*, Phys. Rev. **166**, 871 (1968).
185. E. Shibamura *et al.*, Nucl. Instrum. Methods **A316**, 184 (1975).
186. K. Yoshino *et al.*, Phys. Rev. **A14**, 438 (1976).
187. A.O. Allen *et al.*, NSRDS-NBS-58 (1976).
188. P. Benetti *et al.*, Nucl. Instrum. Methods **A32**, 361 (1993).
189. A.M. Kalinin *et al.*, ATLAS-LARG-NO-058 (1996).
190. G. Danby *et al.*, Phys. Rev. Lett. **9**, 36 (1962).
191. S. van der Meer, CERN 61-07 (1961).
192. J.A. Formaggio and G.P. Zeller, Rev. Mod. Phys. **84**, 1307 (2013).
193. H. Faissner, “CERN Spark Chamber Neutrino Experiment”, INSPIRE-1377455.
194. A.E. Asratien *et al.*, Phys. Lett. **79**, 497 (1978).
195. H. Faissner *et al.*, Phys. Lett. **B68**, 377 (1977).
196. F.J. Hasert *et al.*, Nucl. Phys. **B73**, 1 (1974).
197. N. Armenise *et al.*, Phys. Lett. **B81**, 385 (1979).
198. S.J. Barish *et al.*, Phys. Rev. **D16**, 3103 (1977).
199. N.J. Baker *et al.*, Phys. Rev. **D23**, 2499 (1981).
200. J.W. Chapman *et al.*, Phys. Rev. **D14**, 5 (1976).

201. E.P. Kuznetsov *et al.*, Preprint IHEP 71-75, Serpukhov, (1971).
202. Y. Fukuda *et al.*, Nucl. Instrum. Methods **A501**, 418 (2003).
203. Y. Fukuda *et al.*, Phys. Rev. **D74**, 072003 (2006).
204. A.A. Aguilar-Arevalo *et al.*, Nucl. Instrum. Methods **A599**, 28 (2009).
205. A.A. Aguilar-Arevalo *et al.*, Phys. Rev. **D79**, 072002 (2009).
206. A. Benvenuti *et al.*, Nucl. Instrum. Methods **125**, 447 (1975).
207. C. Athanassopoulos *et al.*, Nucl. Instrum. Methods **A388**, 149 (1997).
208. K. Hiraide *et al.*, Phys. Rev. **D78**, 112004 (2008).
209. D.S. Ayres *et al.*, FERMILAB-DESIGN-2007-01 (2007).
210. B. C. Barish, Phys. Rept. **39**, 279 (1978).
211. M. Holder *et al.*, Nucl. Instrum. Methods **148**, 203 (1978).
212. W.K. Sakumoto *et al.*, Nucl. Instrum. Methods **A294**, 179 (1990).
213. D.A. Harris *et al.*, Nucl. Instrum. Methods **A447**, 377 (2000).
214. I. Ambats *et al.*, FERMILAB-DESIGN-1998-02 (1998).
215. C. Rubbia, CERN-EP-INT-77-08 (1977).
216. S. Amerio *et al.*, Nucl. Instrum. Methods **A527**, 329 (2004).
217. C. Anderson *et al.*, JINST **7**, 10020 (2012).
218. H. Chen *et al.*, FERMILAB-PROPOSAL-0974 (2007).
219. D.H. Perkins, Nature **159**, 126 (1947).
220. N. Uhida *et al.*, Nucl. Instrum. Methods **224**, 50 (1984).
221. S. Aoki *et al.*, Nucl. Instrum. Methods **A447**, 361 (2000).
222. K. Kodama *et al.*, Nucl. Instrum. Methods **B93**, 340 (1994).
223. S. Aoki, Nucl. Instrum. Methods **A473**, 192 (2001).
224. T. Adam *et al.*, Nucl. Instrum. Methods **A577**, 523 (2007).
225. D. Di Ferdinando *et al.*, Radiat. Meas. **44**, 840 (2009).
226. R. Acquafredda *et al.*, New J. Phys. **8**, 303 (2006).
227. T. Fukuda *et al.*, PTEP **2017**, no. 6, 063C02 (2017).
228. A.N. Diddens *et al.*, Nucl. Instrum. Methods **178**, 27 (1980).
229. D. Geiregat *et al.*, Nucl. Instrum. Methods **A325**, 92 (1993).
230. L.A. Ahrens *et al.*, Nucl. Instrum. Methods **A254**, 515 (1987).
231. G. Gidal, LBL-91 Suppl., Rev. (1985).
232. J. Altegoer *et al.*, Nucl. Instrum. Methods **A404**, 96 (1998).
233. L. Aliaga *et al.*, Nucl. Instrum. Methods **A743**, 130 (2014).
234. K. Abe *et al.*, Nucl. Instrum. Methods **A659**, 106 (2011).
235. T. Taylor, Phys. Scripta **23**, 459 (1980).
236. A. Yamamoto, Nucl. Instrum. Methods **A494**, 255 (2003).
237. A. Yamamoto, Nucl. Instrum. Methods **A453**, 445 (2000).
238. R.L. Gluckstern, Nucl. Instrum. Methods **24**, 381 (1963).
239. V. Karimäki, Nucl. Instrum. Methods **A410**, 284 (1998).